INL/EXT-11-23511
Rev. 1

Thermal Analysis of Surrogate Simulated Molten Salts with Metal Chloride Impurities for Electrorefining Used Nuclear Fuel

Toni Y. Gutknecht

April 2012

The INL is a U.S. Department of Energy National Laboratory
operated by Battelle Energy Alliance

INL/EXT-11-23511
Rev. 1

Thermal Analysis of Surrogate Simulated Molten Salts with Metal Chloride Impurities for Electrorefining Used Nuclear Fuel

Toni Y. Gutknecht

April 2012

Idaho National Laboratory
Idaho Falls, Idaho 83415

http://www.inl.gov

Prepared for the
U.S. Department of Energy
Office of Nuclear Energy
Under DOE Idaho Operations Office
Contract DE-AC07-05ID14517

Thermal Analysis of Surrogate Simulated Molten Salts with Metal Chloride Impurities for Electrorefining Used Nuclear Fuel

A Thesis
Presented in Partial Fulfillment of the Requirements for the
Degree of Master of Science
with a
Major in Nuclear Engineering
in the
College of Graduate Studies
University of Idaho

By
Toni Yvonne Gutknecht

April 24th, 2012

Major Professor: Vivek Utgikar, Ph.D., P.E.

ABSTRACT

This project is a fundamental study to measure thermal properties (liquidus, solidus, phase transformation, and enthalpy) of molten salt systems of interest to electrorefining operations, which are used in both the fuel cycle research & development mission and the spent fuel treatment mission of the Department of Energy.

During electrorefining operations the electrolyte accumulates elements more active than uranium (transuranics, fission products and bond sodium). The accumulation needs to be closely monitored because the thermal properties of the electrolyte will change as the concentration of the impurities increases. During electrorefining (processing techniques used at the Idaho National Laboratory to separate uranium from spent nuclear fuel), it is important for the electrolyte to remain in a homogeneous liquid phase for operational safeguard and criticality reasons.

The phase stability of molten salts in an electrorefiner may be adversely affected by the buildup of fission products in the electrolyte. Potential situations that need to be avoided are: (i) build up of fissile elements in the salt approaching the criticality limits specified for the vessel, (ii) freezing of the salts due to change in the liquidus temperature and (iii) phase separation (non-homogenous solution) of elements. The stability (and homogeneity) of the phases can potentially be monitored through thermal characterization of the salts, which can be a function of impurity concentration. This work describes the experimental results of typical salts compositions, consisting of chlorides of strontium, samarium, praseodymium, lanthanum, barium, cerium, cesium, neodymium, sodium and gadolinium (as a surrogate for both uranium and plutonium), used in the processing of used nuclear fuels. Differential scanning calorimetry was used to analyze numerous salt samples providing results on the thermal properties. The property of most interest to pyroprocessing is the liquidus temperature.

It was previously known the liquidus temperature of the molten salt would change as spent fuel is processed through the Mk-IV electrorefiner. However, the extent of the increase in liquidus temperature was not known. This work is first of its kind in determining thermodynamic properties of a molten salt electrolyte containing transuranics, fission products and bond sodium. Experimental data concluded that the melting temperature of the electrolyte will become greater than the operating temperature of the Mk-IV ER during current fuel processing campaigns.

Collected data also helps predict when the molten salt electrolyte will no longer be able to support electrorefining operations.

ACKNOWLEDGMENTS

There are numerous people I would like to thank for helping, guiding, or supporting me during the pursuit of my master's degree. I could not have completed this project without each of these individuals. I would like to start by thanking Dr. Vivek Utgikar first for accepting me as a graduate student and second for his guidance throughout the course of this work. His motivation, persistence, and professionalism greatly encouraged me both as a student in his class and as his research assistant. I would also like to thank Dr. Supathorn Phongikaroon, Dr. Indrajit Charit, Mr. Jesse McBurney-Rebol, Dr. Akira Tokuhiro, Ms. Sara Moore, Ms. Alice Allen, and Mr. Don Patterson of the University of Idaho for guiding me in the right academic direction. There is one professor I encounter as a college student that I would specifically like to thank for his intelligence, humor and genial personality. Thank you to the man who got me interested in science and in my opinion is the best chemistry teacher in the world, Dr. Jim Tarter, you are awesome. Lastly, I would like to thank Brett Culver from Netzsch Instruments for helping me with technical DSC issues I seemed to encounter routinely.

Thank you to the U.S. Department of Energy (US-DOE), Idaho National Laboratory (INL), Fuel Cycle Research and Development Program (FCR&D) and the Republic of Korea (ROK), Korean Atomic Energy Research Institute (KAERI), Ministry of Education, Science and Technology (MEST) for providing the monetary assistance and research project for my thesis (Work package # FT-12IN110509, "Critical Gap R&D – INL: Fundamental Properties of TRU – Bearing Salt"). Research was performed at the Idaho National Laboratory under the guidance of Dr. Guy Fredrickson. Dr. Fredrickson was vital as a mentor, teacher, and fearless leader, I don't know that I will ever be able to thank him enough for the opportunity he has given me, thanks Guy. I would also like to thank Dr. Jeffrey Wass, manager of the pyroprocessing group at the Idaho National Laboratory, for sponsoring me to do research and accommodating me at the lab as graduate student. There are a number of other individuals that contributed to the success of this project that deserve a heartfelt thank you: Ken Marsden, Prahbat Tripathy, Trina Pettingill, DeeEarl Vaden, Ken Bateman, Don Jenkinson, Dean Burt, and Cynthia Papesch. Thank you Ms. Papesch for sharing your DSC expertise. While I am at it I would like to thank the entire Pyroprocessing department!

Table of Contents

FIGURES

TABLES

Acronyms

at.%	atom percent
Au-SS	gold plated stainless steel
BR	Breeder Reactor
DI	Deionized
DOE	Department of Energy
DSC	Differential Scanning Calorimetry
EBR-II	Experimental Breeder Reactor II
ER	Electrorefiner
FCF	Fuel Conditioning Facility
FFTF	Fast Flux Test Facility
FP	Fission Product
FR	Fast Reactor
Fs	Fissium (an alloy of Y, Zr, Mo, Ru, Rh, and Pd)
HFEF	Hot Fuel Examination Facility
IFR	Integral Fast Reactor
INL	Idaho National Laboratory
INTEC	Idaho Nuclear Technology and Engineering Center
K min^{-1}	degrees Kelvin per minute
LiCl-KCl	Lithium Chloride – Potassium Chloride
LWR	Light Water Reactor
Me	Metal
$MeCl_x$	Metal Chloride
MFC	Materials and Fuels Complex
mg	milligram
mol%	Molecular Percentage/Molar %
MW	Molecular Weight
ppm	parts per million
RCRA	Resource Conservation and Recovery Act

RT	Room Temperature
STA	Simultaneous Thermal Analysis
TGA	Thermogravimetric Analysis
TRU	Transuranic
UHP	Ultra High Purity
WCL	Water Chemistry Laboratory
wt%	weight percent

GLOSSARY

Binary Phase Diagram: A set of equilibrium curve and points represented in a temperature versus composition plane, typically at constant pressure (1atm).

Breeder Reactor: A fast neutron reactor conFigured to produce more fissile material than it consumes, using fertile material such as depleted uranium in a blanket around the core.

Calibration: Using the same heating rate, purge gas, and flow rate to be used for the specimens on a set of three or more standards.

Composition: Quantity of components of a mixture; expressed in terms of weight percent or atomic percent of each of the components in a mixture.

Cross Section: A measure of the probability of an interaction between a particle and a target nucleus, expressed in barns (1 barn = 10^{-24} cm^2).

Crystallization Temperature: The temperature at which a specimen undergoes crystallization upon cooling.

Differential Scanning Calorimeter (DSC): A technique in which the heat flow difference into a substance and a reference material is measured as a function of temperature while the substance and reference material are subjected to a controlled-temperature program.

Endotherm: In thermal analysis, the thermal record of a transition where heat is absorbed by the specimen. Tendency for un-mixing, ($\Delta H > 0$).

Enthalpy: A thermodynamic function defined by the equation $H=U+PV$ where H is the enthalpy, U is the internal energy, P is the pressure, and V is the volume of the system. At constant pressure the change in enthalpy measures the quantity of heat exchanged by the system and its surroundings.

Eutectic: Mixture of two or more substances which solidifies as a whole when cooled from the liquid state, without change in composition; represents the lowest melting point of the system.

Exotherm: In thermal analysis, the thermal record of a transition where heat is evolved by the specimen. Tendency of compound formation, ($\Delta H < 0$).

Fast Reactor: A reactor with no moderator and that therefore uses fast neutrons. It normally burns plutonium while producing fissile isotopes in fertile material, such as depleted uranium (U-235) or thorium.

Fast Neutron: Neutron released during fission, traveling at a very high velocity (20,000km/s) and having high energy (~10MeV).

Fertile: Capable of becoming fissile by capturing neutrons, possibly followed by radioactive decay. Examples are U-238, Th-232 and Pu-240.

Fissile: Capable of capturing a slow (thermal) neutron and undergoing nuclear fission, such as U-235, Pu-239, U-233, Pu-241.

Fission Product: Daughter nuclei resulting either from the fission of heavy elements such as uranium, or the radioactive decay of those primary daughters; usually highly radioactive.

Fissium: Alloy of Mo (49.2%), Ru (39.2%), Rh (5.6%), Pd (3.8%), Zr (2.0%), and Nb (0.2%)

High Enriched Uranium: Uranium enriched to at least 20% U-235.

Liquidus: Locus of points in a phase diagram, representing the temperature, under equilibrium conditions, at which each composition in the system begins to freeze during cooling, or completes melting during heating.

Melting Temperature: At a given pressure, the temperature at which a crystalline solid undergoes a phase transition to the isotopic state when heat is added.

Onset: The temperature or time at which a deflection is first observed from the established baseline prior to the thermal event.

Peak: Portion of a thermal curve characterized by a deviation from the established baseline, a maximum dependant parameter deflection, and a reestablishment of a baseline not necessarily identical to that before the peak.

Phase: Homogenous, distinguishable portion of a material system.

Processing: Chemical treatment of used reactor fuel to separate uranium and plutonium and possibly transuranic elements from the small quantity of fission product wastes and transuranic elements produced during irradiation, leaving a much reduced quantity of high-level waste.

Spent Fuel: Highly radioactive fuel that has been removed from the reactor core; typically stored in underwater in spent fuel storage pools.

Solidus: Locus of point in a phase diagram representing the temperature, under equilibrium conditions, at which each composition in a system begins to melt during heating or completes freezing during cooling.

Subsolidus: Phase transitions occurring at temperature below the liquidus-solidus relation.

Supercooling: To cool a substance below a transition temperature without the transition occurring, especially to cool below the freezing point without solidification.

Temkin Theory: A theory developed by M. Temkin in 1945 dealing with fused salts as ionic solutions. In the theory the cations and anions in an ionic melt are to be considered as arranged (similarly to what occurs in an ionic crystal) in two statically distinct although mechanically non-separable sublatticelike assemblies, in either of which permutations of only cations or of anions may take place.

Ternary Phase Diagram: Set of phase equilibrium surfaces, curves, and points plotted on an equilateral triangle or composition triangle. Typically ternary systems are plotted as liquidus projections at constant pressure, due to the complex nature of a ternary system.

Thermal Neutron: Slow or delayed neutron with a kinetic energy of about 0.0025eV. Thermal neutrons typically have a much larger neutron cross section for a given nuclide than fast neutrons.

Transformation Temperature: Temperature at which a change in phase occurs.

Transuranic Element: A very heavy element formed artificially by neutron capture and possibly subsequent beta decay. Has a higher atomic number than uranium. All are radioactive.

1. INTRODUCTION

Today, nearly 20% of electric power in the United States is supplied by nuclear reactors, predominantly thermal Light Water Reactors (LWR) (Hore-Lacy, 2003). However, the first nuclear reactor to supply power to the electrical grid in any usable amount was not a thermal, but a fast reactor: the Experimental Breeder Reactor (EBR), EBR-I, located on the Idaho National Laboratory (INL) complex near Arco, Idaho. Breeder Reactors (BRs) are a type of Fast Reactor (FR), which have the potential to produce "breed" more fuel than they consume. Fast neutrons have energy in the 10 MeV range, while thermal neutrons have energies around 0.0025 eV (Lewis, 1978). In an ideal BR, neutrons leak from the core to the blanket material, the core being composed of fissile plutonium (Pu-239) that would breed more Pu-239 from a fertile blanket of uranium (U-238) (Hore-Lacy, 2003). The decay mechanism through which this takes place is shown below:

$$\mathrm{U}^{238} \overset{+\mathrm{n}}{\to} \mathrm{U}^{239} \overset{\beta^-}{\to} Np^{239} \overset{\beta^-}{\to} {Pu^{239}}^{238}$$

$$\text{Uranium-238} \overset{+\mathrm{n}}{\to} \text{Uranium-239} \xrightarrow{\text{23.5 min}} \text{Neptunium-239} \xrightarrow{\text{2.35 days}} \text{Plutonium-239}$$

BRs have core power densities much higher than thermal reactors; so, BR cores are much smaller than thermal reactors and typically comprised of tightly packed hexagonal fuel elements, which allow high neutron flux levels and a minimal amount of moderators when compared to a typical LWR (Lewis, 1978). BRs cores consist of two main parts: (1) the driver, which undergoes nuclear fission and (2) the blanket which absorbs neutrons released from the core. A schematic of a BR core is shown in Figure 1.1 for the Experimental Breeder Reactor-II (EBR-II). In Figure 1.1, the core is composed of driver assemblies surrounded by the inner and outer blanket fuel assemblies. The driver fuel used in BRs can be either: binary, ternary, or fissium fuel. Binary fuels are made of uranium and zirconium. Ternary fuels are alloys of uranium, plutonium, and zirconium. Fissium fuel usually consists of uranium and zirconium but with a smaller weight percent of uranium than binary fuel (Burkes et al., 2009).

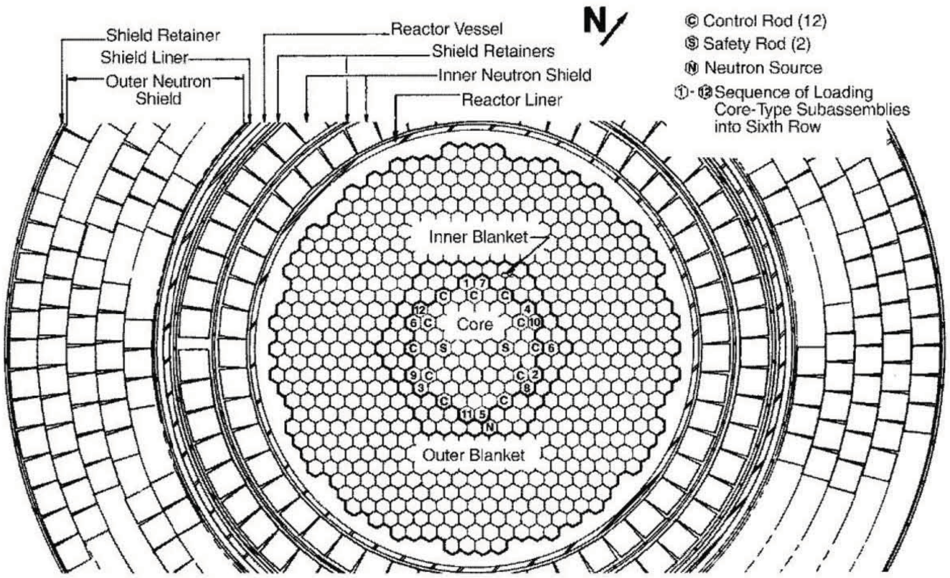

Figure 1.1: EBR-II reactor cross-section (Nesshoefer, 2009)

Figure 1.2 shows the fission cross section of Pu-239 and U-235 for the thermal through the fast neutron spectrum. The fission cross-section is a measure of the probability that fission will take place in an atom. For fast neutrons the fission cross-section is smaller compared to thermal neutrons, this means the chance of a thermal neutron interaction with atoms is more likely than fast neutrons. Thermal reactors use moderators such as water while fast reactors do not use a moderator because of the type of neutrons involved in the chain reaction. BRs use liquid metals such as sodium or a mixture of sodium and potassium to keep the reactor temperature near 500°C. Liquid metals are used because they have minimal moderating effects on fast neutrons and have the ability to transport the heat from the fuel to the bulk sodium, keeping the fuel rods from bowing or breaking due to overheating.

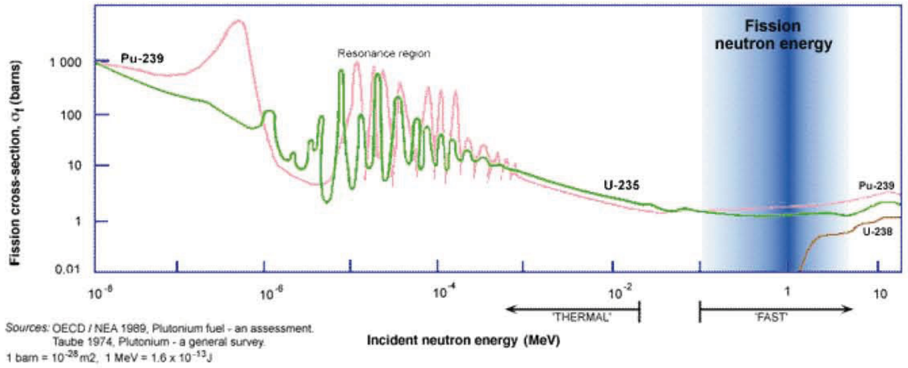

Sources: OECD / NEA 1989, Plutonium fuel - an assessment.
Taube 1974, Plutonium - a general survey.
1 barn = 10^{-28}m2, 1 MeV = 1.6×10^{-13}J

Figure 1.2: Neutron cross-sections for fission of uranium and plutonium (WNA, 2010)

The Integral Fast Reactor (IFR) program was developed as a way to have onsite processing of spent metallic fuel, increasing the lifetime of uranium (Ackerman, 1991; Chang, 1989). Currently, pyrochemical processing developed at Argonne National Laboratory in the 1960's, is being used to treat metallic fuels from the Fast Flux Test Facility (FFTF) and EBR-II fast reactors. Treatment of EBR-II fuels began in 1994 in the Fuel Conditioning Facility (FCF). Pyroprocessing of the spent metallic fuels takes place in FCF which can be seen in Figure 1.3. Currently, the Unites States does not support reprocessing of spent nuclear fuel however some metallic fuel is processed to purify uranium most of which is U-235 leaving the rest of the spent fuel (actinides, fission products, and bond sodium) in the processing vessel.

Figure 1.3: Fuel Conditioning Facility along with EBR-II reactor located at the INL.

Pyroprocessing refers to the complete set of unit operations required to recover actinide elements from spent fuel and recycle them to the reactor for use as fuel (Laidler, 1993) and is also referred to as: high temperature processing, pyrochemical processing, dry processing and non-aqueous processing. Pyroprocessing is a way to return almost all actinide elements to the reactor (Ackerman, 1991) using electrochemical reactions in a molten salt electrolyte (Simpson and Law, 2010).

Pyroprocessing unit operations include: volatilization, liquid-liquid extraction, electrolytic separations, and fractional crystallization (WNA, 2011). The fuel is dismantled and chopped into segments about an inch in length. The chopped fuel is then loaded into an anode basket and submerged in a molten halide salt electrolyte to be electrorefined, which is the major unit operation of pyroprocessing (Cochran and Tsoulfanidis, 1999). During electrorefining the fuel is anodically dissolved in eutectic lithium chloride-potassium chloride (LiCl-KCl) electrolyte and the uranium is deposited on the cathode. The fission products (FP), bond sodium, and transuranics (TRU) remain in the molten LiCl-KCl. The vessel in which electrorefining occurs is known as an electrorefiner (ER). There are two electrorefiners located at the INL: Mk-IV, used to process driver fuel and the Mk-V, used to process blanket fuel.

An advantage of pyroprocessing is that the "out of reactor" part of the fuel cycle can be designed so no fissile material leaves the processing plant; reducing the possibility of diverting the actinides for weapons use (Johnson, 1988). Most fission products decay relatively quickly compared to actinides and can be recycled back into the reactor causing the effective lifetime of the nuclear waste to be reduced to a couple hundred years (Chang, 1988); making recycling the actinides back to the reactor very appealing. Pyroprocessing has the ability to accommodate short-cooled, high burn-up fuel due to the higher radiation stabilities of non-aqueous reagents. The amount of decay heat from reactor fuels requires at least 25 years of cooling time from the date of reactor discharge before aqueous processing is possible. Pyroprocessing can be employed as soon as 5 years after fuel discharged.

The molten salt (electrolyte) in the Mk-IV ER is used to process driver fuel from metallic fueled reactors. The molten salt was originally LiCl-KCl eutectic with a melting temperature of 352°C and dissolved actinide chlorides such as uranium and plutonium (Goff and Simpson, 2009). As spent fuel is electrochemically dissolved, uranium is deposited on the cathode and active metals in the form of metal chlorides remain in the molten salt. Active metals are TRUs, FP such as rare-earth, group I and group II elements (Goff and Simpson, 2009). The thermal properties of the salt will change as impurities (FP, TRU, Na) accumulate in the salt, due to processing spent nuclear fuel. If the thermal properties, most importantly the melting temperature of the salt, can be predicted, then operators of the Mk-IV ER will better know when electrorefining operations will be limited by the condition of the salt.

In the near future, a campaign consisting of 27 batches of used driver fuel from the FFTF will be run through the Mk-IV electrorefiner followed by a significantly larger campaign of driver fuel from EBR-II (165 batches). A batch refers to about 20,000 grams of material, which includes cladding and fuel. FFTF and EBR-II processing campaigns will have a major impact on the thermal properties of the molten salt. The work for this master's thesis will simulate the salt in the Mk-IV ER as spent metal fuel from FFTF and EBR-II are processed. The simulated salt samples will be based on forecasted electrolyte compositions with a surrogate, gadolinium (Gd), being used for uranium (U) and plutonium (Pu), making this a non-radioactive study.

1.1 Thesis Organization

Chapter 1 provides a broad overview on fast reactors and their fuels. It also introduces the relevance and usefulness of this project. Chapter 2 describes what work is to be done to fulfill the experimental requirement of the Master's thesis. Chapter 3 provides detailed background information for understanding the fundamental concepts of chapters 4-9. The topics discussed in chapter 3 are: electrorefining, molten salt, differential scanning calorimetry, and phase diagrams. Chapter 4 illustrates the experimental setup used for conducting the research in this study. Chapter 5 explains the parameters chosen for this study and are based on published data, experimental data or a combination of the two. Chapter 6 provides the results of the experimental work along with a summary and recommendations. It also describes (models) the complex experimental molten salt system in terms of a simpler ternary salt based on thermodynamic models developed by other authors (Sangster and Pelton, 1987, 1991). Chapter 7 provides conclusions based on experimental and modeled results; it also provides a path on which future research can be done. Chapter 8 lists the references used in this study. Finally chapter 9 contains all the experimental data generated during the course of this work.

2. STATEMENT OF WORK

This is a fundamental study to determine the liquidus temperatures of molten salt systems typical of uranium electrorefining operations. The liquidus temperature is a function of the impurity concentration in the molten salt electrolyte which is dictated by the amount of spent fuel processed. Results from the study will be used to help plan the future of the Department of Energy (DOE) Spent Fuel Treatment mission at the INL. Thermal properties of the salt will be studied under different conditions and provide a better understanding of how salt will behave as the impurity load increases during electrorefining operations. Because the thermal characteristics of salt are functions of impurity concentration in the ER electrolyte, the stability and homogeneity of each phase can potentially be monitored through the salt's thermal characteristics.

Potential situations that need to be avoided are the following: (1) salt freezing due to an unexpected change in the liquidus temperature, (2) phase separation or non-homogeneity of the molten salt due to the precipitation of solids or formation of immiscible liquids, and (3) any mechanism that can result in the separation and concentration of fissile elements from the molten salt. Any of these situations would result in an off-normal condition outside the established safety basis for ER operations.

Thermal properties of the molten salt in an ER are affected by the buildup of FP, TRUs, and bond-sodium. By knowing how the liquidus temperature changes as a function of fuel processing, ER operators can better determine when the salt has reached its useful life. Changing the liquidus temperature could ultimately affect the overall efficiency of the ER. The ER currently operates at 500°C, at this temperature, the electrolyte at it current impurty level is a homogenous melt. But as will be seen from the results of this study, there is a point at which the salt in the ER will no longer be a homogenous melt due to TRU, FP, and sodium buildup. To determine how the liquidus temperature changes with increasing impurities (TRU, FP, sodium) several thermal analysis experiments will be run that simulates the salt composition at various points in time, processing FFTF and INTEC spent fuel.

The salt in the Mk-IV ER will change composition when processing used nuclear fuel from the FFTF (U-10Zr fuel) and EBR-II (U-5Fs fuel) reactors. EBR-II fuel of interest here is the so called "fissium (Fs)" fuel presently located at the Idaho Nuclear Technology and Engineering Center (INTEC). As

FFTF and INTEC fuel is processed in the Mk-IV ER, the impurity concentration increases in the salt. The major metal chlorides present in the electrolyte include the following:

- Eutectic Salt: LiCl-KCl eutectic
- Actinides: Uranium, Plutonium, Neptunium
- Active Metal Fission Products: Strontium, Cesium, Barium, Lanthanum, Cerium, Praseodymium, Neodymium, Samarium
- Bond Sodium: Sodium

Thermal analysis experiments will show the effects of impurity concentrations on the thermal properties of the molten salt in the Mk-IV ER.

3. LITERATURE REVIEW

3.1 Electrorefining

After successful demonstrations of the electrochemical process in the Mk-IV were performed from 1996 - 1999 for the DOE, fuel processing became part of the Advanced Fuel Cycle Initiative program in 2002 (Li et al., 2005). Pyroprocessing is a technology of separating uranium from other fuel components such as plutonium, FP, and bond sodium (Li et al., 2005). Fuel segments are chopped and loaded into an anode basket then lowered into the molten salt electrolyte of the Mk-IV ER and a potential is applied. The cladding material remains in the anode basket and the actinides, FP and sodium are dissolved in the salt maintained at 500°C. The uranium is recovered on the cathode and the bond sodium and active metal FP chemically react and displace UCl_3 from the molten salt (Li et al., 2005). Table 3.1 is a list of the major constituents of metal fuel along with their free energies of formation. Elements with low energies of formation (noble metals) remain in the cladding ($TcCl_3$ through $ZrCl_3$); elements with higher energies (active metal) of formation (UCl_3 through CsCl) of chlorides at 500°C take up residence in the electrolyte or form intermetallic compounds in the cadmium pool (located below the molten salt) (Ackerman, 1991). Uranium is processed in batches with about 12 kg of heavy metal fuel processed per batch (Yoo, 2011a and 2011b).

Table 3.1: Free energies of formation of chlorides at 775K (Ackerman, 1991)

Free Energies of Formation of Selected Chlorides at 775K
(Kcal mol^{-1} of chlorine)

CsCl	-87.8	$CeCl_3$	-68.6	UCl_3	-55.2
KCl	-86.7	$NdCl_3$	-67.9	$ZrCl_4$	-46.6
$SrCl_2$	-84.7	YCl_3	-65.1	$FeCl_2$	-32.3
LiCl	-82.5	$AmCl_3$	-64[a]	$CdCl_2$	-29.2
NaCl	-81.1	$CmCl_3$	-64[a]	$MoCl_2$	-16.8
$LaCl_3$	-70.2	$PuCl_3$	-62.4	$TcCl_3$	11.0
$PrCl_3$	-69.0	$NpCl_3$	-58[a]		

[a] Signifies estimated value

The Mk-IV ER has the ability to be operated in three modes:

(1) Direct Transport which allows electrorefining of uranium from the fuel dissolution baskets to the cathode (mandrel) which is a solid steel rod. In this setup the anode is the anode basket, where chopped fuel segments are loaded.

(2) Anodic Dissolution where the cadmium pool acts as the cathode and the anode basket acts as the anode. The metal fuel along with zirconium is dissolved into the cadmium.

(3) Deposition allows electrorefining the chopped fuel segments in the fuel dissolution baskets, a fraction of the uranium dendrites are dislodged from the deposit on the mandrel, drop to the cadmium pool, and dissolve. This uranium is retrieved by making the cadmium pool the anode and collecting the uranium on the cathode mandrel (Westphal et al., 2000).

Typically the Mk-IV ER is operated in direct transport mode; oxidation and dissolution of the metal occurs at the anode and the generic equation is:

$$M \rightarrow M^{3+} + 3e^{-} \qquad eq\ 3.1$$

where M, represents metal. Ultimately the desired reaction is: $U \rightarrow U^{3+} + 3e^{-}$. Reduction and deposition of the metal occurs at the cathode and the generic equation is:

$$M^{3+} + \ 3e^{-} \rightarrow M \qquad eq\ 3.2$$

Metal meaning high purity uranium along with some residual electrolyte salt. An example of a uranium product forming on the cathode via direct transport is shown in Figure 3.1.

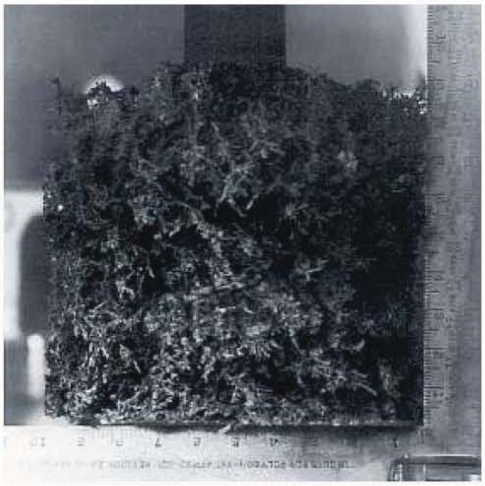

Figure 3.1: Uranium dendrites deposited on cathode of Mk-IV ER

Pyroprocessing produces three high level waste streams: ceramic waste, cathode product (recovered uranium), and a metal waste form. Ceramic waste contains the active metal fission products that have accumulated in the salt. The ceramic waste form is produced when TRUs, FP, and sodium accumulate in the salt in the form of impurities. At some point the level of impurities will be high enough that some salt (with impurities) needs to be removed to ensure the electrolyte is a homogenous melt. The removed salt can be mixed with zeolite and glass to form a ceramic waste form suiTable for disposal in a geologic repository. Of course if salt is removed from the ER eutectic LiCl-KCl will need to be added to maintain the salt inventory in the ER greater than 450 kg. A cathode product results when the deposited metal (uranium along with some residual salt) is processed in a vacuum distillation furnace called the cathode processor which separates the uranium, mostly U-235, from residual salt (Westphal et al., 2009). The salt distilled off in the cathode processor can be returned to the electrorefiner. The final waste stream produces the metallic waste form. Once the fuel and bond sodium are removed from the chopped fuel segments the cladding and noble metals remain in the anode basket, it is then removed and placed in the metal waste form furnace, which simply melts the metal into an ingot (metal waste form). The waste streams can be seen schematically in Figure 3.2, which shows the EBR-II spent fuel pyrochemical treatment process.

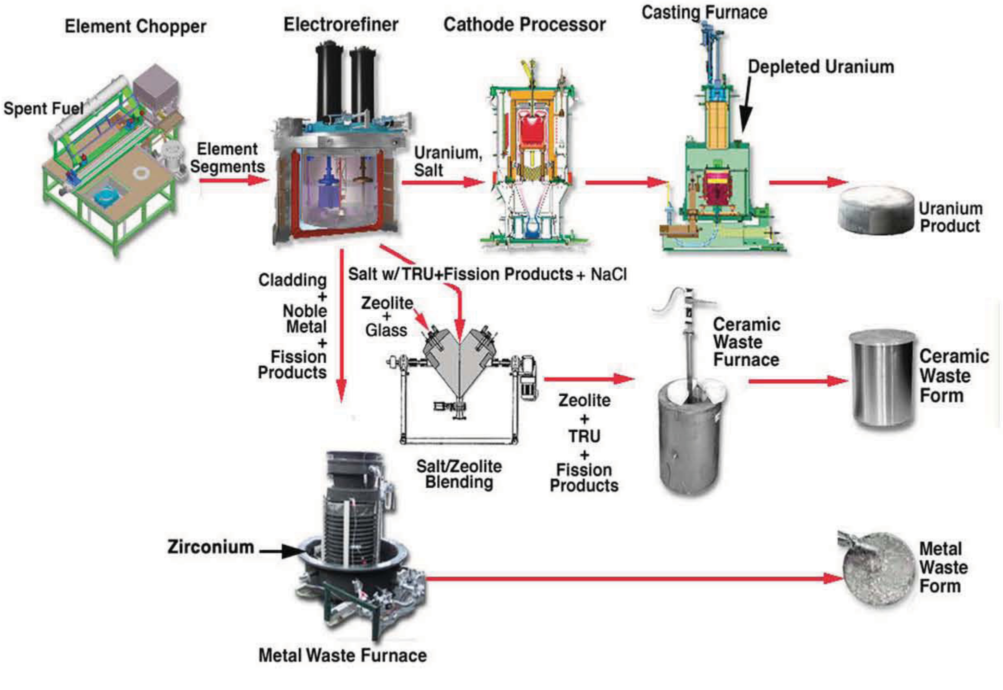

Figure 3.2: EBR-II spent fuel treatment process

3.1.1 Mk-IV Electrorefiner

The ER is the "heart" of pyroprocessing. The Mk-IV ER is made of stainless steel, operated at 500°C and is used to process spent driver fuels. It has an inner diameter and height of 1.0 m. Inside the Mk-IV is a pool of molten cadmium (Cd) approximately 10 cm deep. Directly above the Cd pool is a molten salt layer approximately 32 cm in depth. The electrode assembly consists of a stainless steel mandrel cathode and a cruciform anode basket (Li et al., 2005). A schematic of the Mk-IV ER is shown in Figure 3.3.

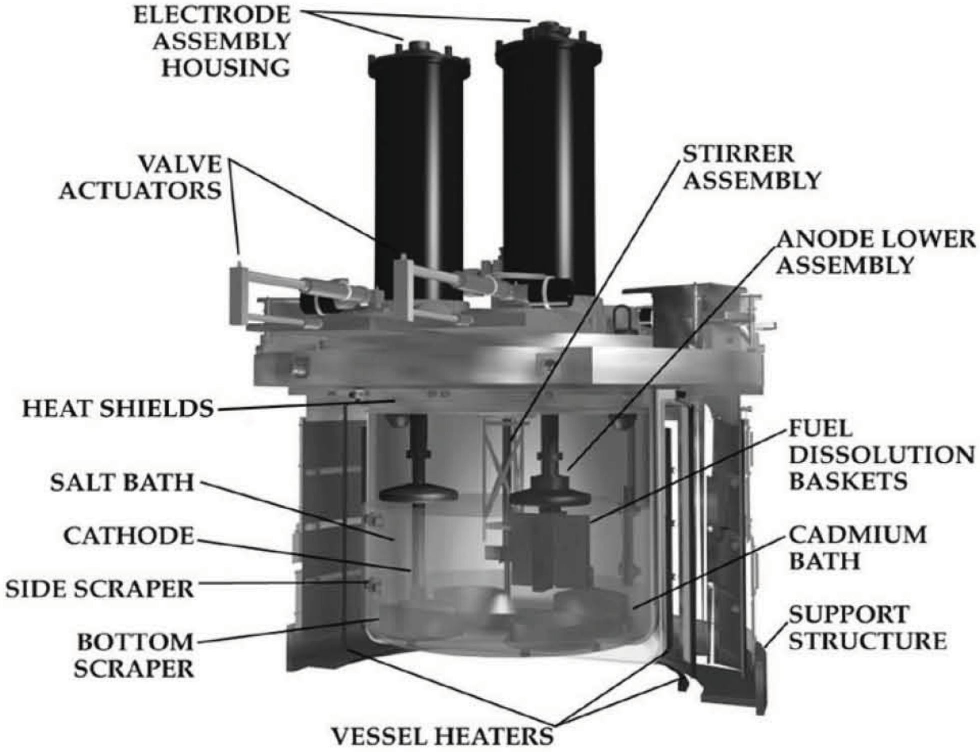

Figure 3.3: Schematic of Mk-IV ER (Vaden, 2005)

The Mk-IV has the ability to process up to 12 kg of heavy metal fuel per batch (Westphal et al., 2009). There are many components that make up an ER. Descriptions of the main components of the Mk-IV are given:

> **Electrode Assembly** – The electrode assembly contains four ports, two for the anode and two for the cathode. There is not a specific location for the anode and cathode because the Mk-IV can be wired and rewired for different electrode configurations.

Molten Salt Electrolyte – Consists of LiCl-KCl eutectic salt, with a melting temperature near 352°C. Along with LiCl-KCl there are other elements present in the electrolyte mainly as impurities introduced from the refining process. Impurities such as bond sodium, fission products, and actinides are introduced to the system from the dissolution of used fuel. The electrolyte is typically maintained at a temperature of 500°C.

Cathode – Consists of a solid steel rod for deposition of uranium. Uranium is deposited via direct uranium transport through the electrolyte. The chemical equation that explains the reaction occurring at the cathode can be depicted by: $U^{3+} + 3e^{-} \rightarrow U$. The product that forms on the cathode consists of dendritic uranium along with residual LiCl-KCl (see Figure 3.1). The salt is removed from the uranium via vacuum distillation in the cathode processor, resulting in a consolidated uranium metal ingot.

Side & Bottom Scrappers – The scrappers constrain the growth of the uranium deposit forming on the cathode.

Anode– (anode basket) Includes four rectangular baskets, arranged in cruciform geometry loaded with the contents of three chopped fuel pins containing used fuel, fission products, bond sodium and cladding material (Westphal et al., 2009). The used fuel along with the fission products and bond sodium undergo reduction-oxidation reactions with UCl_3 and will dissolve into the electrolyte and the cladding material, typically composed of stainless steel, will remain in the anode basket during electrorefining.

Cadmium Pool – Located below the molten salt electrolyte the cadmium pool aides in the recovery of dislodged dendritic material. The cadmium pool contains fission products, uranium and plutonium. The electrical configuration of the Mk-IV can be arranged several ways so that the cadmium pool serves several purposes, anodic dissolution and deposition as described earlier.

3.1.2 Fuels Processing

Two reactors are the focus of this study, FFTF and EBR-II, both of which were BRs. Both reactors started as part of the US governments IFR program. FFTF is located in Hanford, Washington and was fully operational from 1980 to 1993, during that time over 1,050 U-10Zr metal alloy fuel rods were irradiated (Burkes et al., 2009). FFTF fuel was shipped to Argonne National Laboratory West, now known as the Material and Fuel Complex (MFC) at the Idaho National Laboratory (INL). EBR-II went online in 1964, critical in 1965, and ran for nearly 30 years. EBR-II fuel is stored at the Idaho Nuclear Technology and Engineering Center (INTEC) and will be shipped to MFC for processing.

3.1.2.1 FFTF Fuel

There are 169 driver fuel pins in a FFTF driver fuel assembly. Each fuel pin is 2.4 m in length, has a fuel column length of 91.4 cm and a cladding diameter of 6.86 mm. The fuel pins are made of HT9 cladding material, a near-zero swelling ferritic-martensitic alloy with sodium used between the fuel and cladding to provide a thermal bond (Pitner and Baker, 1993). The 169 fuel pins are enclosed in a driver fuel assembly also made of HT9. A schematic of a FFTF metal fuel pin is shown in Figure 3.4. A HT9 wire is wrapped around the fuel pin to maintain spacing and promote sodium mixing within the fuel assembly. FFTF driver fuel was shipped from its Hanford location to the INL for processing in the Mk-IV ER.

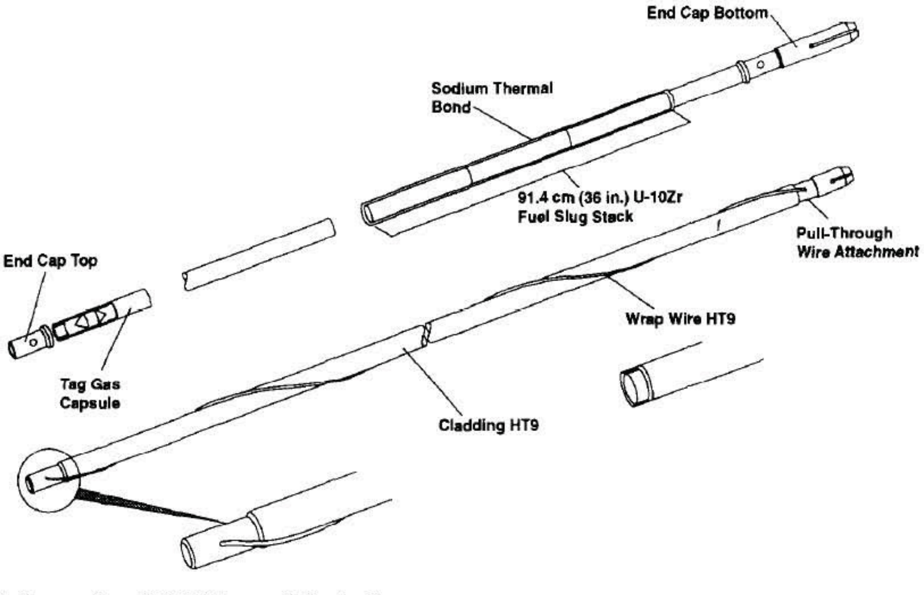

Figure 3.4: Schematic of FFTF metal fuel pin

At the INL the supply of FFTF driver fuel is stored in the Hot Fuel Examination Facility (HFEF) argon hot cell where it is dismantled before being transferred to the FCF where the Mk-IV electrorefiner is located. There is approximately 310 kg of heavy metal FFTF driver fuel that will be processed in the Mk-IV ER. Electrorefining is a batch operation and FFTF will require 27 batches with approximately 11.5 kg of heavy metal fuel per batch. The major components of FFTF fuel are listed in Table 3.2. Uranium, in the form of U-238 (~170 kg) and U-235 (~50 kg) is the major component FFTF driver fuel. Zirconium is present because the uranium was alloyed with zirconium forming a U-10wt%Zr fuel.

Table 3.2: FFTF Fuel Inventory (Yoo, 2011a)

Component	**(g)**	**% of total**
Total U$^{(b)}$	219,588	80.8
TRU	6,811	2.5
Zirconium	31,477	11.6
Sodium	7,061	2.6
Other Elements	6,978	2.6
Total Fuel Mass	271,915	100.0

(b) Total U is the sum of U-235 + U-238 masses

3.1.2.2 INTEC Fuel

Once the FFTF fuel processing campaign is finished a significantly larger and longer campaign of EBR-II driver fuel will initiate. There are several designs for EBR-II fuel (Mk-1A, Mk-II, Mk-IIs, Mk-III, Mk-IIIA, Mk-IV) this work will focus only on processing Mk-1A, Mk-II, Mk-IIA and Mk-IIB fuel. The difference between the EBR-II fuel designs is summarized in Table 3.3. When EBR-II when online in 1964, the Mark-I (Mk-I) driver fuel design was used which included a metallic fuel slug sodium bonded to a stainless steel jacket. Sodium serves the same purpose in EBR-II fuel as it did in FFTF fuel: provides a thermal bond between fuel and clad (Lahm et al., 1993). High temperatures can cause the sodium to become infused into the uranium alloy (Burkes et al., 2009).

EBR-II driver assemblies were highly enriched uranium (U-235) in uranium oxide mixed with zirconium oxide ceramic fuel, which provided the neutron source (Burkes et al., 2009). The blanket fuel composed of depleted uranium oxide pins enhanced the breeding properties of the reactor and surrounded the core in close proximity to the driver assemblies. Initial Mk-I designs did not allow for a high burnup (<1 atom percent, (at.%)) and the design was modified creating the Mk-II series fuels with a burnup of 8 at.% (Lahm et al., 1993). The fuel subassembly for EBR-II fuel contains 91 fuel elements similar to the Mk-IA fuel element shown in Figure 3.5. As with FFTF fuel a spacer wire was wrapped helically around each fuel element to maintain spacing and promote sodium mixing within the fuel assembly (Lahm et al., 1993). There is no significant difference in the designs of the FFTF and INTEC fuel except that the FFTF fuel is longer. The composition of EBR-II fuel for both Mk-I and Mk-II designs is U-5wt%Fs, where Fs stands for fissium and is normally 2.5% Mo, 1.9% Ru, 0.3% Rh, 0.2% Pd, 0.1% Zr and 0.01%Nb.

Table 3.3: Design parameters of EBR-II metal driver fuel elements

Design	**Mk-I/-IA**	**Mk-II**
Fuel alloy wt%	U-5Fs	U-5Fs
U-235 enrichment	52	67
Fuel slug mass (g)	64	52
Length (cm)	46.0	61.2
Burnup limit (at.%)	2.6	8
Plenum gas	Inert	Inert
Cladding material	SS 304L	SS 316

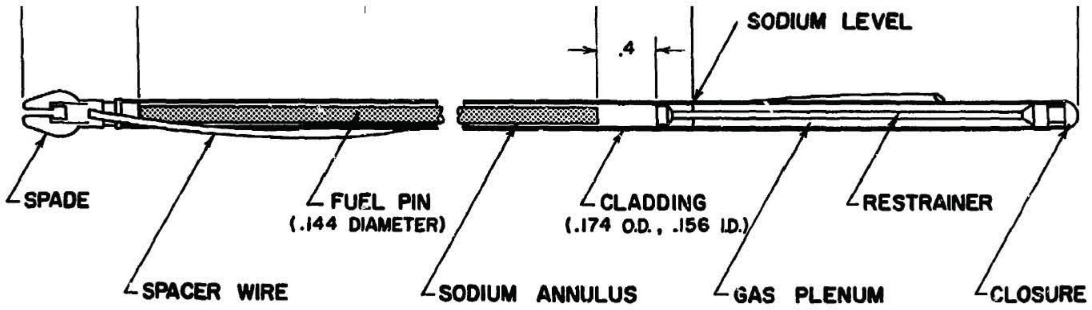

Figure 3.5: Mark-IA design of EBR-II Driver fuel element (Madson and Laug, 1972)

EBR-II fuel has been called fissium fuel but since it is being stored at INTEC in water pools, it has become known as INTEC fuel and will be referred to as such for the remainder of this thesis. The INTEC fuel campaign will consist of approximately 165 batches, processing nearly 12 kg of heavy metal fuel per batch in the Mk-IV ER; heavy metal fuel referring to all actinides (elements with atomic number 89 to 103). The major components of INTEC fuel are shown in Table 3.4. The total uranium accounts for U-235 (1,227 kg) and U-238 (713 kg).

Table 3.4: INTEC Fuel Inventory (Yoo, 2011b)

Component	grams	% of total
Total U(c)	1,939,414	94.9
TRU	8,605	0.4
Sodium	52,886	2.6
Other Elements	43,214	2.1
Total Fuel Mass	2,044,119	100.0

(c) Total U = U-235 + U-238

3.2 Molten Salt

From 1996 to present, there has been more than 953 kg of heavy metal fuel processed in the Mk-IV ER. The fuel has been mostly EBR-II driver fuel but 120 kg of blanket fuel were also processed. Once FFTF and INTEC fuel campaigns are over more than 3,200 kg of heavy metal will have been processed through the Mk-IV ER.

3.2.1 Current Molten Salt

Currently (before FFTF fuel processing), the bulk of the salt present in the Mk-IV ER is LiCl-KCl at 76.83 wt%. This is to be expected since LiCl-KCl eutectic was the starting electrolyte. Actinide chlorides are present in the salt at 9.02 wt%, group 1A metal chlorides are present at 9.53 wt%, group 2A metal chlorides are present at 0.31 wt% and lanthanide chlorides are present at 4.31 wt%. The elements present in the salt in the highest wt% (excluding those associated with the eutectic salt, LiCl-KCl) are uranium chloride (UCl_3, 7.60 wt%) and sodium chloride (NaCl, 8.30 wt%). Here, the U concentration needs to remain above 5 wt% for electrorefining of U in the Mk-IV. The driver fuel that has been processed in the ER was sodium bonded driver fuel. The sodium was infused in the uranium alloy fuel causing the sodium concentration in the electrolyte to increase as fuel is processed.

Figure 3.6 shows the buildup of metal chlorides in the salt versus kilograms (kg) of uranium processed. The initial or base electrolyte is LiCl-KCl-5wt%UCl_3. The dark lines of each color represent the weight percent (wt %) of active metals, transuranic, and lanthanides built-up in the salt prior to FFTF and INTEC fuel processing. The lighter sections of each line show the increasing wt% of metals, transuranic, and lanthanides (not as chlorides) as FFTF and INTEC fuel are processed. LiCl-KCl concentration is based on information provided by Yoo (2011a, 2011b). The projected composition takes into account the radioactive decay of plutonium and other elements.

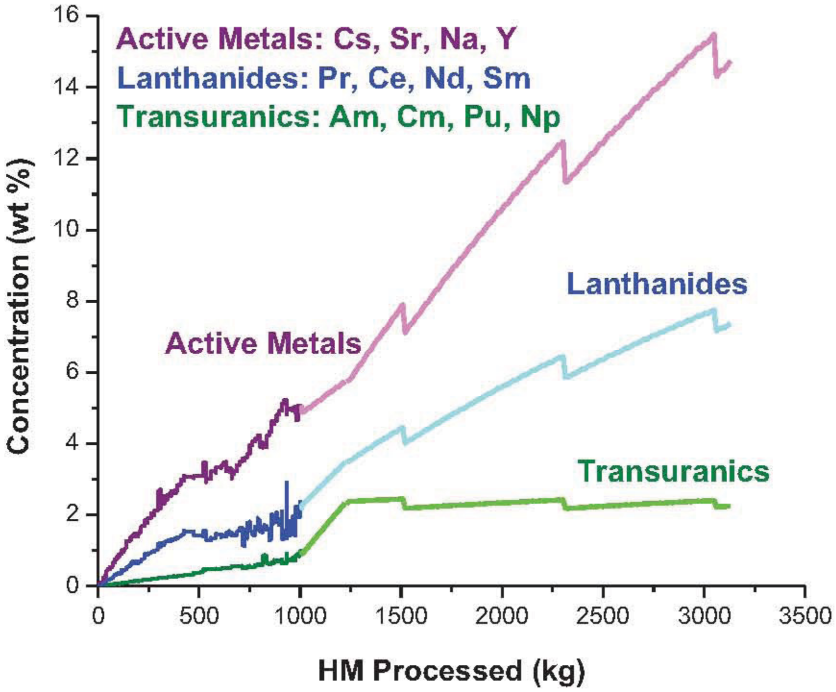

Figure 3.6: Mk-IV ER salt composition vs. uranium processed.

3.2.2 Projected Molten Salt

The projected salt composition during FFTF and INTEC fuel processing is based off calculations performed by Yoo (2011a, 2011b). These calculations assume that for each batch there will be either 11.6 kg (FFTF) or 12 kg (INTEC) of heavy metal fuel and each batch will take 15 days to process. All salt taken out of the ER as residual salt on the cathode product will be returned to the ER. Salt remaining on the cladding hulls will not be returned to the ER. It is estimated that 1600 g of salt will be taken out of the ER with each batch of fuel processed, which is a total of 307 kg of salt removed during FFTF and INTEC fuel processing (Fredrickson et al., 2010). There are mass limits for the ER that will compensate for the "bleeding" of salt by "feeding" eutectic salt to maintain a specified range of electrolyte weight (Fredrickson et al., 2010).

Active metals will reside in the fuel and are therefore transferred to the electrolyte according to equation 3.3 if the species is monovalent this would be an exchange reactions for group I elements such as Na and Cs.

$$UCl_3 + 3\,Me \rightarrow 3\,MeCl + U \qquad eq\ 3.3$$

$$UCl_3 + Na \rightarrow 3\,NaCl + U \qquad eq\ 3.4$$

For trivalent species the generic reaction is shown in Equation 3.5. Chemical species of this nature would be lanthanides and actinide elements; Equation 3.6 shows the exchange reaction for praseodymium. Uranium will be exchanged for metals whose free energies of formation are more negative (see Table 3.1) than UCl_3 (-55.2 Kcal mol^{-1}), this is known as a spontaneous reaction.

$$UCl_3 + Me \rightarrow MeCl_3 + U \qquad eq\ 3.5$$

$$UCl_3 + Pr \rightarrow PrCl_3 + U \qquad eq\ 3.6$$

During pyroprocessing, it is assumed no cladding material will be transported to the salt, and all will remain in the anode basket because the metal chlorides of noble metals are not as sTable as UCl_3 (see Table 3.1). It is also assumed that uranium will have a 95% dissolution rate in the ER, meaning 95% of all uranium in the ER will be deposited on the cathode, while 5% will remain in the salt to be involved in the exchange reactions.

There are 192 batches of fuel that are modeled (27 FFTF and 165 INTEC) for this study. During processing there are five operating conditions that must be maintained throughout the duration of the 192 batch processing such as (Yoo, 2011a, 2011b):

1. The uranium concentration in the salt must be above 5 wt%. If the concentration of U drops below 5 wt% then cadmium chloride ($CdCl_2$) will be added to increase the uranium concentration. Addition of $CdCl_2$ chemically oxidizes uranium from the Cd pool or sacrificial uranium cathodes (Vaden, 2005) spontaneously by equation 3.7. This reaction is possible because UCl_3 is more sTable than $CdCl_2$ and the free energy of reactions in equation 3.7 is -137.3 kcal mol^{-1} (Vaden, 2005).

$$3CdCl_2 + 2U \rightarrow 3Cd + 2UCl_3 \qquad eq.3.7$$

2. The amount of fissile material must be below 77.2 kg. If the amount of fissile material exceeds 77.2 kg then 50 kg of electrolyte are removed from the ER.
3. Total Pu-equivalent must remain below 10 kg. If the amount of Pu-equivalent material exceeds 10 kg then 50 kg of electrolyte is removed from the ER.
4. Salt weight must not be below 430 kg. If the weight of the salt drops below 430 kg then an addition of 50 kg eutectic LiCl-KCl is made.
5. Salt weight must not exceed 550 kg. If the salt exceeds 550 kg then 50 kg of electrolyte is removed from the ER.

There are several times during FFTF and INTEC fuel processing that conditions 1-5 are violated. During FFTF fuel processing condition 1 is violated five times, each violation is represented by a red diamond (◆) in Figure 3.7 which shows a plot of the uranium concentration in the salt versus the batches of FFTF fuel processed. During INTEC fuel processing condition 1 was violated 45 times along with three violations each of conditions 3 and 4.

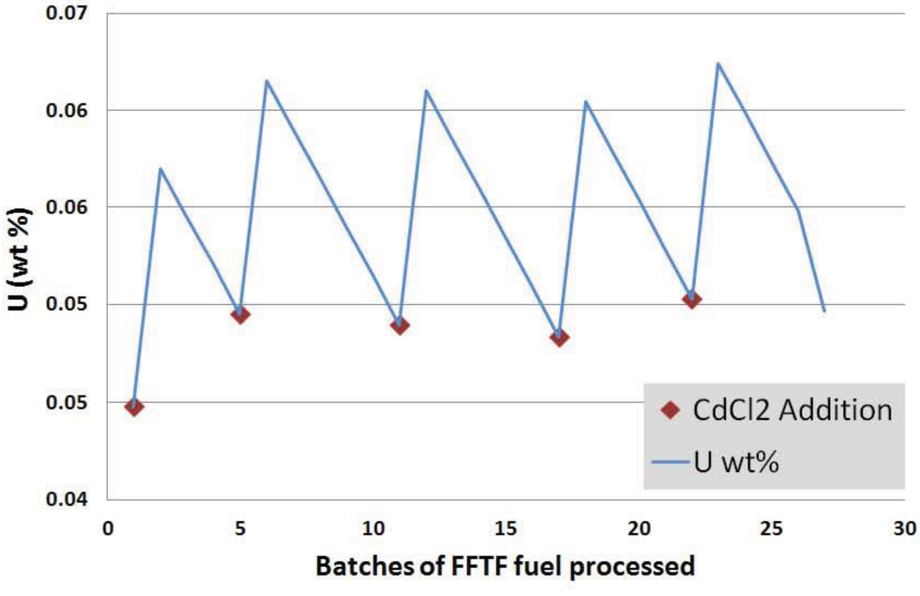

Figure 3.7: U wt% vs. batches of FFTF fuel processed (data from Yoo, 2011a)

3.3 Differential Scanning Calorimetry

3.3.1 Fundamentals

Differential Scanning Calorimetry (DSC) is a thermal analysis technique in which a physical property of a substance is measured as a function of temperature or time while the substance is subjected to a controlled-temperature program (Hohne et al., 2003). DSC can refer to differential scanning calorimeter (instrument) or differential scanning calorimetry (method) and can be simply defined as the measure of energy difference between a sample and reference crucible. DSC is a technique in which the heat flow difference into a substance and a reference material is measured as a function of temperature while the substance and reference material are subjected to a controlled-temperature program (ASTM E473-10, 2010). DSC results can yield information from peaks such as melting, crystallization, phase transformations, reactions, magnetic transitions, specific heat, evaporation, dehydrations and decomposition temperatures (Hohne et al., 2003).

There are two different types of DSC: power compensated differential scanning calorimetry and heat flux scanning calorimetry. They are distinguished depending on the method of measurement used (Hohne et al., 2003). Power compensated DSC consists of two identical microfurnaces which are mounted inside a thermostated aluminum block. The same power is supplied to each furnaces during heat up if a reaction occurs the temperature of one furnace will differ from the temperature of the other the difference is recorded as the DSC signal (Hohne et al., 2003). Power compensated DSC is less common than heat flux DSC which will be described in more detail. Figure 3.8 shows a schematic of a measuring head for a heat flux DSC; here: 1-disk, 2- furnace, 3- lid, 4- differential thermocouple(s), 5- programmer and controller, S sample crucible, R reference crucible, φ_{FS} heat flow rate form furnace to sample crucible, φ_{FR} heat flow rate from furnace to reference crucible, φ_m measured heat flow rate, K calibration factor. Some characteristics of heat flux DSC are (Hohne et al., 2003):

- The main heat flow from the furnace passes symmetrically through a disk of medium thermal conductivity;
- The crucibles, reference and sample, are positioned symmetrically around the center of the disk;
- Thermocouples are integrated into the disk (Pt/Rh type S); and

- Each thermocouple covers the majority of the area of support for the respective crucible so the calibration can be done independently of the sample location inside the crucible.

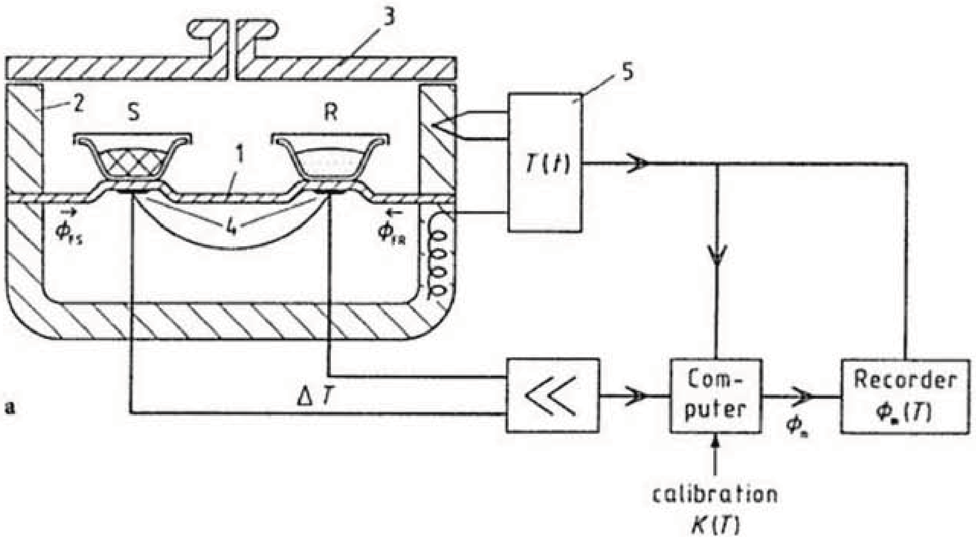

Figure 3.8: Measuring head of a heat flux DSC with disk-type measuring system (Hohne et al., 2003)

Experimental measurements were conducted using a Netzsch 449 F3 Simultaneous Thermal Analyzer (STA). The instrument used is referred to as an STA because it can simultaneously perform DSC along with Thermogravimetry (TG) during the same experiment. For the purpose of this research only the use of the heat flux DSC will be used to carry out thermal analysis and the Netzsch instrument will be referred to simply as a DSC. Heat flux is referring to the measurement of the heat flow rate between the sample and the surroundings. It has the capability to measure the heat of a reaction and partial heat levels between specific temperature intervals, such as a reaction.

The sample carrier is composed of four parts: (1) DSC measuring head, (2) capillary, (3) radiation shield, and (4) the plug (as shown in Figure 3.9). The measuring head is where the sample and reference crucible are placed, an enlarged schematic of a measuring head is show in Figure 3.8. The measuring head contains the sample carrier and thermocouple. The capillary is a corundum tube and is used to insert the sample carrier into the DSC. The radiation shield is a stack of corundum disks that provides surface area for the dissipation of heat from the furnace so as to prevent damage to the sensitive electronics of the balance. The plug connects the sample carrier with the electronics of the DSC.

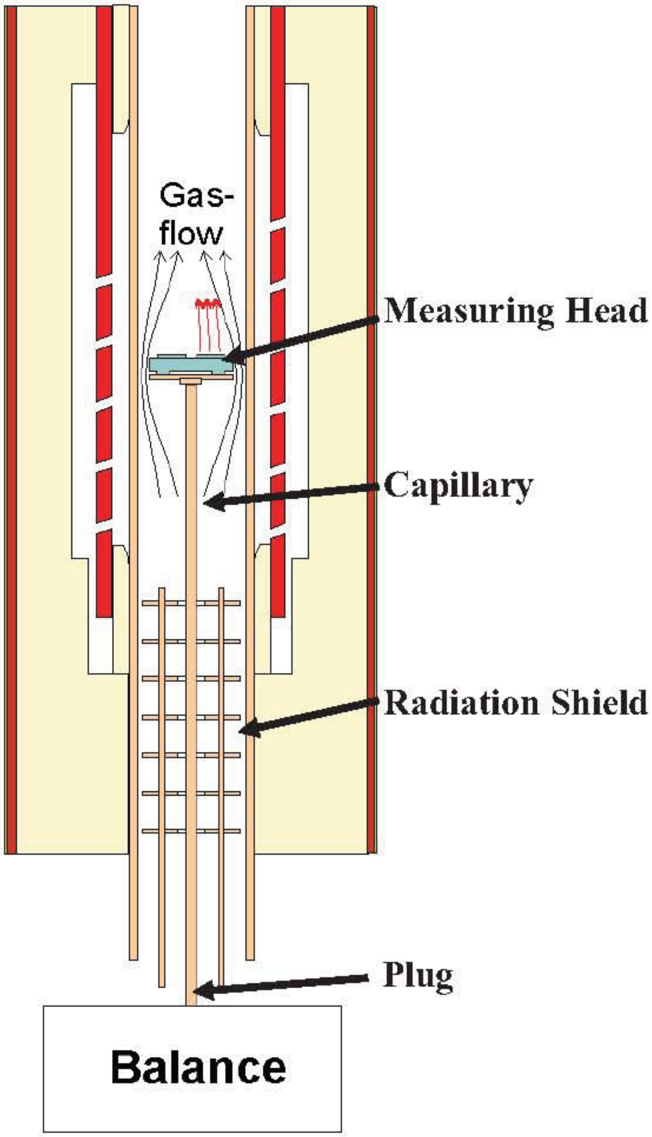

Figure 3.9: Sample carrier for DSC (Schindler, 2010)

3.3.2 DSC Curves

A signal is generated when there exists a difference in temperature between the sample and reference. If a difference between the sample and reference consumes heat (melting), an endothermic peak appears. If the difference in energy between the sample and reference produces heat the reaction is exothermic (crystallization). A DSC peak is defined as the portion of the thermal curve characterized by a deviation from the baseline, a maximum dependant parameter, and a re-establishment of the baseline not necessarily identical to that before the peak (ASTM, E473-10, 2010). When the DSC has been calibrated for temperature and sensitivity the area under the DSC peak is proportional to the transition enthalpy (Netzsch, 2009). Transition enthalpy in this context is defined as the enthalpy associated with the sample transitioning from its solid state to a liquid state (melting). A typical DSC curve for an indium standard with a 5 K min^{-1} heating rate is shown in Figure 3.10. The Figure shows a baseline, onset temperature, melting peak, and the effect of argon atmosphere on the DSC curves for three different heating cycles.

The buoyancy of a sample is affected by the type (argon, helium, air) and flow rate of purge gas. Buoyancy is caused by the sample "swimming" in the furnace atmosphere. The sample carrier sits atop the capillary as seen in Figure 3.9. Purge gas is flushed through the furnace in an upward direction. The sample carrier causes the area of the flow channel to decrease, thus, the flow rate at the sample carrier increases causing the carrier to become "buoyant" within the furnace. Figure 3.10 shows the effects of buoyancy on the sample carrier due to an argon purge gas with a flow rate of 0.34 cm^3 min^{-1}. This is predominant at low temperatures causing the baseline of the DSC curve to be rounded. The effects of buoyancy decrease as the temperature inside the furnace increases.

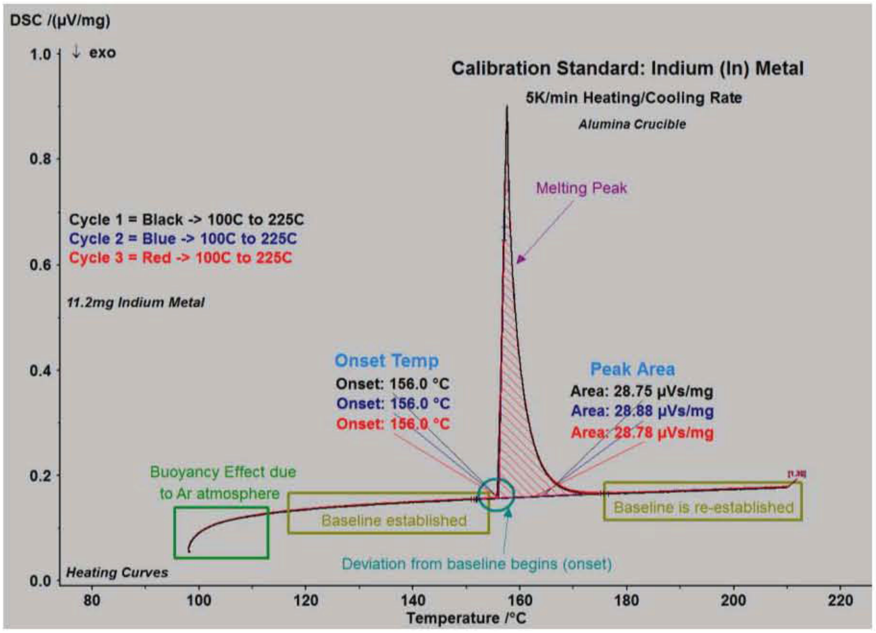

Figure 3.10: DSC thermogram for Indium standard

The onset temperature (ASTM E473-10, 2010) is defined as the temperature at which a deviation is first observed from the established baseline, (labeled and shown for the indium standard in Figure 3.10). The thermogram consists of only endothermic peak, because indium goes through only one phase transition (solid → liquid). The peak is sharp and well defined, as expected for a sample of high purity. As the purity of a sample decreases the peaks tend to become broader because transitions occur over larger temperature range. The onset or melting temperature in this case will be taken as the average of the peak onset temperatures for the three heating cycle runs. All reported temperature values are the average of three heating cycles for the duration of this work unless otherwise noted.

3.4 Phase Diagram

3.4.1 Binary System

Information from DSC curves can be used to construct phase diagrams which are typically plots of composition (abscissa) vs. temperature (ordinate) for binary systems at a constant pressure (1 atm). The composition is typically plotted as the mol fraction of material. Binary systems have three ionic species for which there are two cations and an anion, LiCl-KCl typically written as (Li,K/Cl) or one cationic and two anionic species, Na/Br,Cl. A simple, hypothetical phase diagram is shown in Figure 3.11 along with the hypothetical DSC curves used to construct the phase diagram. Peaks a_1 and a_2 represent the transitions associated with pure A; similarly peak g_1 is a sample of pure B. Peaks a_2 and g_1 represent the melting of the pure samples and help form the liquidus line which is defined as the locus of points in a phase diagram, representing the temperature, under equilibrium conditions, at which each composition in the system begins to freeze during cooling, or completes melting during heating (ASTM E1142-07, 2007). A solidus line is a peak(s) that represents the initial occurrence of the liquid phase upon heating (Franzosini and Sanesi, 1983). Any transformation that occurs below the solidus is known as a subsolidus transformation. For ionic systems the heating curve is used to determine the liquidus and solidus, this may be considered atypical of other materials such as metals or ceramics. The reason for this is supercooling which happens when a substance is cooled below its transition temperature without the transition occurring, especially cooling below the freezing point without solidification (ASTM E1142-07, 2007). However, the cooling curve can be more effective at determining phase separations of multi-component systems.

Peaks a_2, b_3, c_2, d_1, e_3, f_3 and g_1 form the liquidus line for this system. Curve (d) represents a eutectic mixture of A and B. there is only one peak (d_1) on this curve representing a eutectic invariant reaction, which is when a mixture solidifies as a whole when cooled from liquid state to solid state without change in composition (ASTM E1142-07, 2007) and represents the lowest melting point of the system. Peaks b_1, c_1, d_1, and e_1 occur at the eutectic temperature. In Figure 3.11, the eutectic peaks get smaller (decrease in area) as the composition deviates from the eutectic composition (peaks b_1, c_1, and e_1). Curve (b) the first melt (b_1) represents the eutectic temperature and with subsequent heating the amount of melt continuously increases until the liquidus is reached at b_3 (Franzosini and Sanesi, 1983). A similar description can be used to describe curve (e) except that peak e_2 represents the isothermal peritectic transformation into a liquid and mixed crystals of the amount AB_4 as a solid.

Subsolidus transformations such as f_1 are hardly detecTable by DSC (Franzosini and Sanesi, 1983). When an unknown system is being studied the pure components of that system must be studied along with a plethora of intermediate compositions (Franzosini and Sanesi, 1983).

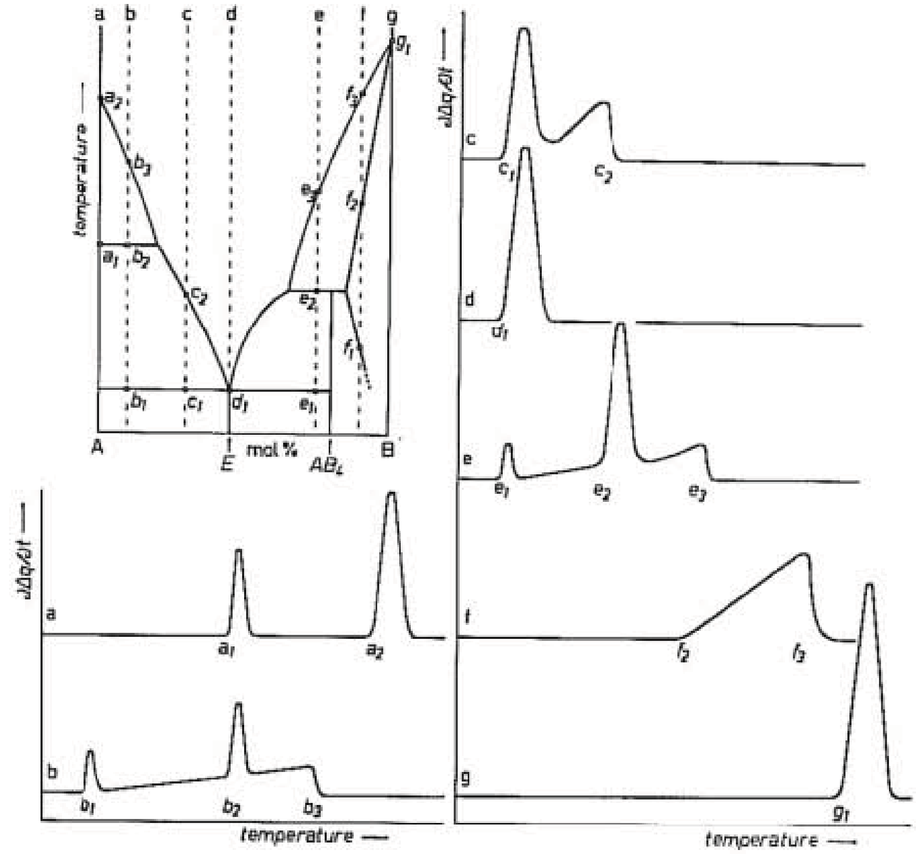

Figure 3.11: Hypothetical phase diagram (Franzosini and Sanesi, 1983)

3.4.2 Ternary System

A ternary system has four ionic species (three cationic + one anionic or three anionic and one cationic species) for example Li/K/Na,Cl. Ternary systems are represented as an equilateral triangle. Unlike the binary system the ternary additive triangle typically denotes the liquidus temperature as a function of composition. Ternary systems are called additive ternary systems if they don't form any compounds (all salts have a cation and an anion). The composition of additive ternary salts can be plotted on a equilateral triangle, where the triangular prism represents the temperature composition relationship for the system and can be seen in Figure 3.12 represented as the blue dashed line.

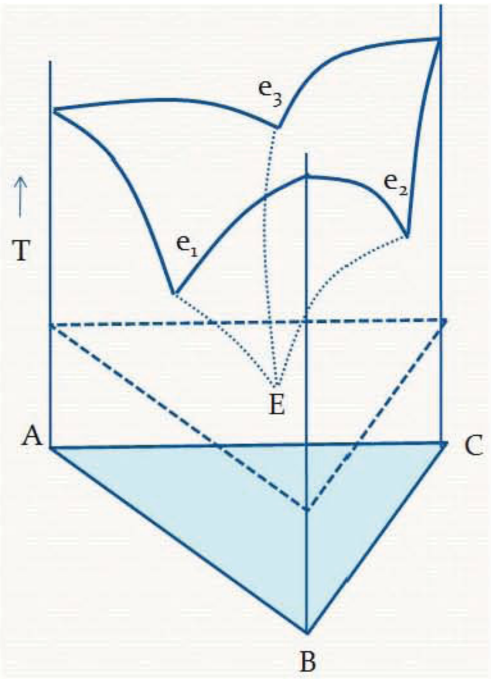

Figure 3.12: Generic additive ternary phase diagram (Phongikaroon, 2011)

All compositions on the blue dashed triangle are at the same temperature. Each face of the equilateral triangle can be viewed as a binary phase diagram; each binary system in Figure 3.12 forms a simple eutectic. The point, E, in Figure 3.12 represents the lowering of the eutectic temperature (e_1) by addition of the third solute. The ternary system forms a new minimum temperature when compared to the individual binary systems. This new minimum temperature represents the eutectic temperature for the ternary system, at which point all the material is liquid. Typically ternary phase diagrams are not shown as three dimensional equilateral triangles. It is more common in literature to report ternary systems on liquidus projections. Liquidus projections don't show the phases present at different temperatures, it shows the liquidus temperature as a function of composition and is much easier to graph than a ternary phase diagram.

3.4.3 Thermodynamics

If a system is at constant temperature and pressure, then the Gibbs free energy of the system can be defined as

$$G = H - TS \qquad eq. 3.8$$

where H is the enthalpy, T the absolute temperature and S the entropy of the system. In this system the relative stability is dependent on the Gibbs energy (West and Saunders, 2002). Enthalpy relates to the heat content of the system and is expressed as

$$H = E + PV \qquad eq. 3.9$$

where E is the internal energy (potential and kinetic) of the system, P the pressure and V the volume (West and Saunders, 2002). During a transformation (i.e. melting), the heat absorbed or evolved depends on the change in internal energy. The term PV takes account of volume changes and, if pressure is constant, the heat evolution or absorption is then directly equivalent to the change in enthalpy (West and Saunders, 2002) which can be experimentally obtained using the DSC and other methods. The internal energy can describes why solid phases are most sTable at relatively lower temperatures and liquids are more sTable at high temperatures. It is because in solids the strong atomic binding leads to low internal energy and enthalpy (West and Saunders, 2002).

When a homogenous solid solution is formed between two components A and B, the molar free energies are G_a and G_b, respectively. There is a change in Gibbs energy, ΔG_{mix}, when the solution is formed (West and Saunders, 2002):

$$\Delta G_{mix} = \Delta H_{mix} - T\Delta S_{mix} \qquad eq. 3.10$$

where ΔH_{mix} is the heat of solution and ΔS_{mix} is the entropy difference between the mixed and unmixed conditions (randomness of the system). Entropy is related to randomness of the system by the Boltzman equation (West and Saunders, 2002)

$$S = k \ln W \qquad eq. 3.11$$

where k is the Boltzman's constant and W is a measure of randomness. Using Stirling's approximation, entropy can be expressed (West and Saunders, 2002):

$$\mathrm{S} = -\mathrm{Nk}(\mathrm{x_a} \ln \mathrm{x_a} + \mathrm{x_b} \ln \mathrm{x_b}) = -\mathrm{R}(\mathrm{x_a} \ln \mathrm{x_a} + \mathrm{x_b} \ln \mathrm{x_b}) \qquad eq. 3.12$$

where N is Avogadro's number, x_a and x_b are the mole fractions of A and B, respectively and R is the universal gas constant. This defines the ideal entropy change on mixing. For the case of an ideal solution, where no repulsive or attractive interactions are being considered to occur between the components ($\Delta H_{mix} = 0$) and

$$\Delta G_{mix,ideal} = RT(\mathrm{x_a} \ln \mathrm{x_a} + \mathrm{x_b} \ln \mathrm{x_b}) \qquad eq. 3.13$$

The concept of an ideal solution is typically only useful to describe the gas phase. In condensed matter (solid, liquid), there are invariably significant repulsive and attractive interactions between components. Therefore, an extension of the approach is needed and the simplest procedure for dealing with such interactions is by use of the regular solution model, where the excess heat of mixing (ΔH_{mix}^{ex}) is given by

$$\Delta H_{mix}^{ex} = \mathrm{x_a x_b} \Omega \qquad eq. 3.16$$

where Ω is the regular solution interaction parameter and is related to the interaction energies of the bonds between A and B components (West and Saunders, 2002). A positive value of Ω corresponds to repulsive interactions while a negative value corresponds to attractive interactions. The Gibbs energy then becomes

$$\Delta G_{mix}^{ex} = \mathrm{x_a x_b}(\mathrm{M} - \mathrm{NT}) \qquad eq. 3.15$$

where M is equivalent to ΔH_{mix}^{ex} and N is ΔS_{mix}^{ex}.

There exists a large amount of data on mixing and excess properties for common ion binary alkali halide systems, in both the liquid and solid states that lack critical evaluation of the data (Sangster and Pelton, 1987). Evaluating the data allow discrepancies among various sets of data to be resolved and uncertain phase boundaries can often be estimated with good precision and conversely, some reported phase boundaries can be rejected as being inconsistent with the thermodynamic properties of the system. Computer coupled thermodynamic phase diagram analysis can assist in estimating ternary and higher order phase diagrams from binary systems.

Sangster and Pelton (1987) have developed excess thermodynamic functions for the alkali halide binary system based on the conformal ionic solution theory (Blander, 2000). Some of the systems developed by Sangster and Pelton (1987) are important in electrorefining because the electrolyte of the electrorefiner is made up of the eutectic alkali halide, LiCl-KCl. A discussion on the development of equations for excess functions of free energy, enthalpy (heat of fusion) and entropy will be given based on work done by Sangster and Pelton (1987, 1991). Followed by a discussion on the application of the excess terms developed from experimental data for binary systems. The binary systems are important in predicting the thermodynamic properties of a ternary system.

For equilibrium between a solid and a liquid phase in a binary system with components A and B, the Gibbs energy of fusion of A at T ($\Delta_{fus}G_A^{\circ}$) may be written as (Sangster and Pelton, 1987):

$$RT\ln a_A^l - RT\ln a_A^s = -\Delta_{fus}G_A^{\circ} \qquad eq. 3.17$$

where a_A^l and a_A^s are the activities of A on the liquidus and solidus at temperature T. Setting the ideal activities equal to the mole fractions x^l (liquid) and x^s (solid) the Gibbs energy of fusion may written

$$RT\ln\frac{x_A^l}{x_A^s} + G_A^{ex(l)} - G_A^{ex(s)} = -\Delta_{fus}G_A^{\circ} \qquad eq. 3.18$$

Where $G^{ex(l)}$ and $G^{ex(s)}$ are the partial excess Gibbs energies of A in the liquid and solid. These are zero in an ideal solution and note that

$$G_A^{ex(l)} = RT\ ln\ \gamma_A^l \qquad eq. 3.19$$

where γ^l is the activity coefficient in the liquid. If the Gibbs energies of fusion are known, and if the excess Gibbs energies are also known as functions of temperature and composition, then these two equations can be solved simultaneously by numerical methods to calculate the liquidus and solidus lines. Conversely, if the liquidus lines and solidus are known along with the excess Gibbs energies for one phase, then the excess Gibbs energies for the other phase can be calculated (Sangster and Pelton, 1987).

The integral excess Gibbs energy G^{ex} is related to the partial excess Gibbs energies by the following equation:

$$G^{ex} = x_A G_A^{ex} + x_B G_B^{ex} \qquad eq. 3.20$$

Conversely, the partial properties can be obtained from the integral property from the following equation (Sangster and Pelton, 1987):

$$G_i^{ex} = G^{ex} + (1 - x_i)\frac{dG^{ex}}{dx_i} \qquad eq. 3.21$$

where *i* represents either A or B.

The excess Gibbs energy can be written as

$$G^{ex} = H^{ex} - TS^{ex} \qquad eq. 3.22$$

where H^{ex} and S^{ex} are the excess enthalpy and entropy respectively. In most cases, it can be assumed that H^{ex} and S^{ex} are independent of temperature.

Polynomial expressions can be used to express excess properties of systems. For phase (liquid and solid) with extended ranges of solubility, H^{ex} and S^{ex} may be expanded as polynomials in the mole fractions as follows (Sangster and Pelton, 1987):

$$H^{ex} = x_A x_B (h_o + h_i x_B + h_2 x_B^2 + \cdots) \qquad eq. 3.23$$

$$S^{ex} = x_A x_B (s_o + s_i x_B + s_2 x_B^2 + \cdots) \qquad eq. 3.24$$

$$G_A^{ex} = RT\, ln\gamma_A = H_A^{ex} - TS_A^{ex} \qquad eq. 3.25$$

Where the h_o, h_i , s_o and s_i are empirical coefficients. Alkali halide solutions have shown that the enthalpic term H^{ex} in equation 3.22 is generally larger in magnitude than the entropic term TS^{ex}. Sometimes entropic data are not available, thus, it is possible to assume that $S^{ex} = 0$ and that G^{ex} is temperature independent (Sangster and Pelton, 1987). As a general rule, the larger the cations and/or anions and the smaller the difference between the radii of the two cations in a common anion binary system, the more closely the above approximations (one or two-term polynomial expansions; $S^{ex} = 0$) are obeyed.

3.4.4 Conformal Ionic-Solution Theory

Developed by Reiss et al., (1962), the conformal ionic solution theory was first applied to binary molten salt systems which led to the important conclusion that the excess free energy of mixing of an ionic mixture could be represented by a simple polynomial. This theory is important because it is the only system valid for ionic systems with long range interactions (Blander, 2000). Sangster and Pelton (1987) used the conformal ionic solution theory along with excess energy data generated by Kleppa and numerous others to develop excess energy equations that can be used to describe ternary molten salt systems.

In cases with limited solid solubility Equation 3.19 was used under the assumption of Henrian solid behavior (limited solid solubility of only a few mole percent), to calculate excess Gibbs energies along the A and B liquidus lines. Combining excess Gibbs energies with the already fitted calorimetric liquid enthalpies permitted the excess liquid entropy $S^{ex(l)}$to be calculated and then smoothed by representation as a one or two member polynomial.

The heat of mixing data for binary alkali halide systems was done using a modified conformal solution theory and was developed by Reiss et al (1962). This model assumes (1) the role of long range coulomb potential is to create a locally ordered structure, so that on average a negative ion is surrounded by positive ions and vice versa. (2) Only short-range interactions between unlike ions are of importance. This is justified by the local structure and by the repulsive Coulomb potential between ions of like sign. The enthalpy of mixing is given as (Sangster and Pelton, 1991)

$$H_{mix} = H_{mix}^{ideal} + H^{ex} = H^{ex} \qquad eq. 3.26$$

Since

$$H_{mix}^{ideal} = 0 \qquad eq. 3.27$$

The excess enthalpy and entropy are expressed as Legendre polynomials in the mole fractions X_A and X_B of the components as follows (Sangster and Pelton, 1991):

$$H^{ex} = X_A X_B[a_o + a_1(2X_B - 1) + a_2(6X_B^2 - 6X_B + 1)] \qquad eq. 3.28$$

$$S^{ex} = X_A X_B[b_o + b_1(2X_B - 1) + b_2(6X_B^2 - 6X_B + 1)] \qquad eq. 3.29$$

The empirical coefficients, a_i and b_i can be calculated thermodynamically using integral and partial properties of the binary liquid. Table 3.5 shows the empirical coefficients used for the excess enthalpy and entropy equation of LiCl-NaCl, LiCl-KCl, and NaCl-KCl binary systems. These values in Table 3.5 are used in the polynomial equations for excess entropy and enthalpy of liquids described in the next section.

Table 3.5: Excess enthalpy and entropy of the liquid state as Legendre polynomials (Sangster and Pelton, 1987)

System (A-B)	**a_o**	**a_1**	**a_2**	**b_o**	**b_1**	**b_2**
LiCl-NaCl	-4868	0	0	0	0	0
LiCl-KCl	-17758	189	0	-5.148	-2.479	0
NaCl-KCl	-2189	136	0	0	0	0

For Henrian solid solutions of a few mole percent of one component in the other, it was assumed that the activity of the solvent is ideal (i.e. Raoultian) and that the activity coefficient of the solute is independent of the composition (Sangster and Pelton, 1991). The excess partial Gibbs free energy of the solute was represented by the expression

$$G_i^{ex} = RTln\gamma_i = constant \qquad eq. 3.30$$

In which it was assumed that G_i^{ex} is independent of temperature. In the case of simple common-ion ternary molten salt solution, in which G^{ex} of the binaries can be well represented by simple polynomial expansions contain "geometric" models, which are based on regular solution theory, proved successful in estimating ternary properties from binaries (Sangster and Pelton, 1991). Two types of models are illustrated in Figure 3.13. In the symmetric, Kohler equation, G^{ex} at point p in the ternary is related to the binary values at points a, b, and c:

$$Kohler\ eq. \qquad G_p^{ex} = (1 - X_C)^2 G_c^{ex} + (1 - X_A)^2 G_a^{ex} + (1 - X_B)^2 G_b^{ex} \qquad eq. 3.31$$

where X_A, X_B, X_C are the component mole fractions. The Kohler equation (symmetric approximation) is appropriate for liquid solutions when all three components are common-ion salts of the same charge. In the asymmetric or Toop equation

$$Toop\ eq. \qquad G_p^{ex} = \frac{X_A}{X_A + X_C} G_c^{ex} + \frac{X_C}{X_A + X_C} G_a^{ex} + (1 - X_B)^2 G_b^{ex} \qquad eq. 3.32$$

is used for ternary solid solution in which components A and C are miscible at all concentrations but in which B is only sparingly soluble (Sangster and Pelton, 1991). The factors multiplying each binary excess Gibbs energy in the Kohler and Toop equations are obtained from regular solution theory such that these equations are exact if the ternary solution is strictly regular (Sangster and Pelton, 1991).

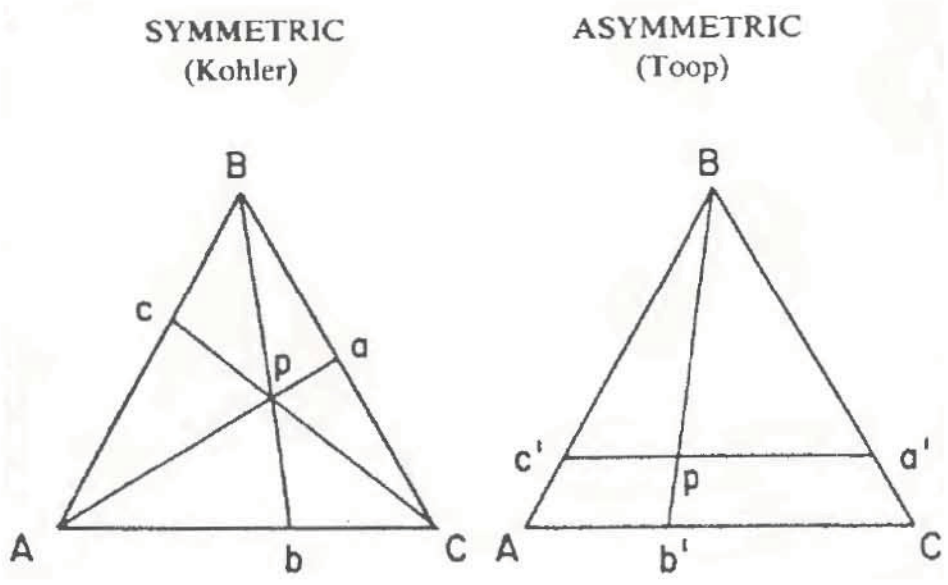

Figure 3.13: Composition triangle illustrating the geometrical basis of the Kohler and Toop equations for estimating ternary solution properties from those of the binaries (Sangster and Pelton, 1991) used with permission from Springer

The reason that simple equations such as the Kohler and Toop equations, which are based on the regular solution model, give good predictions in ionic systems is that the basic assumptions of regular solution theory (additive of pair-bond energies, small excess entropy) are satisfied in ionic systems in which columbic forces predominate (Sangster and Pelton, 1991). It is possible to extend the Kohler and Toop equations to more complex systems. There are some ternary systems in which a correction factor needs to be added to the ternary Gibbs energy expression to bring the calculated and reports diagrams into coincidence.

3.4.5 Application of Conformal Ionic Theory

It has been shown that thermodynamic binary systems can be used to predict thermodynamic properties of a ternary common-ion alkali halide system (Sangster and Pelton, 1991). A simple example using the Kohler equation will be shown using the binary phase system thermodynamics for KCl-LiCl, KCl-NaCl, and LiCl-NaCl. This is a useful technique that uses more prevalent binary data to make predictions of the ternary system KCl-LiCl-NaCl. The general method is useful for other systems as well and minimizes the amount of data needed to predict the properties of other complex systems.

KCl(A)-LiCl(B)

The excess enthalpy (heat of mixing) of the liquid has been reported from solid-liquid mixing experiments at 740°C. From the experimental data the equation for excess enthalpy of LiCl-KCl is (Hersh and Kleppa, 1965)

$$H^{ex}_{KCl-LiCl}(l) = x_A x_B(-17570 - 377x_B)\, J\, mol^{-1}$$

And the excess entropy term is (Sangster and Pelton, 1987)

$$S^{ex}_{KCl-LiCl}(l) = x_A x_B(-7.627 + 4.958x_B)\, J\, mol^{-1}K^{-1}$$

$$G^{ex}_{KCl-LiCl}(l) = H^{ex}_{KCl-LiCl}(l) - TS^{ex}_{KCl-LiCl}(l) = x_A x_B(-17570 - 377x_B) - T[x_A x_B(-7.627 + 4.958x_B)]$$

KCl-NaCl

The excess enthalpy of the liquid has been measured at 810°C by direct calorimetry and the results yield the excess enthalpy equation (Sangster and Pelton, 1987)

$$H^{ex}_{KCl-NaCl}(l) = x_A x_B(-2050 - 272x_B)\, J\, mol^{-1}$$

$$S^{ex}_{KCl-LiCl}(l) = 0\, J\, mol^{-1}K^{-1}$$

$$G^{ex}_{KCl-NaCl}(l) = x_A x_B(-2050 - 272x_B)\, J\, mol^{-1}$$

LiCl-NaCl

The excess enthalpy of the liquid state was obtained by calorimetric solid-liquid mixing experiments at 740°C, yielding a equation for excess enthalpy of (Sangster and Pelton, 1987)

$$H^{ex}_{LiCl-NaCl}(l) = -4686x_A x_B\, J\, mol^{-1}$$

The system was treated as one with continuous solid solution at the liquidus temperature instead of having a eutectic. A phase diagram was calculated assuming the excess Gibbs energy was equal to the excess enthalpy (Sangster and Pelton, 1987)

$$G^{ex}_{KCl-NaCl}(l) = -4686x_A x_B\, J\, mol^{-1}$$

It has been shown numerous times in literature (Sangster and Pelton, 1991, Richards and Meldrum, 1917) that there exists a eutectic melting composition in the KCl-LiCl-NaCl ternary salt. Using the equations for excess enthalpy, entropy, and free energy from the binary KCl-LiCl, KCl-NaCl, and

LiCl-NaCl the liquidus temperature of the eutectic 0.36KCl-0.55LiCl-0.09NaCl can be verified using the Kohler interpolative method for the liquid phase. No ternary correction term was used in the calculation. The ternary eutectic can be seen in Figure 3.14 which is a ternary liquidus projection for KCl-LiCl-NaCl calculated using the thermodynamic data from the binary systems listed above. Using the Kohler equation, based on three binary systems, a eutectic temperature of 343°C and a composition of 0.36KCl-0.55LiCl-0.09NaCl was calculated.

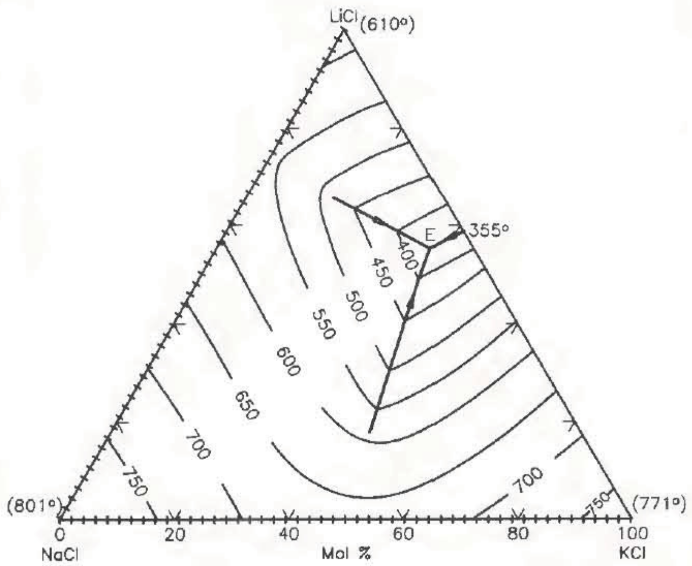

Figure 3.14: KCl-LiCl-NaCl ternary phase diagram (Sangster and Pelton, 1991) used with permission from Springer

The Kohler equation works well with common-ion binary alkali halides because the ions in consideration are of similar ionic radius and have similar interaction parameters (Sangster and Pelton, 1991). This is not the case for larger ions such as rare earth elements. For rare earth elements it may be possible to take the concept of using binary thermodynamic properties to calculate ternary salt thermodynamic properties.

3.4.6 Temkin Model

A quick way to estimate properties of binary systems is the Temkin Model used for studying the thermodynamic properties of a system the concept of an ideal solution is useful in that an ideal solution is characterized by the property that if the liquid of a pure component at temperature and pressure of the solution is taken as the standard state, the activity of the component in solution is equal to its mol fraction (for each component Raoult's Law holds at all concentrations) over a certain temperature range (Temkin, 1945). Not all solutions behave ideally, some deviate either positively, which, if large enough can lead to the formation of miscibility gaps in the liquid state (Franzosini and Sanesi, 1983) or negatively from ideality. The deviations can be expressed as activity coefficients. By assuming that a solution behaves perfectly it may be possible to approximate, the conditions of chemical equilibrium in solution on the basis of free energies of the pure substances (Temkin, 1945).

Constructing phase diagrams can take a lot of experimental work and time. Sometimes it can be beneficial to model the behavior of the salt as a function of composition. In 1945, Temkin came up with a model that suggests the cations and anions in an ionic melt are considered to be arranged (similar to what occurs in an ionic crystal structure) in two statically distinct although mechanically non-separable sub-lattice like assemblies, in either of which permutations of only cations or only anions may take place (Franzosini and Sanesi, 1983).

If there is no mixing in the salt the total entropy, degree of disorder, is shown by adding the entropy of the cations to the entropy of the anions.

$$S = S^+ + S^- \qquad eq. 3.33$$

An example of the Temkin Model for a binary mixture of two monovalent cations A^+ and B^+ and two monovalent anions X^- and Y^- , which describes the goes as follows:

$$AX + BY \leftrightarrow AY + BX \qquad eq. 3.34$$

For an ideal system the free energy of mixing is given by:

$$\Delta G_m = -T\Delta S_m = RT(n_A lnX_A + n_B lnX_B + n_X lnX_X + n_Y lnX_Y) \qquad eq\ 3.35$$

The Temkin model assumes an ideal mixture of both anions and cations, with the ionic fraction defined as:

$$X_{A^+} = \frac{n_{A^+}}{n_A + n_B}, \qquad X_{B^+} = \frac{n_{B^+}}{n_A + n_B}, \qquad X_{X^-} = \frac{n_{X^-}}{n_X + n_Y}, \qquad X_{Y^-} = \frac{n_{Y^-}}{n_X + n_Y} \qquad eq\ 3.36$$

where n_{A^+} is the number of A^+ ions in solution and the denominator is the sum of all positive ions. For any number of monovalent species the relationship for cationic species is:

$$X_{A^+} = \frac{n_{A^+}}{\sum n_{i^+}} \qquad eq\ 3.37$$

While the relationship for anionic species is:

$$X_{X^-} = \frac{n_{X^-}}{\sum n_{j^-}} \qquad eq\ 3.38$$

Inserting the cationic fraction (eq 3.37) and anionic fraction (eq 3.38) into the equation for an ideal mixture (eq 3.35) but using c_i to represent the cationic species and a_j to represent the anionic species the free energy of mixing is:

$$\Delta G_m = -T\Delta S_m = RT\left(\sum_{c_i} N_{c_i}\ln(N_{c_i}) + \sum_{a_i} N_{a_j}\ln\left(N_{a_j}\right)\right) \qquad eq\ 3.39$$

$$\Delta H_m = 0;\ \text{ideal solutions}$$

The Temkin Model can approximately predict the activity of molten salt mixtures by assuming they are completely ionized. The strong Columbic forces in a molten salt lead to alternating charges so that anions are encompassed by cations and vice versa (Blander, 2000). The activity For a Temkin ideal solution the general equation is:

$$a^{id}_{A_xB_y} = (N_A)^x(N_B)^y \qquad eq\ 3.40$$

An example of estimating the activity of LiCl in 0.1mol KCl using Temkin's model is shown:

$$a^{id}_{A_xB_y} = (N_A)^x(N_B)^y = a_{LiCl} = (N_{Li})^+(N_{Cl})^- = \left(\frac{n_{Li}}{n_{LiCl} + n_{KCl}}\right)\left(\frac{n_{Cl}}{n_{LiCl} + n_{KCl}}\right) =$$

$$\left(\frac{0.9}{0.9 + 0.1}\right)\left(\frac{0.9 + 0.1}{0.9 + 0.1}\right) = 0.9$$

The activity can be used to calculate the melting temperature of the system by rearranging

$$\ln a_{KCl} = \frac{-\Delta H_{f_{KCl}}}{R}\left(\frac{1}{T} - \frac{1}{T_{f_{KCl}}}\right) \qquad eq\ 3.41$$

Where, a, is the activity, ΔH_f is the enthalpy of formation, T is the temperature, and T_f is the temperature of formation. Solving for T will yield the liquidus temperature.

This model became more popular when Flood and Urnes (1954) applied it to the KCl-$MgCl_2$ system. This system is assumed to be ideal but with the formation of complexes. Here, it is assumed that all ionic species are known in the system of interest (Moore, 1990). Using the ideal Temkin model for the KCl-$MgCl_2$ system gives the activity of KCl as

$$KCl + MgCl_2 \rightarrow K_2MgCl_4 \qquad eq\ 3.42$$

$$a_{KCl} = (N_{K^+})(N_{Cl^-}) = \left(\frac{n_{K^+}}{n_{K^+} + n_{Mg^+}}\right)\left(\frac{3n_{Cl^-}}{3n_{Cl^-}}\right) = \left(\frac{n_{KCl}}{n_{KCl} + n_{MgCl_2}}\right)(1) = N_{KCl}$$

Applying the Temkin model to the phase diagram as in Figure 3.15 (dashed line), it is clear that it does not accurately explain the phase diagram for KCl-$MgCl_2$ because it does not account for the formation of the $MgCl_4^{-2}$ complex. However, by assuming KCl reacts quantitatively with $MgCl_2$ to form $MgCl_4^{-2}$, which has been confirmed by Raman spectroscopy (Øye, 2000), The ideal activity of KCl is given

$$MgCl_2 + 2Cl^- \rightarrow\ MgCl_4^{-2} \qquad eq\ 3.43$$

$$KCl\ \rightarrow K^+ + Cl^- \qquad eq\ 3.44$$

$$a_{KCl} = (N_{K^+})(N_{Cl^-}) = \left(\frac{n_{K^+}}{n_{K^+}}\right)\left(\frac{n_{Cl^-}}{n_{Cl^-} + n_{MgCl_4^{-2}}}\right) = (1)\left(\frac{n_{KCl} - 2n_{MgCl_2}}{n_{KCl} - 2n_{MgCl_2} + n_{MgCl_2}}\right) =$$

$$= \left(\frac{n_{KCl} - 2n_{MgCl_2}}{n_{KCl} - n_{MgCl_2}}\right) = \left(\frac{N_{KCl} - 2(1 - N_{KCl})}{N_{KCl} - (1 - N_{KCl})}\right) = \frac{3N_{KCl} - 2}{2N_{KCl} - 1}$$

This activity function as seen in Figure 3.15 (solid line) predicts the liquidus temperature with good agreement to the phase diagram for KCl-$MgCl_2$.

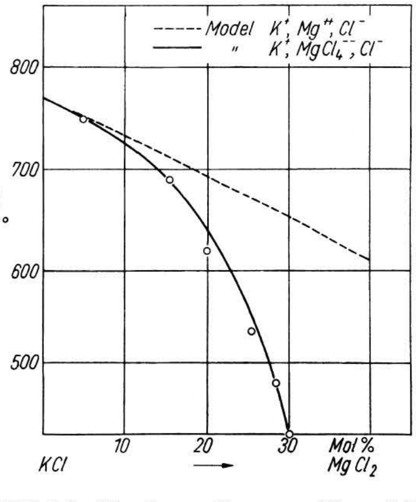

Figure 3.15: The KCl side of the KCl-$MgCl_2$ phase diagram (Øye, 2000)

4. MATERIALS AND METHODS

The research was performed in the Water Chemistry Laboratory (WCL), Building 768B, at MFC of the INL. The samples simulate the electrolyte in the Mk-IV ER at set points during FFTF and INTEC fuel processing. Two samples represent the salt during FFTF processing, and seven samples represent the salt during INTEC fuel processing. Points from which the samples were taken are shown on Figure 4.1, represented by red diamonds (♦). The batch number is given for both FFTF (1-27) and INTEC (28-192) fuels (abscissa) versus the weight fraction (ordinate). Figure 4.1 shows the composition of the salt changing with respect to the sodium and FP concentrations. The TRU (~0.2 wt%) and uranium (~0.5 wt%) concentrations remain somewhat constant.

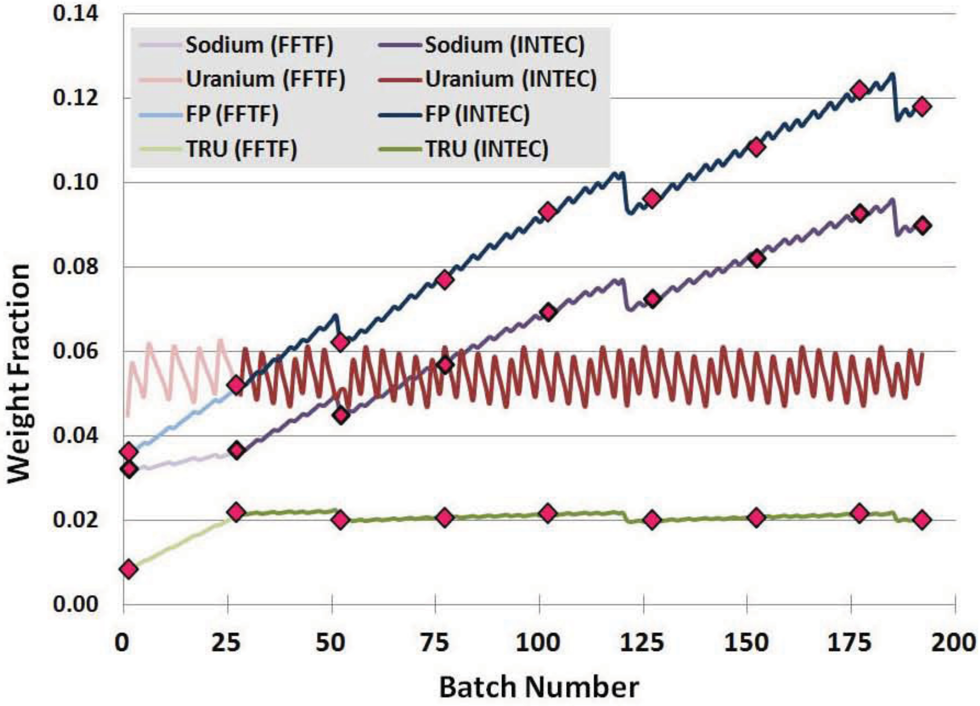

Figure 4.1: Change of salt composition during fuel processing

Each sample will have a varying composition of impurity elements in order to accurately represent the electrolyte during fuel processing. Target impurities being studied were uranium, plutonium, fission products (Sr, Sm, Pr, La, Ba, Ce, Cs, and Nd) and sodium. These impurities, along with the LiCl-KCl electrolyte, represent ~99% of the salt in the Mk-IV ER. Gadolinium (Gd) was used as a surrogate for uranium and plutonium to keep the experiments non-radiological. Strontium was used in the place of barium since barium is a Resource Conservation and Recovery Act (RCRA) metal, which would make the disposal of wastes more difficult.

The composition of the salt changes as the amount of fuel processed increases. There are many factors that will affect composition of the salt in the Mk-IV, such as:

- Type of fuel being processed. For this study it will be FFTF and EBR-II driver fuel
- Number of fuel batches run
- Amount of heavy metal fuel in each batch
- If the species will be deposited on the cathode or absorbed in the salt, or possibly absorbed in the cadmium pool.

4.1 Sample Preparation

The sample preparation involved three steps: (1) calculations, (2) measuring and melting, and (3) homogenization. The first step involved calculating the exact quantities of individual salts needed to prepare a salt mixture representative of the composition of the simulated ER electrolyte. Steps 2 and 3 were performed under an inert argon atmosphere in an MBraun® Labmaster DP glovebox, (see Figure 4.2). The oxygen and moisture concentrations were maintained below 0.1 parts per million (ppm) for the duration of this experiment unless otherwise noted.

Figure 4.2: Argon atmosphere, moisture and oxygen controlled glovebox located in WCL

The chemicals used in this research had a purity of 99.99% or greater except for samarium chloride ($SmCl_3$) which had a purity of 99.9%. All chemicals were purchased from Sigma Aldrich or Alfa Aesar and received in sealed glass ampoules packaged under an argon atmosphere. Once received the ampoules were immediately transferred to the glovebox. A diamond file was used to score the outside of the ampoule and break it open. The chemicals were placed in labeled glass vials. All salts were stored in the glovebox due to their hygroscopic characteristics. Salts used for the experiments are listed in Table 4.1.

Table 4.1: List of salts used in this study

Chemical Name	Chemical Formula	Supplier	Purity	Product #	Lot #	Comments
Cerium (III) Chloride	$CeCl_3$	Sigma Aldrich	≥99.99%	429206	MKBB9297	Anhydrous Beads, 10 mesh
Cesium Chloride	$CsCl$	Sigma Aldrich	99.99%	449733	11991BR	Anhydrous Beads, 10 mesh
Gadolinium (III) Chloride	$GdCl_3$	Sigma Aldrich	99.99%	439770	K26W158	Anhydrous
Lanthanum (III) Chloride	$LaCl_3$	Alfa Aesar	99.999%	44322	L08N13	Ultra Dry Powder
Eutectic Lithium Chloride/ Potassium Chloride(d)	$LiCl$-KCl	Sigma Aldrich	99.99%	479330	MKBC8337	Anhydrous Beads
Neodymium (III) Chloride	$NdCl_3$	Sigma Aldrich	≥99.99%	449946	MKBB6345	Anhydrous Powder
Potassium Chloride	KCl	Sigma Aldrich	99.999	449989	MFCD000113 60	Anhydrous Beads, 10 mesh
Praseodymium (III) Chloride	$PrCl_3$	Sigma Aldrich	99.99%	298298	99096MJ	Anhydrous Powder
Samarium (III) Chloride	$SmCl_3$	Alfa Aesar	99.9%	35804	A15T006	Ultra Dry Powder
Sodium Chloride	$NaCl$	Sigma Aldrich	99.999%	450006	MKBF6003V	Anhydrous Beads
Strontium (II) Chloride	$SrCl_2$	Sigma Aldrich	≥99.99%	439665	MKBC8344	Anhydrous Powder

(d) Eutectic LiCl-KCl has a purity of 99.99% with respect to LiCl and KCl

4.1.1 Calculations

There is approximately 500 kg of electrolyte in the Mk-IV ER. This study used a 15 g surrogate sample to simulate the 500 kg inventory. More than 99 wt% of the ER salt was represented using chlorides of Li, K, Na, Nd, U, Pu, Cs, Ce, La, Pr, Sm, Ba, and Sr. Weighted atomic masses for the top fourteen elements (including Cl) in the salt were calculated based on (a combination of measured and modeled) isotopic abundances in the Mk-IV salt. These weighted atomic masses were used to calculate the weight percent (wt %) of each element in the salt.

The weight percentages of the top fourteen elements present in the Mk-IV ER electrolyte were used to calculate the amount of each metal chloride needed to make the 15 g simulation sample for DSC analysis. The 15 g simulation sample contains the same elements in the same wt% as the original

Mk-IV salt composition from which the simulation sample is based. To keep this research non-radiological and RCRA metal free, Gd is used in place of U and Pu and Sr is used in place of Ba.

The composition and the elements present in the Mk-IV ER salt after batch 25 of INTEC fuel (INTEC B25) has been processed is shown in Table 4.2. The rank of the element (column 1) is based on the abundance of the element in the ER salt: chlorine (Cl) is the most abundant; potassium (K) is the second most abundant, etc. In equation 4.1, the wt% of metal (Me) in the salt is calculated for K:

$$\frac{Mass\ of\ Me\ (g) in\ salt}{Metal\ in\ salt\ (g)} = \frac{84430 g\ of\ K\ in\ salt}{444300\ g - mass\ of\ Cl} \times 100 = 45.35\ wt\%\ K \quad (eq\ 4.1)$$

The molecular weight (MW) of Me is calculated based on different element isotopes and their abundance (modeled and measured) in the Mk-IV ER. Li, K, Na and Cs are assumed to be in a +1 oxidation state; Ba and Sr in the +2 oxidation state; and Nd, U, Pu, Ce, La, Pr, Sm are present in the salt in the +3 oxidation state. Equation 4.2 shows the calculations for determining the amount of metal chloride ($MeCl_x$), in this case KCl, needed to make a 15 g surrogate sample. The subscript x, in $MeCl_x$ represents the number of chloride ions needed to balance the valence of the metal cation.

$$g\ MeCl_x\ Sample = \frac{\left[\left(\frac{MW\ of\ MeCl_x}{MW\ of\ Me}\right) \cdot wt\ of\ Me\ in\ salt\right]}{\sum\left[\left(\frac{MW\ of\ MeCl_x}{MW\ of\ Me}\right) \cdot wt\ of\ Me\ in\ salt\right]} \times 15 grams \quad (eq\ 4.2)$$

$$\frac{\left[\left(\frac{74.25 \frac{g\ KCl}{mol\ KCl}}{39.06\ \frac{g\ K}{mol\ K}}\right) \cdot 84{,}431 g\ K\ in\ salt\right]}{\sum\left\{\left[\left(\frac{74.25 \frac{g\ KCl}{mol\ KCl}}{39.06\ \frac{g\ K}{mol\ K}}\right) \cdot 84{,}430 g\ K\right] + \left[\left(\frac{262.8 \frac{g\ UCl_3}{mol\ UCl_3}}{157.3\ \frac{g\ U}{mol\ U}}\right) \cdot 24{,}290 g\ U\right] + \ldots \left[\left(\frac{159.2 \frac{g\ SrCl_2}{mol\ SrCl_2}}{88.78\ \frac{g\ Sr}{mol\ Sr}}\right) \cdot 1{,}161 g\ Sr\right]\right\}} \times 15\ grams$$

$$= \mathbf{5.440 g\ KCl}$$

The columns in Table 4.2 with the word "actual" are based on a real, prepared simulated salt sample. The masses are grams (g) of $MeCl_x$. For example, 1.685 g of NaCl was used in the 15 g sample to represent the wt% of Na present in the Mk-IV ER. Table 4.2 shows that the ER salt contains 10.55 wt% Na (column 4), the 15 g simulated salt sample also contains 10.55 wt% Na (column 8). The MW of Gd is used instead of U because $GdCl_3$ is substituted for UCl_3 so that the sample is non-radiological. The same concept applies for $PuCl_3$. Nonetheless, the final sample contains the same or nearly the same wt% of each element as the original Mk-IV ER electrolyte it was modeled after. This can be verified by comparing the columns titled: wt% Me in ER salt and actual wt% Me in 15 g sample. Equation 4.3 shows how to calculate the actual wt% of Me in 15 g sample.

$$wt\%\ of\ Me\ in\ 15g\ Sample$$

$$= \frac{\left[\left(\frac{MW\ of\ Me}{MW\ of\ MeCl_x}\right)\cdot mass\ of\ MeCl_x\ in\ 15g\ Sample\right]}{\sum\left[\left(\frac{MW\ of\ Me}{MW\ of\ MeCl_x}\right)\cdot mass\ of\ MeCl_x\ in\ 15g\ Sample\right]} \times 100 \quad (eq\ 4.3)$$

The wt% of Me in ER salt (column 4) and the wt% of Me in the 15 g sample (column 8) should be similar if not exactly the same and can be seen in Table 4.2.

Table 4.2: Composition of Mk-IV salt and 15 g simulated sample after batch 25 of INTEC fuel was processed

INTEC B25 Rank	**Element**	**Mass of Me in ER salt (g)**	**wt% Me in ER salt (%)**	**Calculated Mass in 15 g $MeCl_x$ Simulated Sample (g)**	**Actual mass of $MeCl_x$ in 15 g Sample (g)**	**Actual mass of Me in 15 g Sample (g)**	**Actual wt% Me in 15 g sample (%)**
1	Chlorine	258100					
2	Potassium	84430	45.35%	5.440	5.440	2.862	45.36%
3	Uranium (Gd)	24290	13.05%	1.376	1.376	0.8233	13.05%
4	Lithium	21870	11.75%	4.487	4.487	0.7412	11.75%
5	Sodium	19640	10.55%	1.685	1.685	0.6658	10.55%
6	Plutonium (Gd)	8790	4.720%	0.498	0.4975	0.2977	4.72%
7	Neodymium	7896	4.240%	0.463	0.4629	0.2676	4.24%
8	Cesium	5624	3.020%	0.241	0.2404	0.1905	3.02%
9	Cerium	4374	2.350%	0.259	0.2592	0.1482	2.35%
10	Lanthanum	2396	1.290%	0.143	0.1434	0.0815	1.29%
11	Praseodymium	2210	1.190%	0.131	0.1312	0.0750	1.19%
12	Samarium	1807	0.9700%	0.105	0.1044	0.0610	0.97%
13	Barium (Sr)	1668	0.9000%	0.102	0.1019	0.0565	0.90%
14	Strontium	1161	0.6200%	0.071	0.0708	0.0395	0.63%
Total		444300	100.00%	15.00	14.99	6.309	100.0%

Table 4.2 refers to the simulated salt sample labeled INTEC B25. Eight other simulated salt samples of other compositions were prepared using the same procedure and equations. Compositions for all nine samples are presented in Appendix A.

4.1.2 Measuring and Melting

Measuring and melting involves weighing the calculated amounts of metal chloride salts (eutectic LiCl-KCl, $GdCl_3$, NaCl, $NdCl_3$, CsCl, $CeCl_3$, $LaCl_3$, $PrCl_3$, $SmCl_3$, and $SrCl_2$) to make the 15 g simulated salt sample, mixing and melting them in a crucible; all handling and weighing of the chloride salts were performed in the MBraun® glovebox. To avoid contamination with other salts, all glovebox surfaces were wiped down with a clean, terry cloth towel before using the pure anhydrous metal chloride salts. Crucibles, spatulas, and weight dishes were washed with deionized (DI) water, rinsed with propanol, and dried in an oven before each use or between each 15 g sample preparation.

A total of ten salts ($GdCl_3$ in place of UCl_3 and $PuCl_3$ and $SrCl_2$ in place of $BaCl_2$) were used to make the 15 g simulated salt sample. During sample preparation the chloride salts used were weighed into a plastic weighing dish and weighed to the nearest 0.0001 g using a Mettler Toledo Analytical Balance model number MS3045/03. The analytical balance was calibrated, had an accuracy of ±0.0005 g, and was periodically auto calibrated. A 1.0000 g standard was used daily to make sure the balance was operating within the calibrated accuracy. The measured values of the 1.0000 g standard were within ±0.0003 g. The salts were weighed individually in a plastic weighing dish, combined in a nickel crucible, and mixed together with a spatula. The crucible was a 30 mL high form nickel (Ni) crucible with Ni lid. The final mass of the combined salts in the nickel crucible is approximately 15 g. Figure 4.3 shows all ten metal chloride salts mixed in a Ni crucible.

Figure 4.3: Combined metal chloride salts in Ni crucible

The Ni crucible with 15 g of salt mixture and a Ni lid were placed in a Thermo Scientific small bench top muffle furnace at 500°C for approximately one hour. The chloride salts showed no sign of reaction with the Ni crucible when heated in the furnace. At 500°C, the salt mixture should be completely molten (homogenous) as seen in Figure 4.4a for sample INTEC B25. However, this was not always the case. Some of the samples with higher concentrations of impurities, such as sample INTEC B125, did not appear to be completely molten (non-homogeneous) at 500°C, (Figure 4.4b). Sample INTEC B25 contained 33.8 wt% of impurities while sample INTEC B125 contained 51.6 wt% of impurities in the form of $GdCl_3$ (UCl_3 and $PuCl_3$), FP chlorides, and NaCl. If the sample did not look completely molten at 500°C, it was heated to 600°C and held at that temperature for 1 hr.

Figure 4.4a and 4.4b: Homogenous molten salt (INTEC B25) and non-homogeneous molten salt (INTEC B125) respectively

After one hour of heating, the crucible and sample were removed from the furnace, the sample was allowed to cool to room temperature (inside glovebox). The sample was taken out of the furnace in order to cool it quickly and to reduce the effect of zone cooling. The effects of zone cooling were reduced but not eliminated as can be seen in Figures 4.5a – 4.5d, (sample INTEC B75). The molten sample solidifies along the crucible wall seen most clearly in Figure 4.5b. The middle then solidifies as seen in Figure 4.5c until the entire sample has recrystallized into a solid ingot as seen in Figure 4.5d. There was some color variation between the top and bottom of the sample. Color variation can be seen faintly in Figure 4.5d, but is more noticeable on the actual salt ingot.

Figure 4.5a – 4.5d: INTEC B75 as molten sample cools to room temperature

Zone freezing needs to be avoided in these experiments to ensure homogeneity of the samples. Even though the sample was homogeneous in the molten state, as it cooled and recrystallized the salt sample may have segregated or "precipitated out" at different temperatures. There were possibly regions of higher LiCl-KCl concentrations near the edge of the crucible. This was evident by the light color of the edges compared to the middle and the brittleness of the ingot at the edges.

4.1.3 Homogenization

Having a homogenous sample ensures that even a minute DSC sample will represent the entire original Mk-IV ER salt sample. There are about 500 kg of salt in the Mk-IV from this study being represented using a 15 g simulated sample of the same composition; 15 g is 0.003% of 500 kg. From the 15 g simulated sample, ~10 mg of the sample will be placed in a DSC crucible for analysis. The 10 mg sample is 0.000002% of 500 kg. Since the DSC uses such a small amount of sample, it is essential to have a homogenous mixture capable of representing the entire original ER electrolyte.

The 15 g salt ingot (Figure 4.5d) is not considered a homogenous mass although it was once a homogenous molten sample in the furnace at temperatures of 500°C to 600°C. It is clear the piece of recrystallized salt ingot is not homogenous throughout (see Figure 4.6). This can be seen by the changing color of sample INTEC B75, the top is light blue-green and seems less dense and more brittle than the middle which is a darker shade of light blue; the bottom of the sample is a dark blue-grey color and looks denser than the top of the ingot.

Figure 4.6: Piece of crystallized salt showing non-homogeneity of 15 g ingot

Homogenization of the salt ingot is done by grinding the crystallized salt ingot with an agate mortar and pestle as seen in Figure 4.7 and sieving. The salt is passed through two sieves, US 40 mesh (0.422 mm) and US 100 mesh (0.152 mm) yielding a final powder sample with a particle size of 100% minus 100 mesh. The test sieves were produced and manufactured using methods and quality control procedures to assure conformity according to the ASTM E 11 standard.

Figure 4.7: Agate mortar and pestle with crushed salt

One to three grams of the original 15 g simulated salt sample was lost during the grinding and sieving process. After the salt sample was ground, it was placed in a labeled glass vial and stored in the glovebox until needed for DSC analysis. The sieves, mortar and pestle, spatulas, weighing dishes, and crucibles were transferred out of the glovebox and cleaned before the next use. Cleaning was done using soap and DI water. The clean labware was air dried overnight. The grinding and weighing tools were rinsed with propanol to remove any organic residue and baked in an oven to remove any remaining residual water.

4.2 DSC Analysis

Figure 4.8 shows the DSC setup in the WCL at MFC. The DSC includes two furnaces (silver and platinum), argon purge gas, cooler, vacuum pump, sample carrier and laptop for instrument control, data acquisition and storage. The cooler is used to keep the microbalance within the DSC cool; typically set to 25°C. The vacuum feature may be used to study samples at lower pressures, but for these studies atmospheric pressure was used and the vacuum pump was not needed. The DSC is a highly sensitive instrument, its data can be affected by a number of factors (environment, sample, etc.), these disturbances need to be mitigated as much as possible. To keep noise from the system (DSC) to a minimum, factors such as furnace atmosphere, furnace size and shape, sample carrier material, sample carrier geometry, sample placement, heating rate, speed and response of recording instrument, and thermocouple location will be the same from one sample to the another (Schindler, 2010). Particle size, thermal conductivity, heat capacity, packing density, swelling or shrinkage of sample, amount of sample, and degree of crystallinity can affect the DSC signal and can ultimately skew DSC results (Schindler, 2010).

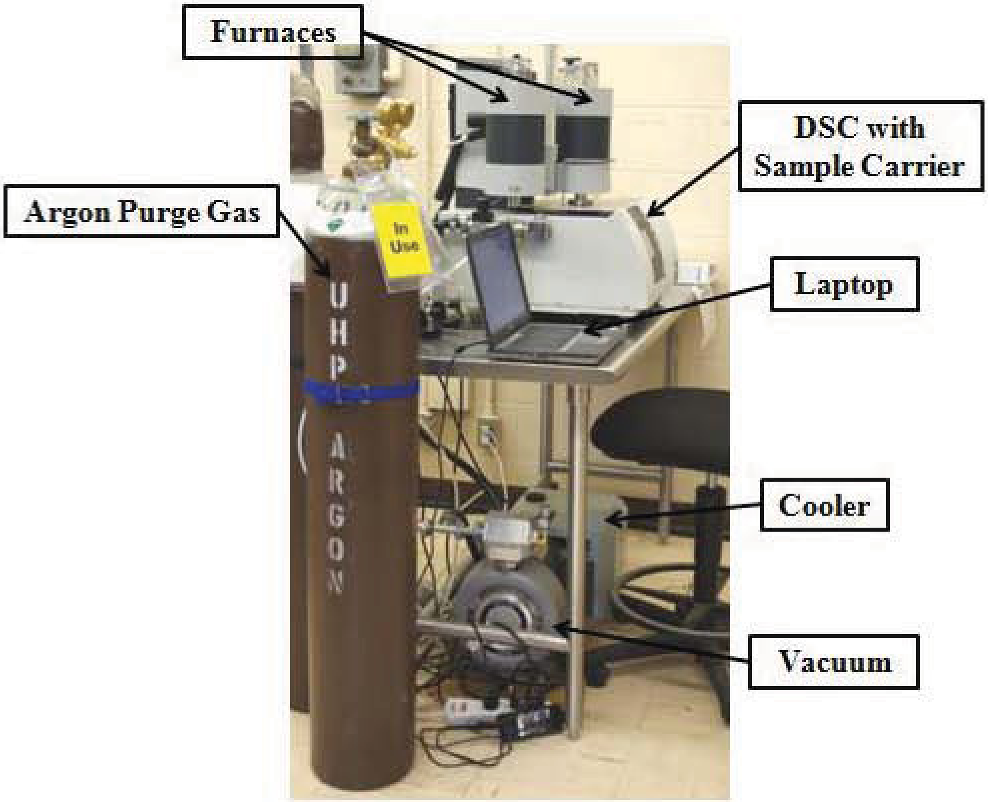

Figure 4.8: DSC setup in WCL

The DSC parameters held constant for all samples are listed in Table 4.3. Several parameters varied from sample to sample including: sample size, sample temperature range, pressure inside the sealed crucible, lab temperature, and lab vibrations. Actions were taken to ensure the variations were kept to a minimum. Some parameters such as laboratory temperature did not deviate too much from 22°C. If the deviation was greater than ±5°C DSC, then analysis would not be performed. All samples were subject to different temperature ranges depending on the transition and melting temperature range. Because some samples, such as eutectic LiCl-KCl, melt at low temperatures (~350°C), and other samples, like pure LiCl, melt over 600°C, the samples would be subjected to different temperature profiles (initial and final temperature) in the DSC to ensure the transition and melting peaks of each sample could be seen within the set temperature range. The WCL where the DSC is located added some background noise to the DSC signal. The lab had fluctuating temperature, power outages, and vibrations due to the heating and ventilation systems and nearby construction and demolition. The majority of the effects were seen on the TG curve while the DSC curve showed little effect of the lab environment.

Table 4.3: DSC parameters used in this study

Parameter	Setting
Crucible Material	Au plated Stainless Steel
Crucible Sealing Torque	2.5 N·m
Purge Gas Flow Rate	20 cm^3 min^{-1}
Protective Gas Flow Rate	20 cm^3 min^{-1}
Furnace Atmosphere	UHP Argon
Furnace Material	Platinum Furnace (0 to 1500°C)
Sample Carrier Material	Platinum/Rhodium
Thermocouple Type	Type S
Calibration	Temperature, Sensitivity
Heating/Cooling Rate	10 K min^{-1}, 2 K min^{-1}
Sample Size	10 ± 1mg

Chloride salts are hygroscopic, the DSC is not located inside a glovebox, therefore a sealed gold plated stainless steel (Au-SS) DSC crucible was used in this research. The nominal diameter of the crucible was 6 mm and it had a volumetric capacity of 27 µl. The crucible could withstand a maximum internal pressure of 100 bar and had a maximum temperature rating of 500°C. The maximum temperature rating was used more as a guideline; the crucibles were subjected to temperatures up to 800°C and performed as expected. Au-SS crucibles consist of three parts: (1) lid, (2) seal, and (3) pan (see Figure 4.9). The seal was placed on top of the pan, which contained approximately 10 mg of sample, and the lid was screwed on locking the gold seal between the pan and lid. A torque screwdriver set to of 2.5 N·m was used to create a cold weld between the gold disk and the sample pan.

Figure 4.9: DSC crucible, gold plated chrome nickel steel crucible lid, seal, and pan

As the crucible was subjected to a temperature profile, the internal pressure of the crucible increases slightly. The effect of the pressure increases as a function of increasing temperature is small; thus, it is not accounted for in these studies. For all practical purposes, the sample is assumed to be at atmospheric pressure. Calibration standards and a study of the LiCl-KCl phase diagram confirm that the pressure within the crucible remains at or very near atmospheric pressure. The samples were prepared in the inert atmosphere glovebox, loaded into the Au-SS crucible, sealed and then transferred out of the glovebox for DSC analysis in a labeled plastic bag along with a reference (empty) crucible.

The reference and sample crucibles were placed on the sample carrier in the platinum (Pt) furnace of the DSC having a temperature range from room temperature (RT) to 1500°C (the DSC is also equipped with a silver furnace (RT to 650°C) but was not used because the temperature range was not broad enough for this study). UHP argon gas was purged through the furnace during experiments. The sample and reference crucibles were subjected to the desired temperature program and data acquired and saved on the instrument laptop (Figure 4.8). The sample data file included information about the reference, sample crucible weights, sample weight, argon purge flow rate, protective gas flow rate, calibrations, heating rates, and temperature ranges.

4.3 Calibrations

Measurements with any instrument can be affected by changes in the instrument that occur over time such electronic drift and aging thermocouples (Netzsch, 2010). Calibrating is a means of establishing a set of operations using a specific set of conditions to get the most accurate data possible from the instrument when compared to a set of standards (Hohne et al., 2003). There were two types of calibrations run for this work: temperature and sensitivity. Temperature calibrations determine the accuracy of the temperature measurements made with the DSC. Sensitivity calibrations are performed to ensure the accuracy of quantitative evaluation of DSC peak areas and are very important in determining the enthalpy of experimental samples. For temperature and sensitivity calibrations, materials of high purity, for which the transformation temperatures are known, were used as calibration materials. For sensitivity calibrations, the instrument was calibrated using standards of known enthalpy (enthalpy of fusion) run under identical test conditions (crucible, atmosphere, heating rates, and sample weights) as the experimental samples (Netzsch, 2010).

A calibration must be run using no less than three standards and multiple scan rates and must encompass the temperature range in which the experimental samples will be analyzed. The calibrations must also be run using the same set of conditions as the experimental samples including purge flow rate, sample size, crucible material, and heating rate. Temperature and sensitivity calibrations were run using a set of five, high purity salt standards provided by Netzsch® from 120°C to 668°C for heating rates of 10 K min^{-1} and 2 K min^{-1}. 10 K min^{-1} is a very typical heating rate used in most literature, whereas 2 K min^{-1} is a somewhat slow heating rate that can in some instances resolve data not explicitly clear when taken at faster heating rates. Each standard was run using 10 mg ± 1 mg of sample. Details of the calibration standards are shown in Table 4.4, along with the sample size, purity, literature reported transition temperature, and the temperature range used for DSC analysis.

Table 4.4: Calibration standards, sample size, purity and temperature range used for DSC analysis

Standards	**Sample Size (mg)**	**Purity (%)**	**Literature Transition Temp (°C)**	**Temperature Range (°C)**
Benzoic Acid (C_6H_5COOH)	9.9	99.5	122.4	20 260
Rubidium Nitrate ($RbNO_3$)	9.2	99.99	164.2	80 375
Potassium Perchlorate ($KClO_4$)	9.2	≥99	300.8	150 420
Cesium Chloride (CsCl)	10.3	99.999	476.0	330 630
Potassium Chromate (K_2CrO_4)	9.3	≥99	668.0	520 800 (10K min^{-1}) 550 770 (2K min^{-1})

4.3.1 Temperature Calibration

Each standard used in the temperature calibration was subject to three heating/cooling cycles. A representative calibration curve for benzoic acid with a 2 K min^{-1} heating rate is shown in Figure 4.10. It can be seen that there is only one peak, as benzoic acid has one phase transition (solid-to-liquid, i.e. melting). The average of the onset temperatures for the three cycles was used for the onset temperature of the calibration file. Table 4.5 shows the experimental transition temperature values for the five standards used in this study obtained for 10 K min^{-1} and 2 K min^{-1} heating rates. All five standards used produced melting temperatures within 5°C of the reported literature value for the 10 K min^{-1} and 2 K min^{-1} heating rate.

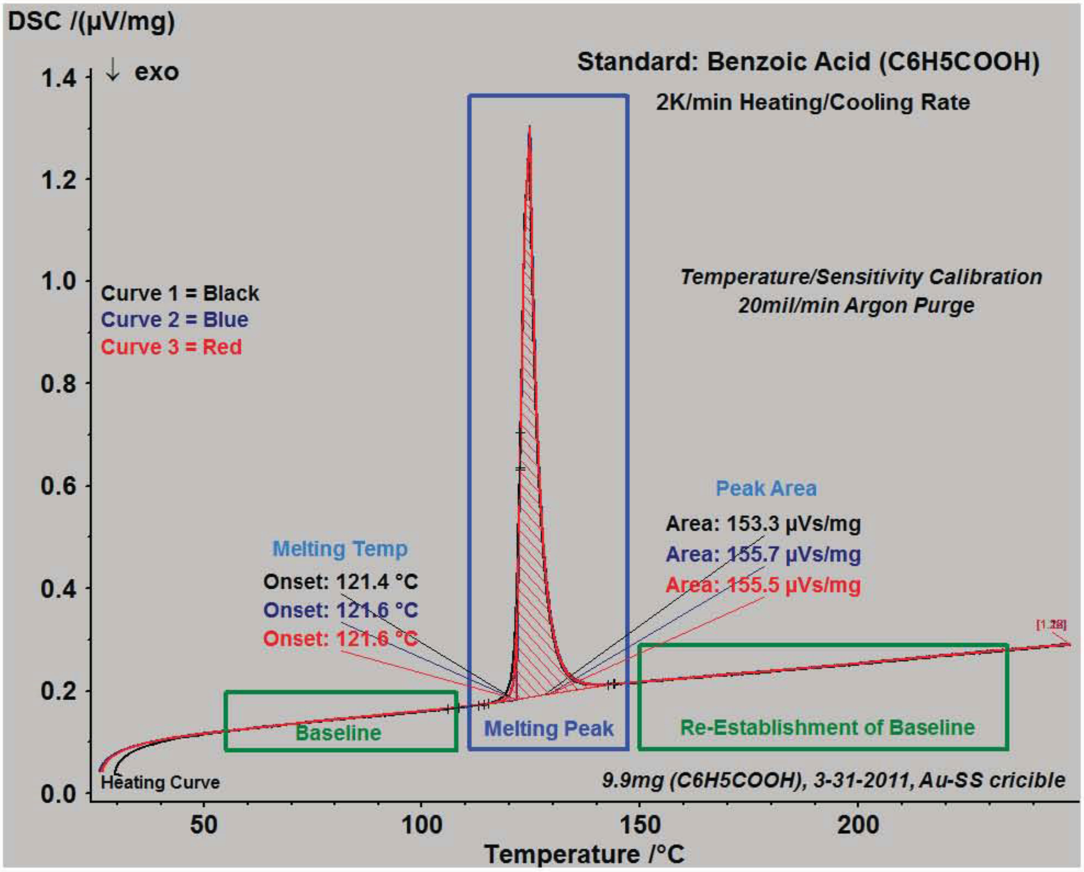

Figure 4.10: DSC curve for benzoic acid standard

Table 4.5: Experimental transition temperature values

Standard	**Cycle**	**Transition Temp, 10 K min^{-1} (°C)**	**Transition Temp, 2 K min^{-1} (°C)**
Benzoic Acid (MP=122.4°C)	1	122.6	121.4
	2	122.5	121.6
	3	122.6	121.6
	Average	122.6	121.5
$RbNO_3$ (TT*=164.2C)	1	164.2	160.1
	2	163.9	159.0
	3	163.5	158.6
	Average	163.9	159.2
$KClO_4$ (MP=300.8°C)	1	302.0	299.8
	2	302.2	300.0
	3	302.6	299.8
	Average	302.3	299.9
CsCl (MP=476.0°C)	1	475.8	474.2
	2	476.6	474.9
	3	477.0	475.0
	Average	476.5	474.7
K_2CrO_4 (MP=668.0°C)	1	664.2	663.7
	2	664.2	663.7
	3	664.2	663.7
	Average	664.2	663.7

*TT = Transition Temperature not melting temperature

Using the average values in Table 4.5, the temperature calibration curves were constructed as seen in Figure 4.11 and Figure 4.12 for 10 K min^{-1} and 2 K min^{-1} heating rates, respectively. It should be noted that a "dummy value" value was used as the last point on the 10 K min^{-1} and 2 K min^{-1} temperature calibration. It is recommended in the Netzsch calibration software to use dummy values to optimize the curve fit of the measured calibration standard. A dummy value was chosen that would decrease the slope of the red line in Figures 4.11 and 4.12. The data acquisition software has a threshold slope criteria that must be met or the calibration files cannot be loaded during sample runs. Since the temperature range for the calibration is low compared to the maximum temperature of the furnace a dummy value was chosen at 800°C that "flattened" the slope at higher temperatures. The calibration files will not be used for temperatures greater than 665°C. A dummy value was chosen that will have minimal, if any effect on the data. The $RbNO_3$ point (2nd point in Figure 4.12) is not as accurate as the other points because the temperature used was taken from a peak for a phase transformation not from a melting peak like the other standards, so kinetics are interfering with the DSC curve at this point to a small degree. The individual calibration curves for the standards, used to construct Figures 4.11 and 4.12 are presented in Appendix B.

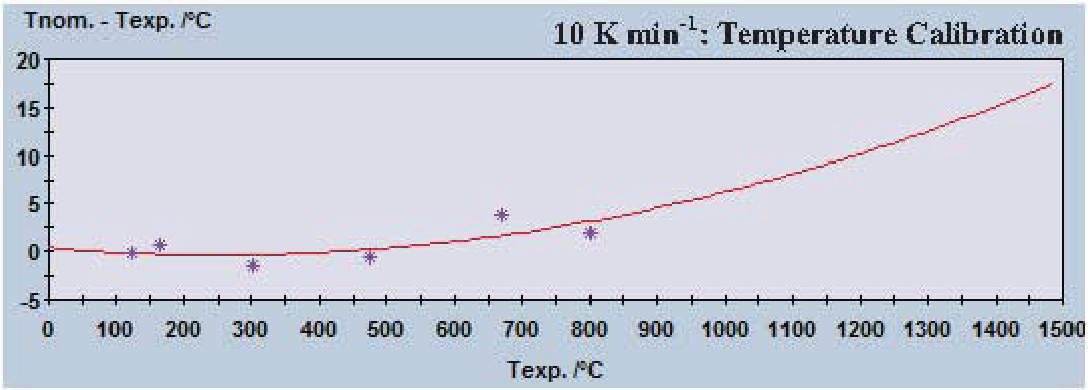

Figure 4.11: 10 K min^{-1} temperature calibration curve for Pt furnace using Au-SS DSC crucible

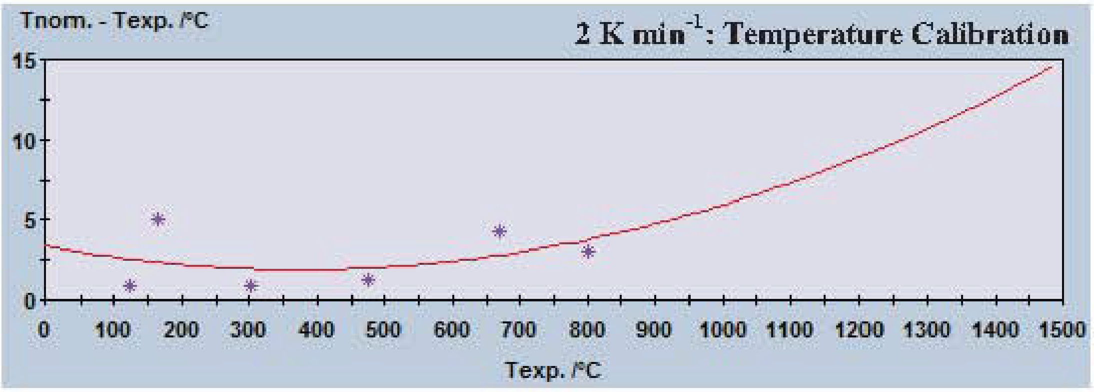

Figure 4.12: 2 K min^{-1} temperature calibration curve for Pt furnace using Au-SS DSC crucible

4.3.2 Sensitivity Calibration

A quantitative evaluation of DSC peak area can help estimate enthalpy. A sensitivity calibration, also called a heat flow rate calibration, is constructed from the same data used to make the temperature calibration. Sensitivity calibrations are dependent on the measurement conditions (crucible, atmosphere, flow rate, heating rate, sample weight). The sensitivity of the measuring system is defined as the ratio between the change of the measurement and the change of the measured quantity that creates the signal (Hohne et al., 2003). The measured quantity is the heat flow rate ($\Delta\Phi$ in mW), and the signal output is an electric voltage (ΔU in μV) yielding a sensitivity given in $\mu V\ mW^{-1}$.

Sensitivity changes with temperature (higher temperature equals less sensitive) and is applied to the experimental DSC data automatically within the software. All experimental DSC curves in which sensitivity calibration files are loaded will yield a DSC signal in units of mW mg^{-1}. By comparing the measured value to a standard value (literature value), a better understanding of the heat flow of the instrument is obtained. The standards used to make the sensitivity calibration are shown in Table 4.6 along with the experimentally obtained peak areas for each standard.

Table 4.6: Experimentally obtained peak areas for sensitivity calibrations

Standard	**Cycle**	**Peak Area, 10K min^{-1} (µVs/mg)**	**Peak Area, 2 K min^{-1} (µVs/mg)**
Benzoic Acid (-147.4 J/g)	1	158.2	153.3
	2	157.0	155.7
	3	157.4	155.5
	Average	157.5	154.8
$RbNO_3$ (-26.6 J/g)	1	27.08	26.18
	2	27.01	25.66
	3	27.32	25.75
	Average	27.1	25.9
$KClO_4$ (-104.9 J/g)	1	93.19	96.8
	2	92.63	97.03
	3	94.47	97.68
	Average	93.4	97.2
CsCl (-17.2 J/g)	1	12.26	12.68
	2	12.69	12.23
	3	12.6	12.25
	Average	12.5	12.4
K_2CrO_4 (-35.0 J/g)	1	17.4	16.45
	2	16.98	16.62
	3	16.33	16.47
	Average	16.9	16.5

The average values of the three peak areas (measured heat fluxes) for the standards were used to create a sensitivity calibration factor as a function of temperature. The sensitivity factor is used to determine the temperature-dependant proportionality factor between peak area and enthalpy and is applied automatically to experimental DSC data when the sensitivity calibration file is loaded during DSC setup. Figures 4.13 and 4.14 show the sensitivity calibration curves for 10 K min ^{1} and 2 K min ^{1} heating rates, respectively. The individual DSC curves used to construct these figures are presented in Appendix B. The sensitivity calibration curves indicate that as the temperature increases, the sensitivity of the instrument decreases. The sensitivity calibration curve was loaded into the software for each sample run to correct for the decreased sensitivity at higher temperatures. Using the sensitivity calibration the results of the peak area calculation in J g ^{1}, as compared to in µVs mg ^{1} without the calibration.

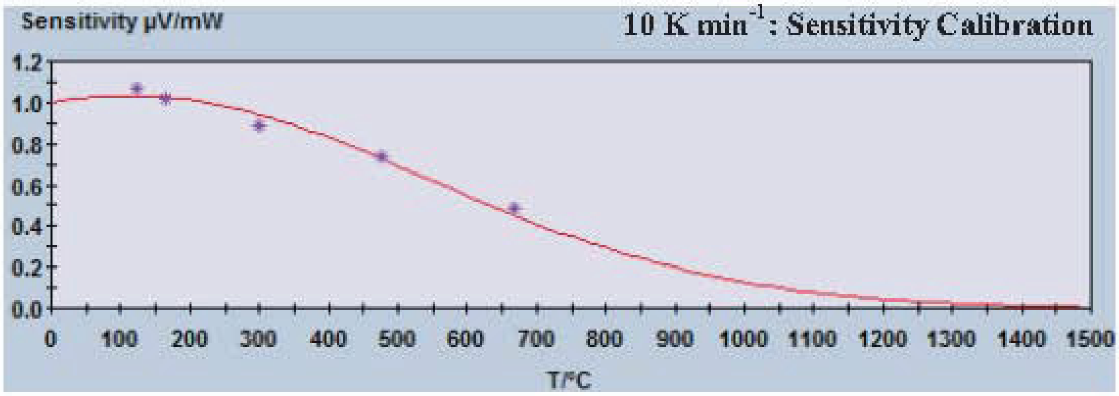

Figure 4.13: 10 K min ^{1} sensitivity calibration curve for Pt furnace using Au-SS DSC crucible

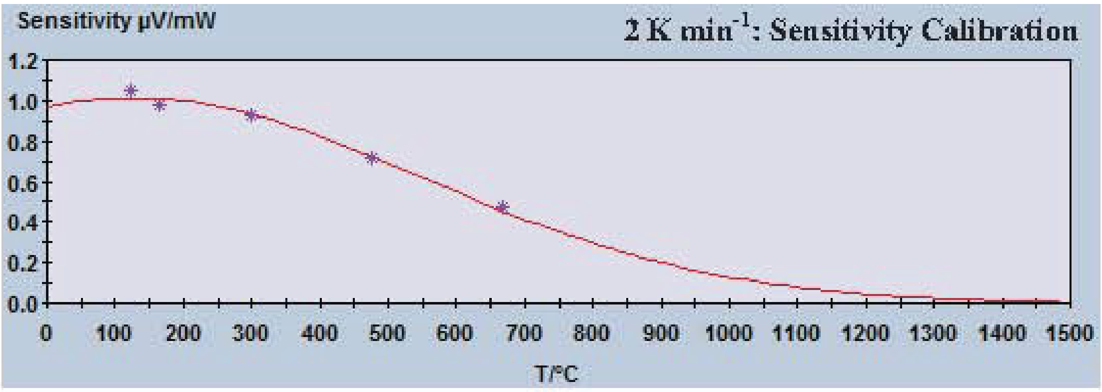

Figure 4.14: 2 K min ^{1} sensitivity calibration curve for Pt furnace using Au-SS DSC crucible

5. PRELIMINARY STUDIES: Discussion and Results

There are many factors to consider when setting up calorimetric experiments such as purge gas, flow rate, specimen mass, crucible material, and heating rate. It is important to know the effect of operating conditions on experimental results. Preliminary studies on heating rate, particle size, sample mass, and purge gas were studied, and in some instances experiments were performed to observe how the DSC curves would be affected. These studies also helped in determining the optimal operating conditions for the DSC. A study on sample homogeneity was done to ensure the DSC sample size chosen provided an accurate representation of the original mass. Baseline corrections were also studied to determine what effects, if any, the DSC system had on the acquired DSC data. Baseline experiments involved subtracting the DSC signals generated (system + sample) from the signals generated purely by the sample. Finally a study on a well known system, LiCl-KCl, was done to ensure correct interpretation of DSC curves and confirm optimal operating parameters by comparing experiential data to literature reported data.

5.1 Factors Affecting DSC Curves

There are many factors that can affect DSC measurements such as scanning speed (heating rate), thermal resistance between holder and pan, sample weight, geometry, atmosphere, pressure, and sample correction. The effects of some of these were studied prior to running FFTF and INTEC fuel processing experiments. A brief description of factors effecting DSC data will be discussed and optimal operating parameters will be chosen.

5.1.1 Effect of Heating Rate

The correlation of peak height with heating rate has been studied by Garn (1961) and Melling et al (1969). It was determined by Garn (1961) that there is a correlation between heating rate and peak area if the temperature of the sample is subtracted from the temperature of the reference and plotted against the temperature of the sample. However, Melling et al., (1969) determined that if the peak area is measured as the temperature of the sample minus the temperature of the reference versus time, then peak area is independent of heating rate. Garn (1961) later determined that the area of the peak increased with heating rate due to a problem with heat transfer between his instrument and sample. Melling et al., (1969) did not have a heat transfer issue due to their instrument and the type of sample being used. There may not be a direct correlation between peak area and heating rate but it has been shown by Speil et al., (1945) that the peak amplitude is affected by heating rate. Figure 5.1 shows that as the heating rates are increased the amplitude of the peaks increase. The amplitude may change but this does not have an effect on the peak area because peak area is a function of time. The slower the heating rate is the smaller the amplitude of the peak. The area of the peak in Figure 5.1for the 5°C heating rate will yield the same (or nearly the same) peak area when compared to peak areas with faster heating rates.

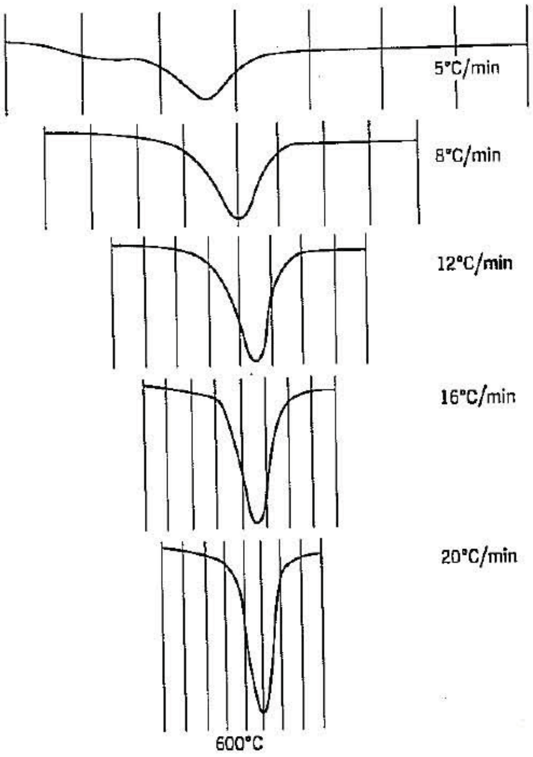

Figure 5.1: Variation of peak temperature with heating rate (Speil et al., 1945)

It was determined that peak area does not depend on heating rate but that peak amplitude was a function of heating rate. Work done by Pella and Nebuloni (1971) (Table 5.1) indicates that faster heating rates cause an increase in melting temperature of p-nitrotoluene by about 0.15°C between 0.5°/min and 2°/min. For phenanthrene, the melting temperature changes by 0.35°C between 0.5°/min and 2°/min. For the samples used in their study, the melting temperature increased as a function of heating rate; however, the change in temperature at which melting occurs is only measureable by highly sensitive equipment. The properties (density, conductivity, surface tension, etc.) of the sample as well as heating rate can affect the melting temperature.

Table 5.1: Influence of the scanning rate on the temperature (Pella and Nebuloni, 1971)

	Melting Temperature, °K		
Substance	0.5°/min	1°/min	2°/min
P-Nitrotoluene	319.60	319.70	319.75
Napthalene	350.25	350.50	350.60
Phenanthrene	371.30	371.55	371.75
Benzoic Acid	394.70	394.75	394.85
Anisic Acid	--	455.90	456.25

For this work, with ionic salts, a study of the effect of heating rates was done with the results shown in Figures 5.2 and 5.3. The curves in Figure 5.2 are for three heating rates: 20 K min^{-1} (purple), 10 K min^{-1} (blue) and 2 K min^{-1} (green) for a 9.2 mg potassium perchlorate standard in a sealed Au-SS crucible. The peak for each heating rate represents the melting of the sample. Figure 5.2 shows that the higher the heating rate the greater the DSC signal for the melting peak (faster heating rate, larger peak amplitude); the 20 K min^{-1} heating rate has a peak DSC signal near 2.5 μV/mg where as the peak DSC signal for 2 K min^{-1} is near 1.0 μV/mg.

The amplitude of the peak changes as a function of heating rate but the area remains nearly constant. The average peak area for the potassium perchlorate sample is 95.8 ± 1.2 μVs/mg, which translates to less than a 1.5% difference among peak areas for heating rates between 2 and 20 K min^{-1}. For this reason the peak area is not going to be considered a function of heating rate for this study. Table 5.2 is a summary of the data shown in Figure 5.2, where the onset temperature is, in this case, the melting temperature. These results confirm the lack of correlation between peak area and heating rate. The study also confirms the onset and peak temperatures are affected by heating rates (faster heating rate = higher onset and peak temperatures). For this study the effects of heating rates on the onset and peak temperatures are amplified because of the mass of the DSC crucibles used. Because the crucibles and samples need to be non-reactive and sealed due to the samples hygroscopic properties, heavier DSC crucibles were used compared to traditional alumina DSC crucibles. The Au-SS DSC crucibles create a small thermal lag that is more prevalent at high heating rates as opposed to lower heating rates.

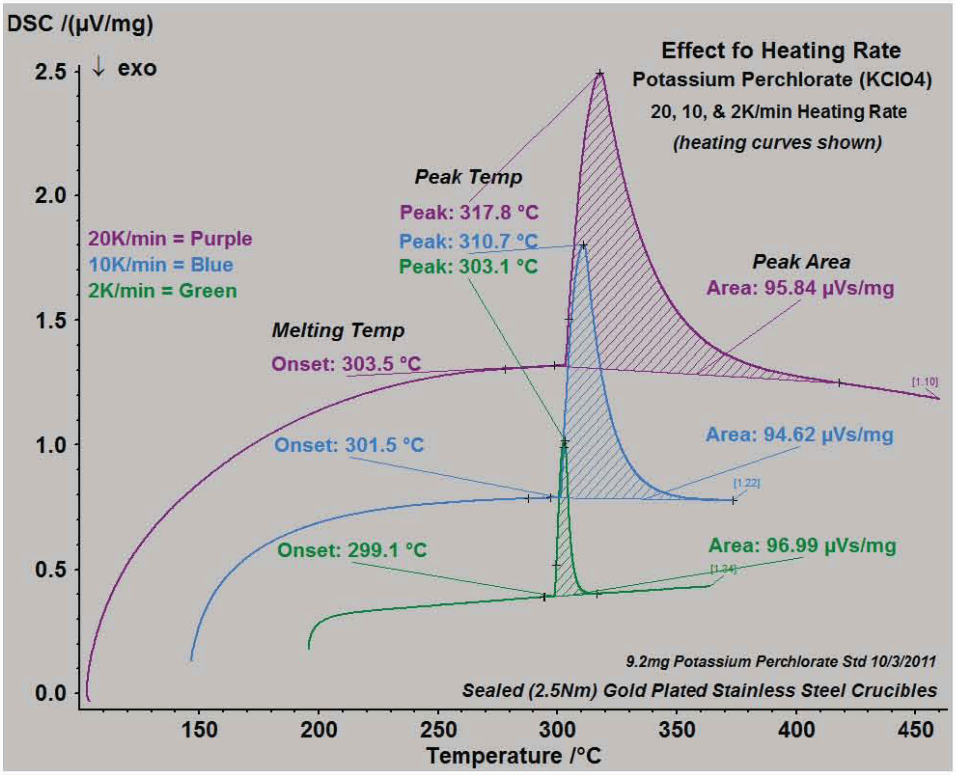

Figure 5.2: Effect of heating rate on transition temperatures and peak area

Table 5.2: Comparison of results from Figure 5.2

Heating Rate ($K\ min^{-1}$)	**Onset Temperature (°C)**	**Peak Temperature (°C)**	**Peak Area ($\mu Vs\ mg^{-1}$)**
20	303.5	317.8	95.84
10	301.5	310.7	94.62
2	299.1	303.1	96.99

Using higher heating rates allow for the detection of smaller transitions, some of which may not be detected at lower heating rates (Wendlandt, 1974) because higher heating rates cause the amplitude of the peaks to increase. Peak resolution is dependent on heating rate, the higher the heating rate the lower the resolution of DSC peaks. At a higher heating rate, 20 K min^{-1}, there may exist a large broad peak; however, if the heating rate is slowed to 2 K min^{-1}, then the broad peak may resolve into two peaks. Slowing the heating rate to resolve the peaks can have an effect on the peak height, and can possibly eliminate the peak altogether. Figure 5.3 shows how the height of the peaks (peak 1, 2) change with heating rate, peak 2 is not as prevalent at slower (2 K min^{-1}) heating rates compared to faster (20 K min^{-1}). Since there is such variability in the DSC signal with different heating rates, three heating rates will be used in this study, 20 K min^{-1}, 10 K min^{-1}, and 2 K min^{-1}, however, only two heating rates (10 K min^{-1} and 2 K min^{-1}) will be compared for this work. The conclusion for this study is that faster heating rates can increase the sensitivity of a DSC curve, as well as decrease the resolution and temperature accuracy.

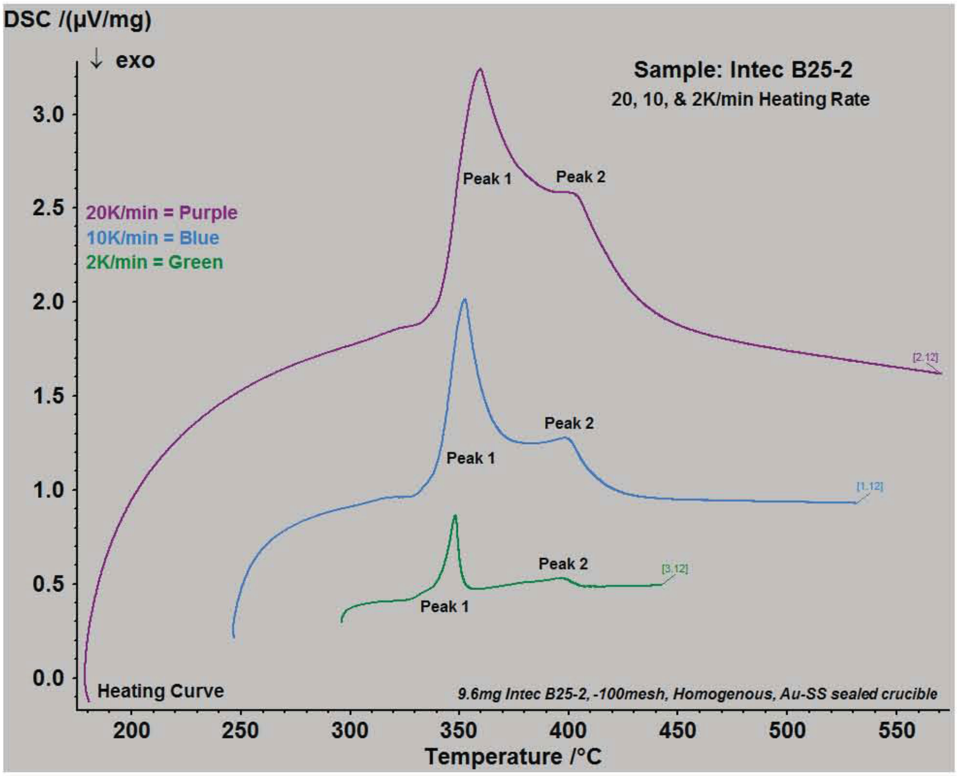

Figure 5.3: Effect of heating rate on peak resolution

5.1.2 Effect of Particle Size

It was concluded in a study by Grimshaw et al., (1945) that with particle sizes down to 1 micron, the thermal characteristics of kaolin samples were independent of particle size. The results of this study are shown in Table 5.3. For the kaolin study, a pure substance was used. Salt samples prepared for this work are a mixture of many salts. To ensure that the DSC samples were a homogenous mixture of the larger 15 g sample, samples were composed of particles smaller than 150 microns (100%, -100 Mesh) for DSC analysis. Small particle size will ensure that the DSC sample is a homogenous mixture that will yield reproducible results.

Table 5.3: Effect of Particle size on the thermal characteristics of Kaolin (Grimshaw et al., 1945)

Average Particle Size, µm	**Endothermic Reaction**		**Exothermic**
	Onset Temp., °C	**End Temp., °C**	**ΔT_{min}, °C**
10-44	600	670	980
0.5-1.0	605	650	980
0.25-0.5	605	630	980
0.10-0.25	600	615	980
<0.10	600	610	945, 990[e]

[e] Two peaks

5.1.3 Effect of Sample Mass

It is important when analyzing a sample consisting of multiple elements that the DSC sample is a good representation of the original sample. However the sample should be kept as small as possible so the DSC curves are not affected by the thermal lag due to sample size. To accurately compare DSC results between samples, the mass of the samples used for DSC analysis must be kept constant. An endothermic reaction such as sample melting will be effected by the mass of the sample. This is because the heat needed to cause the endothermic reaction is proportional to the mass of the sample (Pella and Nebuloni, 1971), meaning the more the sample weights the more heat will be needed to cause an endothermic reaction. If the sample size is too large, then DSC results will have a thermal lag due to the sample size. It is important to keep the sample small enough to reduce the effects of thermal lag but still have a sample that is a homogenous representation of the original. In a study done by Pella and Nebuloni (1971), the sample size was kept between 2 and 4 mg (using pure samples) and the results of that study are shown in Table 5.4. Table 5.4 shows that the melting temperature changes slightly with sample size.

Table 5.4: Influence of the sample mass on temperature (Pella and Nebuloni, 1971)

Substance	**Melting Temperature, (K)**			
	1mg	**2mg**	**3mg**	**4mg**
p-Nitrotoluene	319.87	320.08	320.29	320.52
Phenanthrene	370.25	370.97	371.22	371.39
Benzanilide	435.82	436.07	436.15	436.26

The degree to which the melting temperature will vary with respect to sample size is dependent on the sensitivity of the instrument and properties of the sample. There are advantages and disadvantages to having small and large sample sizes. Large samples are useful for detecting low-level transitions that might not be seen using smaller samples. Large sample size is good for non-homogenous samples and will show the effect of low concentrations on DSC curves (Wendlandt, 1974). Large sample sizes analyzed at faster heating rates will yield large board peaks (low resolution, low temperature accuracy), to reduce the broadness of the peaks it is necessary to run smaller samples at slower heating rates (this can become very time consuming). Small sample sizes yield highly resolved DSC curve peaks that are sharp. Smaller samples permit faster heating rates and take less time for DSC analysis (Wendlandt, 1974).

Before work for this project was done, several sample masses were used to determine the appropriate sample mass for this research. The effect of sample size can be seen in Figure 5.4, which shows the DSC curve for three sample sizes: 24.1 mg (purple), 10.1 mg (black) and 3.3 mg (blue) in a sealed Au-SS crucible at a heating rate of 2 K min^{-1}. In Figure 5.4, the peak areas range from 258.8 J/g to 254.2 J/g and the melting (onset) temperatures range from 353.5°C to 354.1°C for the three samples sizes used. There is no correlation between sample size and peak area or sample size and melting temperature. Figure 5.4 suggests that the sample properties, instrument or the instrument environment is not sensitive enough to show a correlation when samples range in size from 3 to 25mg. A sample size of 10 mg was chosen for DSC analysis in this study to ensure a homogenous, representative sample. With a 10 mg sample mass, the DSC curves yield sharp, resolved peaks and reproducible data.

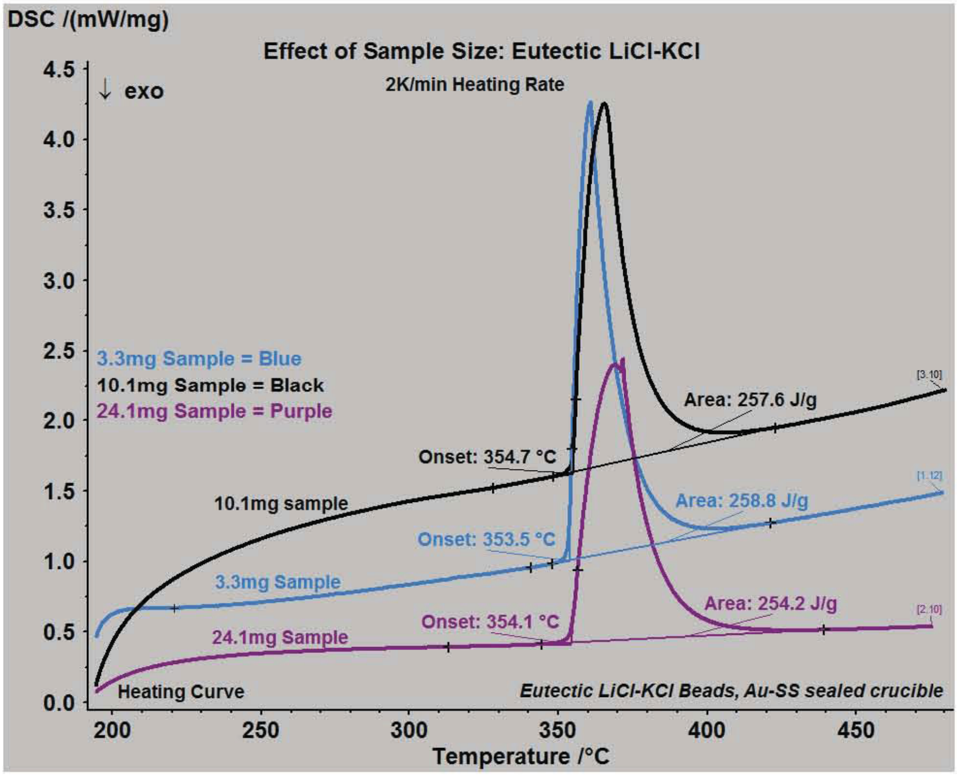

Figure 5.4: Effect of sample mass on temperature and peak area

5.1.4 Effect of Atmosphere

There are several options when selecting the purge gas for the DSC, including: air, nitrogen, argon, helium, etc. However it should be noted that different purge gases and purge gas flow rates will affect DSC results differently for identical sample with respect to melting temperature (Pella and Nebuloni, 1971) and baseline shape (Schindler, 2010). Furnace atmosphere affects the buoyancy of the sample holder. Buoyancy is caused by the gas flowing through the furnace; it causes the sample carrier to float in the furnace chamber. Argon has the most pronounced buoyancy effect compared to helium or air and can be seen in Figure 5.5 (Schindler, 2010). The buoyancy effect on the baseline is reduced with increasing temperatures, notice in Figure 5.5 that from 0 to 100°C the baseline is sloped, at temperature greater than 100°C the slope of the baseline becomes constant. A dynamic atmosphere should be chosen that will not react with the sample throughout the entire temperature range used during DSC analysis.

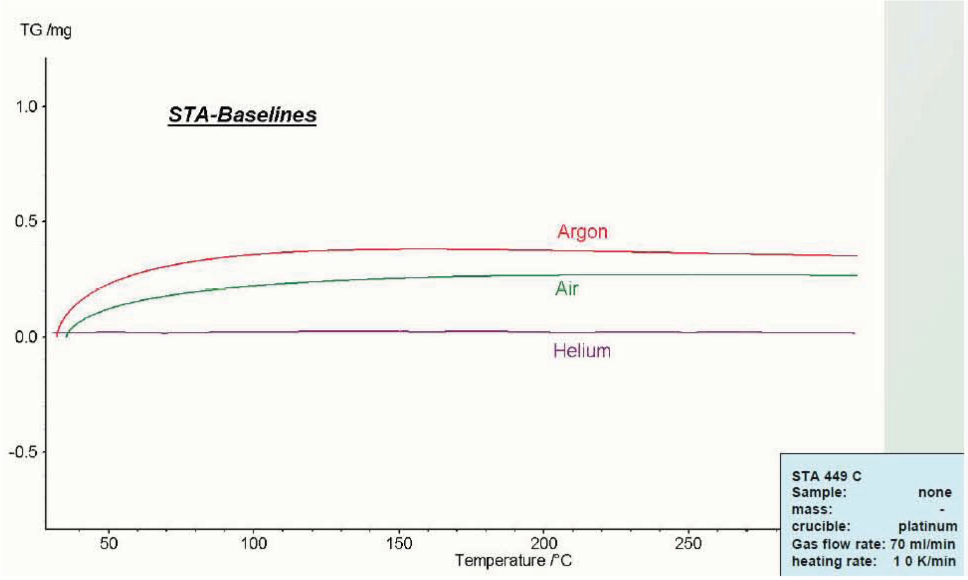

Figure 5.5: Effect of atmosphere on DSC curve (Schindler, 2010)

Pella and Nebuloni (1971) have shown that purge gas and its flow rate have an effect on the melting temperature of the sample; Table 5.5 shows these results. Comparing the indium standard with a purge gas flow rate of 75 cm^3 min^{-1} for nitrogen and helium a difference in melting temperature of over 5 K is seen. For this research, ±5 degrees is considered a significant difference. For indium with a nitrogen purge (0 to 75 cm^3 min^{-1}) the effects of the nitrogen on the melting temperature of the sample are minimal. For the same sample purged with helium the effects of purge gas at different flow rates is significant (>±5°C). Increasing the nitrogen gas flow rate of the tin sample actually yielded a melting temperature closer to the literature reported melting temperature of tin. This is because tin is easily oxidized. By increasing the nitrogen flow rate the sample has less interaction with oxygen and tin oxidation is reduced.

Table 5.5: Influence of purge gas on temperature measurements (Pella and Nebuloni, 1971)

	Melting Temperature, K							
	Nitrogen cm^3 min^{-1}				**Helium cm^3 min^{-1}**			
Substances	0	10	25	75	0	10	25	75
Indium MP = 429.76	429.1	429.5	429.7	429.7	429.1	435.7	435.5	435.2
Benzanilide MP = 436.36	437.6	436.4	436.5	436.5	437.6	443.7	443.2	442.9
Tin MP=505.06	508.9	504.8	505.0	505.3	508.9	515.1	514.9	514.6
Carbazole MP=518.46	520.9	517.7	517.7	517.9	520.9	528.7	529.1	529.6

For this study, there was only one viable option for purge gas, UHP argon. The salts are hygroscopic and have to be handled in moisture and atmosphere controlled glovebox. The oxygen and moisture concentrations in the glovebox are kept below 0.1 ppm. The sample is sealed in a Au-SS DSC crucible inside an argon atmosphere glovebox so the sample is only in contact with an argon environment. UHP argon purge gas is run through the DSC furnace chamber at a flow rate of 20 cm^3 min^{-1}. It should be noted that all the DSC curves in this study have a similar baseline to that shown in Figure 5.5, for the argon purge gas which is initially characterized with a rounded baseline that becomes flattened at higher temperatures.

5.2 Sample Homogeneity

To confirm the sample preparation technique, described in previous sections, results in a homogeneous mixture and the 10 mg DSC sample mass is representative of the 15 g simulated salt sample, three different samples of the salt INTEC B25 were run. First, a 10 mg sample was taken from the vial INTEC B25 sample, and termed INTEC B25-1. Next, the vial was covered with a lid and shaken for several minutes. The lid was removed from the vial and the contents were then stirred with a spatula for further mixing. Another 10 mg sample was taken from the vial and termed INTEC B25-2. This process was repeated yielding sample INTEC B25-3.

Figure 5.6 shows the DSC results of INTEC B25-1 (black curve), INTEC B25-2 (blue curve), and INTEC B25-3 (pink curve) for a heating rate of 10 K min^{-1}. Figure 5.6 indicates that there is very little difference between the onset, peak, and liquidus temperatures of the three INTEC B25 samples. It can be concluded that the 10 mg DSC sample is a homogenous representative sample of the 15 g simulated salt prepared using the procedure described above.

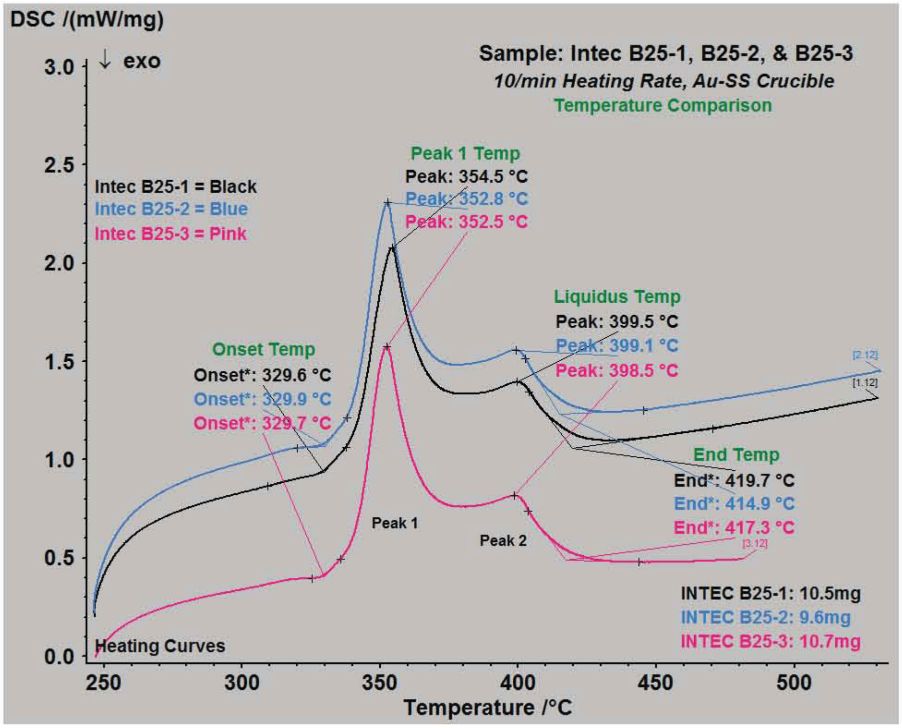

Figure 5.6: Temperature comparison of INTEC B25-1, INTEC B25-2, and INTEC B25-3 with a heating rate of 10 K min^{-1}

For the heating curves in Figure 5.6 a comparison of the three INTEC B25 samples is shown in Table 5.6 for 10K min^{-1} heating rate. The onset temperatures is 32.7 ±0.3°C, the peak temperatures is 353.3±1.2°C, the liquidus temperatures is 399.0±0.5°C, and end temperatures are 417.3±2.4°C, indicating that sample preparation procedures yield a homogenous sample and that the DSC is able to generate curves with reproducible results. This study also proves that taking a 10 mg subsample from the 15 g sample for DSC measurements will provide a representative sample and the DSC results will not change due to in-homogeneity of the sample.

Table 5.6: 10K min^{-1} heating rate comparisons of INTEC B25-1, INTEC B25-2, and INTEC B25-3 (Figure 5.6)

Sample	**Onset Temp (°C)**	**Peak (1) Temp (°C)**	**Liquidus Temp (°C)**	**End Temp (°C)**
INTEC B25-1	329.6	354.5	399.5	419.7
INTEC B25-2	329.9	352.8	399.1	414.9
INTEC B25-3	329.7	352.5	398.5	417.3
Average	329.7±0.3	353.3±1.2	399.0±0.5	417.3±2.4

5.3 Baseline Correction

INTEC B25-3 was run using a correction file. The correction also called baseline correction is when the DSC signal produced from the instrument (crucible, sample carrier, thermocouple, furnace etc.) is subtracted from the DSC signal of the sample. The correction file is run at the exact parameters (heating rate, temperature range, flow rate, isothermal time, calibration, etc.) that the sample will be run with. Two empty sealed Au-SS crucibles are loaded onto the sample carrier of the DSC. The DSC parameters are set and the correction file is acquired. Once the correction file is finished and saved, the crucible is loaded with ~10 mg of sample and then place back on the sample carrier. A new file is opened using a sample plus correction file. The DSC parameters of the sample plus correction have to be exactly the same as the conditions of the correction file. This will allow the software to subtract the corrected curve from the sample curve to produce a new curve that takes into account the contribution the thermal behavior of the measuring instrument itself.

The baseline correction should not change the transition temperatures but it will affect the slope of the baseline. This can be seen in Figure 5.7 and Figure 5.8 for heating rate of 10 K min^{-1} and cooling rate of 10 K min^{-1} respectively. In these Figures INTEC B25-1 (black line), INTEC B25-2 (blue line), and INTEC B25-3 (pink line) differ in DSC (ordinate) values. Notice that that INTEC B25-1 and INTEC B25-2 are not completely similar to each other even though both samples were run without a correction. There are several reasons for this: (1) the sample masses were different, (2) the crucible masses were different one possibly having slightly different thermal properties than the other, and (3) the location of each crucible relative to the reference crucible may have been slightly different, which can change the buoyancy properties of the sample carrier. Even thought the baseline is different for samples INTEC B25-1 and INTEC B25-2 they have very similar enthalpy of reaction values differing by only 1.9 J/g for the heating curve (Figure 5.7) and 2.6 J/g for the cooling curve (Figure 5.8).

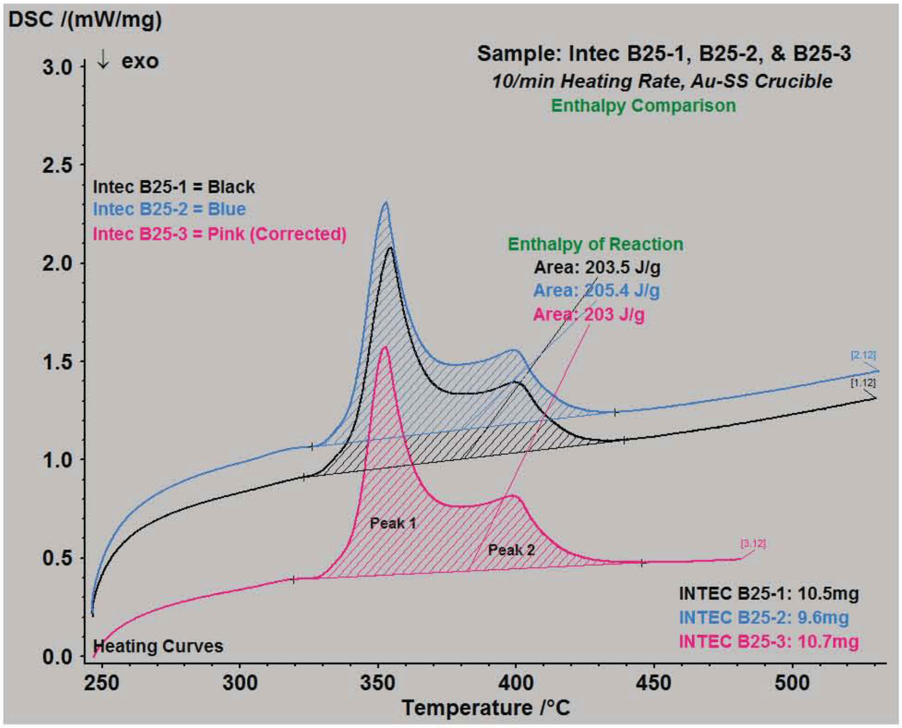

Figure 5.7: Comparison of corrected curves vs. non-corrected curve on the enthalpy determination of the heating curve

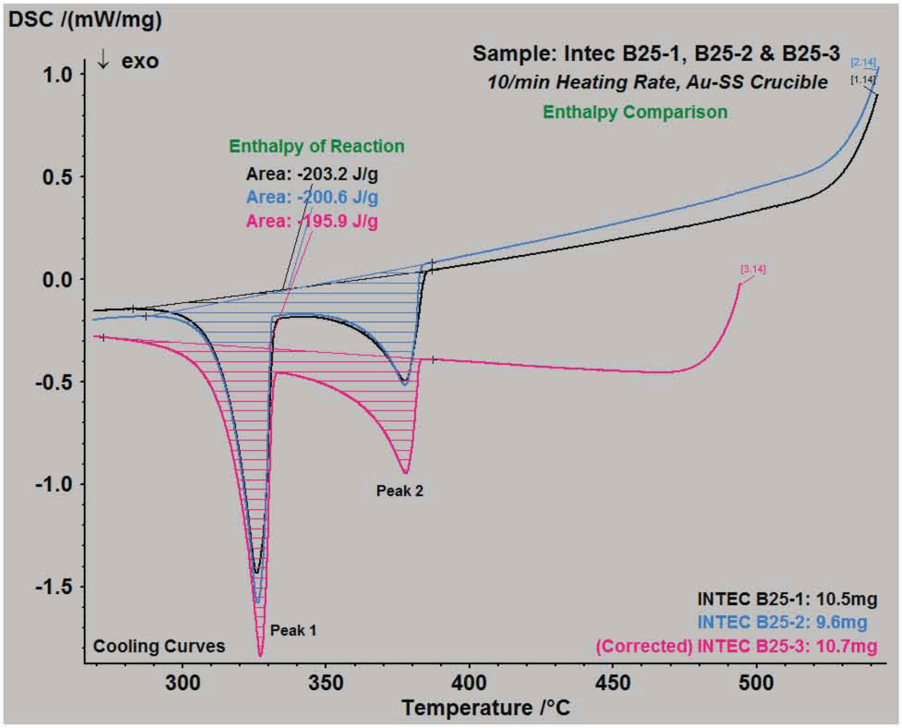

Figure 5.8: Comparison of corrected curves vs. non-corrected curve on the enthalpy determination of the cooling curve

The most important comparison to be seen in Figures 5.7 and 5.8 is between the non-corrected (INTEC B25-1, B25-2) and corrected (INTEC B25-3) DSC curves. The corrected curve differs in mW/mg (DSC signal) significantly from the non-corrected curve for both heating and cooling. However the enthalpy of reaction is still very similar to that of the non-corrected values. Table 5.7 lists the enthalpy values for each INTEC B25 curve. Because there is no significant variation in enthalpy due to the baseline correction it was determined that the effects of the instrument are minimal and need not be considered for future samples. The enthalpy values are also very similar when comparing heating (Figure 5.7) and cooling (Figure 5.8) curves. This suggests the reactions are reversible and reproducible.

Table 5.7: Comparison of heating and cooling curve enthalpy of reaction values; (-) exothermic

Sample	Enthalpy (Heating) J/g	Enthalpy (Cooling) J/g
INTEC B25-1	203.5	-203.2
INTEC B25-2	205.4	-200.6
INTEC B25-3	203.0	-195.9
Average	204.0±1.4	-199.9±7.5

5.4 LiCl-KCl Study

By studying the LiCl-KCl system, a better understanding of DSC curves with various heating and cooling rates and operating parameters was obtained. It also helped in interpreting properties of thermograms such as peaks, solidus, liquidus and peak areas. Eight LiCl-KCl salts, of varying composition, were prepared using high purity, anhydrous, LiCl and KCl. Table 5.8 shows the amount and compositions of LiCl and KCl used for each of the eight samples. The sample preparation described earlier was followed for the preparation of these samples as well, with the only significant difference being the sample size of ~2 g as opposed to 15 g. Equations 5.1 through 5.5 show the equations used for calculating mol of LiCl, mol of KCl, mol fraction LiCl, mol fraction KCl, and wt% LiCl of sample 3 in Table 5.8 (shaded gray). Similar calculations were performed for other samples in Table 5.8.

Table 5.8: Various compositions used in LiCl-KCl study

Sample	LiCl Added (g)	KCl Added (g)	Total LiCl-KCl (g)	LiCl (mol)	KCl (mol)	LiCl (mol fraction)	KCl (mol fraction)	LiCl (wt%)
1	0.0000	0.7500	0.7500	0.0000	0.0101	0.0	1.000	0
2	0.4242	2.9826	3.4068	0.0100	0.0400	.2000	.8000	12.5
3	0.3292	0.7502	1.0794	0.0078	0.0101	.4356	.5644	30.5
4[f]	--	--	--	--	--	.5920	.4080	44.0
5	0.8796	0.7502	1.6298	0.0207	0.0101	.6734	.3266	54.0
6	1.2714	0.5589	1.8303	0.0300	0.0075	.7999	.2001	69.5
7	1.4073	0.1999	1.6072	0.0332	0.0027	.9253	.0747	87.6
8	1.0000	0.0000	1.0000	0.0236	0.0000	1.000	0	100

[f] Sample 4 is the eutectic LiCl-KCl, this salt was not prepared like the other samples, it was purchased

$$\boldsymbol{mol\ LiCl} = 0.3292 g LiCl \times \frac{1\ mol\ LiCl}{42.394\ gLiCl} = 0.0078\ mol\ LiCl \quad (eq\ 5.1)$$

$$\boldsymbol{mol\ KCl}\ =\ 0.7502 g\ KCl\ \times \frac{1 mol\ KCl}{74.5513\ g\ KCl} = 0.0101\ mol\ KCl \quad (eq\ 5.2)$$

$$\boldsymbol{mol\ fraction\ LiCl} = \frac{0.0078\ mol\ LiCl}{0.0078\ mol\ LiCl\ +\ 0.0101\ mol\ KCl} = 0.4356\ mol\ LiCl \quad (eq\ 5.3)$$

$$\boldsymbol{mol\ fraction\ KCl} = \frac{0.0101\ mol\ KCl}{0.0101\ mol\ KCl + 0.0078\ mol\ LiCl} = 0.5644\ mol\ KCl \quad (eq\ 5.4)$$

$$\boldsymbol{wt\%\ LiCl} = \frac{0.3292 g\ LiCl}{0.3292 g\ LiCl\ +\ 0.7502 g\ KCl} \times 100\ =\ 30.5\ wt\%\ LiCl \quad (eq\ 5.5)$$

*****All calculations are for Sample 3***

Table 5.9 gives the average values of the eutectic and liquidus temperatures of the eight samples used in this study. Individual DSC curves from which these data were obtained and are presented in Appendix C. The values are an average of three different heating curves for heating rates of 10 K min^{-1} and 2 K min^{-1}. Single component salts (Sample 1 and Sample 8) do not have a eutectic; they have only a melting temperature. Two dashes (--) are used to denote when a temperature is not applicable to the sample. Notice in Table 5.9 that Sample 4 has the same eutectic and liquidus temperature; this is because Sample 4 is the eutectic composition of LiCl-KCl.

Table 5.9: Eutectic and Liquidus temperatures for LiCl-KCl study

Sample	LiCl, wt%	10 K min^{-1} Heating Rate		2 K min^{-1} Heating Rate	
		Eutectic Temp., °C	Liquidus Temp., °C	Eutectic Temp., °C	Liquidus Temp., °C
1	0	--	769.7	--	772.6
2	12.5	352.0	682.4	353.7	687.8
3	30.5	354.1	522.3	354.7	--
4	44.00	354.7	354.7	354.4	354.4
5	54.0	353.0	426.2	354.7	428.1
6	69.5	353.6	511.7	354.8	512.4
7	87.6	353.6	578.1	354.5	577.0
8	100.00	--	605.8	--	607.8

The LiCl-KCl phase diagram in Figure 5.9 was constructed using the experimental values (10 K min^{-1}) from Table 5.9 and other works: (Zemczuzny (1910); Richards and Meldrum (1917); Elchagardus (1932), as cited in Korin and Soifer 1997, Basin et al., 2008) it shows a comparison between the LiCl-KCl data from this work and data obtained from other LiCl-KCl studies. The blue cubic points (■) in Figure 5.9 are experimental results of this LiCl-KCl study. The data obtained in this research lies within ±5°C of other reported liquidus and eutectic temperatures.

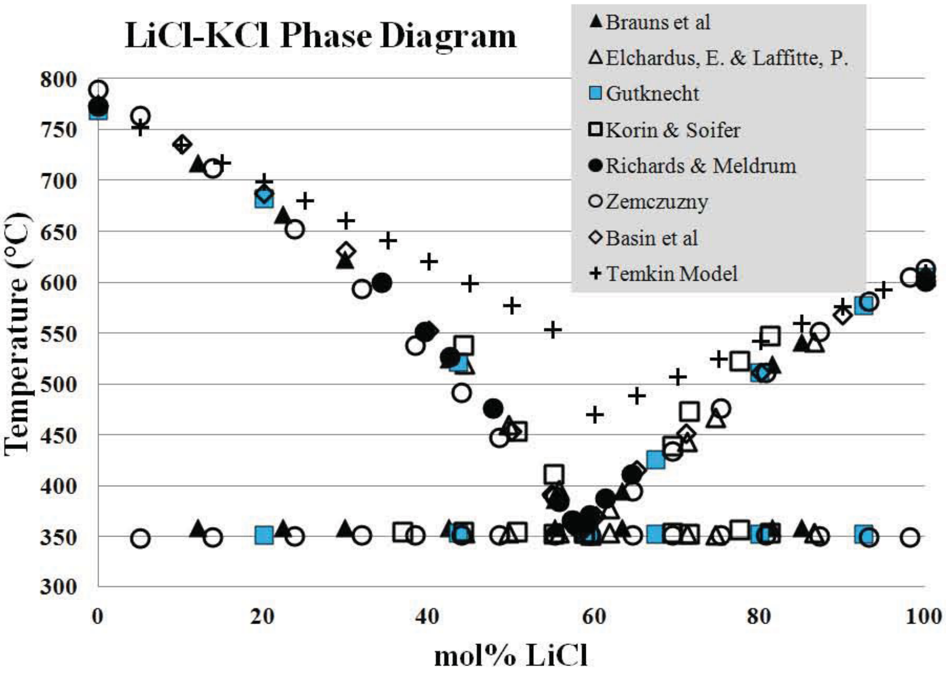

Figure 5.9: LiCl-KCl phase diagram comparison

The Temkin model was applied to the LiCl-KCl system and can be seen in Figure 5.9 represented by (+). Here, as expected, Temkin model does not accurately represent the liquidus line of the LiCl-KCl system for concentrations of LiCl between 20 and 75 mol%. It does however approximate, with good accuracy (±20°C) the liquidus temperature of the binary salt on the LiCl and KCl rich sides. Once the concentration of LiCl is greater than ~20 mol percent and the composition of KCl is greater than 20 mol percent the Temkin model is no longer valid for the binary system. Perhaps a corrected Temkin model accounting for deviations from ideal behavior would be a better fit for the data. For systems when no data are available the Temkin model can be applied to binary solutions (whose complexes are known) when the composition of each component is less than 20 mole percent. When the composition is greater than 20 mole percent the Temkin model data tends to deviate from ideal behavior. For the LiCl-KCl study the Temkin model was not needed because experimental results were generated and readily available for comparison (Zemczuzny (1910); Richards and Meldrum (1917); Schaefer (1920); Elchagardus (1932), as cited in Korin and Soifer 1997).

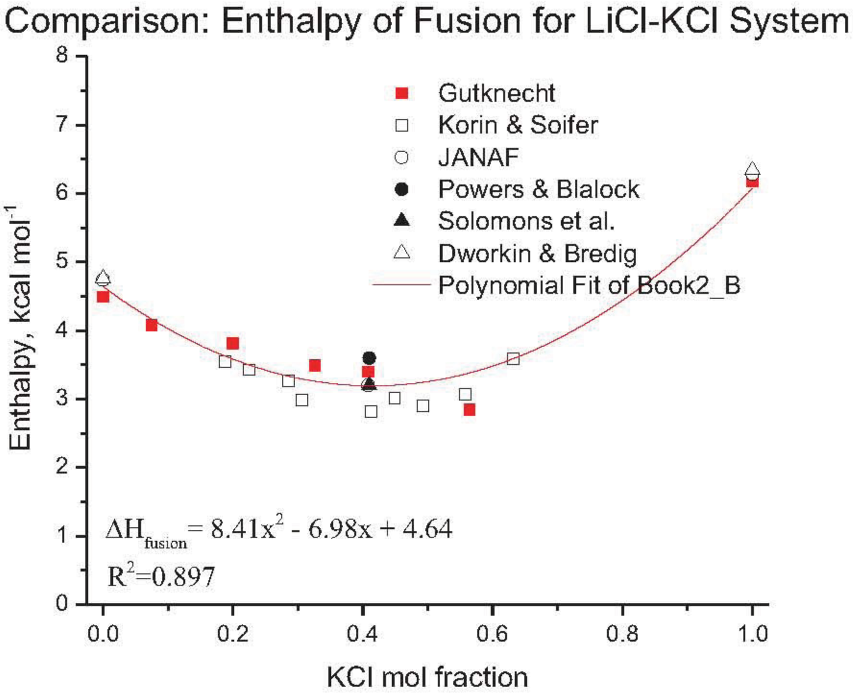

Figure 5.10: Enthalpy comparison of the common anion, binary alkali system, LiCl-KCl

The experimental DSC data collected in this study not only determine invariant reactions and liquidus temperatures, but it can (if calibrated correctly) yield a good approximation of the enthalpy of the system. Data generated for this study can be seen is shown in Figure 5.10 represented using a red box

(🟥) and is taken form DSC cooling curves with a cooling rate of 10K min^{-1}. This faster cooling rate proved to be more accurate than the slower cooling rate (2K min^{-1}) because of the increased sensitivity of the DSC at higher scanning rates. The cooling curve was used instead of the heating curve because the molten salt was in better contact with the surface of the DSC crucible allowing for more accurate enthalpy measurements. Enthalpy data was collected assuming atmospheric pressure. An equation for the enthalpy of fusion (H_{fus}) using a binary polynomial fit and is shown in Figure 5.10

5.5 Summary of Parameters chosen for this study

Table 5.10 lists the parameters used for all standards and experimental samples in this study.

Table 5.10: Standard DSC operating parameters

DSC Parameter	**Set Point**
Crucible Material	Gold plated stainless steel
Sealing Torque	2.5 N·m
Atmosphere	UHP argon
Sample Size	10mg ±1mg
Heating Rate(s)	10, 2 K min^{-1}

It should be noted that the crucibles were chosen for a few reasons:

1. Gold is not reactive with chloride salts
2. The crucible has the ability to be sealed so air (moisture) do not come in contact with the sample during DSC analysis causing unwanted reactions
3. The crucible exhibits good thermal conductivity and heat transfer properties

Since the sample was sealed in the crucible the internal pressure of the crucible may have increased slighty. The pressure does not increase to any significant extent based on the data from the LiCl-KCl study and was assumed to be atmospheric (1 atmosphere) for this study. All experimental samples were subject to a temperature profile (starting and ending temperature) that will try to be held a constant as possible. Since the samples that will be run on the DSC are unknown with respect to melting temperature the temperature profile will be adjusted accordingly.

6. RESULTS AND DISCUSSION

6.1 Spent Metallic Fuel Processing

From the DSC curves, the liquidus temperature can be determined along with (in most cases) the enthalpy of fusion. Enthalpy calculations are based on sensitivity calibrations that yield a sensitivity coefficient which is then used to determine enthalpy. Although this approach of enthalpy determination is not as accurate as specific heat calculations it yields a good approximation. The main purpose of this study was to determine the melting temperatures of the simulated molten salts. Also, estimation of other thermal properties such as enthalpy, entropy, and free energy, are discussed but are not available for every sample, due to the complexity of the salt mixture.

Programmed heating and cooling experiments were carried out at two heating rates. Each heating rate comprised of four temperature cycles. While, the first cycle (used to condition the sample in the Netzsch instrument) was omitted the other three cycles were used to collect the data. A DSC thermogram is useful in determining onset and peak temperatures. In the present study the final peak temperature was treated as the liquidus temperature because at this temperature in the measurement the entire sample became a homogenous melt. Each thermogram represents three heating cycles 10 K min^{-1} and 2 K min^{-1} respectively. All DSC thermograms are shown in Appendix D (FFTF Fuel) and Appendix E (INTEC Fuel). In the DSC thermograms black, blue and red color denotes/represents first, second and third heating/cooling cycles respectively. IN some instances it may be difficult to distinguish these lines as they lay directly on each other.

Each thermogram lists the onset temperature, final peak (liquidus) temperature, enthalpy of fusion, and recrystallization temperature. Also the heating and cooling curves the sample name, weight, and wt% of LiCl-KCl, actinide chlorides (UCl_3, $PuCl_3$), FP chlorides ($SrCl_2$, CsCl, $BaCl_2$, $LaCl_3$, $CeCl_3$, $PrCl_3$, $NdCl_3$, and $SmCl_3$) and NaCl are clearly labeled with proper legends.

Table 6.4 lists the onset temperature, liquidus temperature, enthalpy of fusion, and enthalpy of recrystallization (with the respective average values) for each DSC thermogram. The reported values were determined by averaging the results from the three cycles in each thermogram. In the text, the term DSC curve is used interchangeably with thermogram.

6.1.1 FFTF Fuel

It takes approximately 27 batches to process FFTF fuel inventory in the Mk-IV ER. Processes Each batch approximately processes 11.5 kg of heavy metal fuel (Yoo, 2011a). The composition used in the Mk-IV ER (before FFTF) is 76.8 wt% LiCl-KCl and 23.2 wt% impurity chlorides (Table 6.1). The electrolyte composition changes to 70.4 wt% LiCl-KCl and 29.6 wt% impurity chlorides after FFTF fuel is processed (Table 6.1). As the wt% of LiCl-KCl decreases, the wt% of impurity chlorides increases. Two 15 g simulated salt samples were made to represent the electrolyte composition in the Mk-IV ER: before and after the FFTF fuel were processed. Table 6.2 lists the electrolyte compositions used in the present investigation. $GdCl_3$ was used to mimic the chlorides of U and Pu. The actual wt% of each fission product has been provided in Appendix A. The amount of $PuCl_3$ present in the molten salt electrolyte was double the initial concentration while the FP chloride concentration increased by about 2.5 wt% after FFTF fuel was processed.

Table 6.1: Composition of Mk-IV salt Before and After FFTF fuel processing

	Mk-IV salt composition Before FFTF, (wt%)	**Mk-IV salt composition After FFTF, (wt%)**
LiCl-KCl	76.84	70.39
UCl_3	7.60	8.41
$PuCl_3$	1.42	3.68
NaCl	8.30	9.37
FP Chlorides	5.84	8.15

The DSC thermogram that compares the Mk-IV molten salt compositions (before and after FFTF fuel processing) with a heating/cooling rate of 10 K min^{-1} are shown in Figures 6.1 (heating) and 6.2 (cooling), respectively. A single pair of heating and cooling DSC curves are shown to make the thermograms less congested. Appendix D shows all the three heating and cooling cycles. The blue and black lines in Figure 6.1 represent the Mk-IV salt composition before and after FFTF fuel processingv respectively. Values listed in Table 6.2 were taken from these two figures.

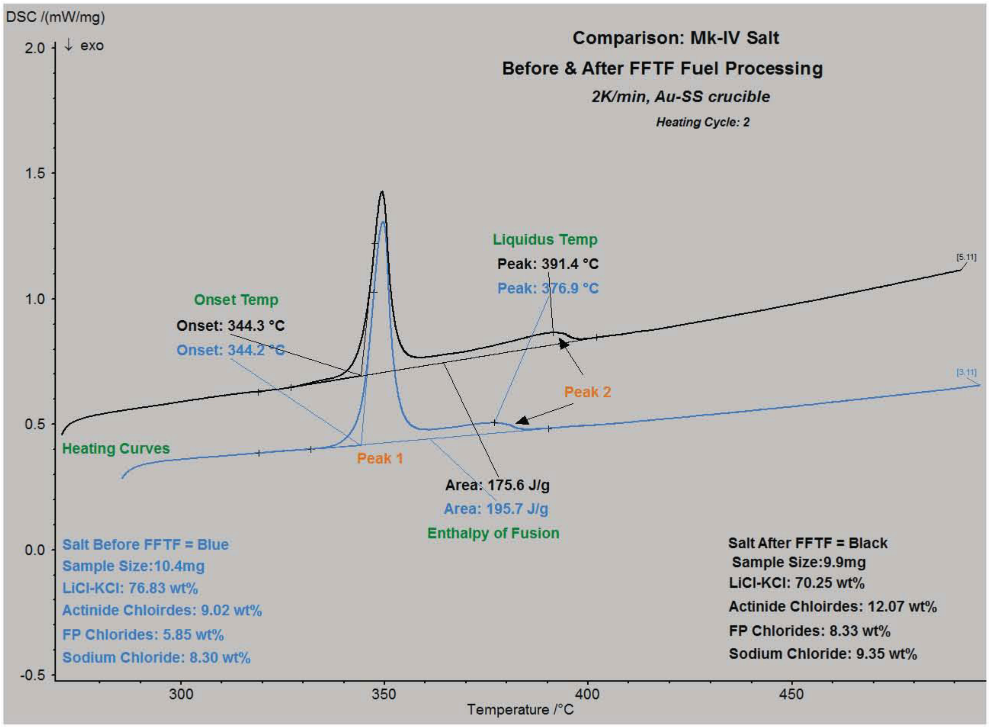

Figure 6.1: Comparison of DCS heating curves for Mk-IV salt Before and After FFTF fuel with a 10 K min^{-1} heating rate

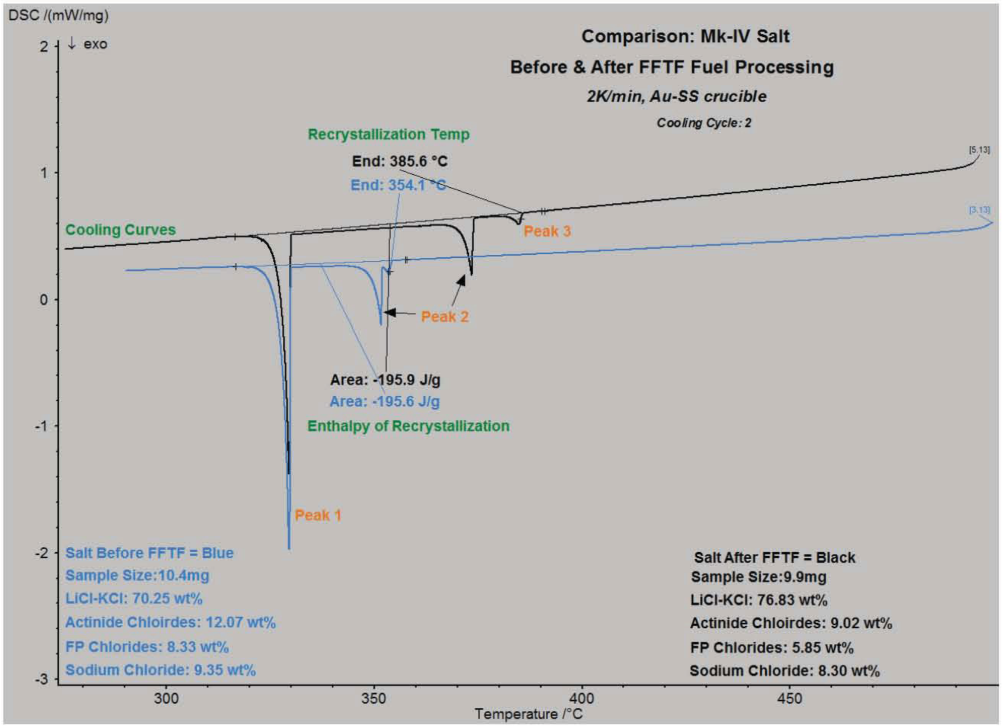

Figure 6.2: Comparison of DSC cooling curves for Mk-IV salt Before and After FFTF fuel with a 10 K min^{-1} heating rate

Although the cooling curve is shown for both samples, the temperature information is not used due to super cooling effects of the salt resulting in inaccurate onset and peak temperatures. When the transitions occurring on the heating curve are reversible, the enthalpy of fusion from the heating curves should equal the enthalpy of crystallization from the cooling curve. Sometimes, heating curves do not provide a clear distinction between transition peaks due to peak overlap. In general, cooling curves showed more resolved peak separation, which aided the determination of the peak temperature from the heating curve.

The heating curves, shown in Figure 6.1 clearly reveal two transition peaks. While the onset for Peak 1 occurred near 343°C for both before and after FFTF compositions, peak 2 appeared near 379°C for the sample labeled 'Before FFTF fuel' and at 392°C for the sample labeled 'After FFTF fuel'. Comparison of the heating and cooling curves in Figure 6.2 clearly shows that the salt goes through three transitions, labeled by 1, 2, and 3 during the cooling process. To resolve the peaks, a slower heating/cooling rate was used. Figure 6.3 shows that when the scanning (heating/cooling) rates were reduced, the peaks became more resolved and less sensitive to the transitions. Reduced sensitivity can be seen in Figure 6.3. Clearly the amplitude of peak 2 was larger at higher heating rates (10 K min^{-1}) . The presence of an extra peak during cooling might indicate the precipitation of a phase out of the salt (at a higher temperature) than that of the bulk salt upon recrystallization.

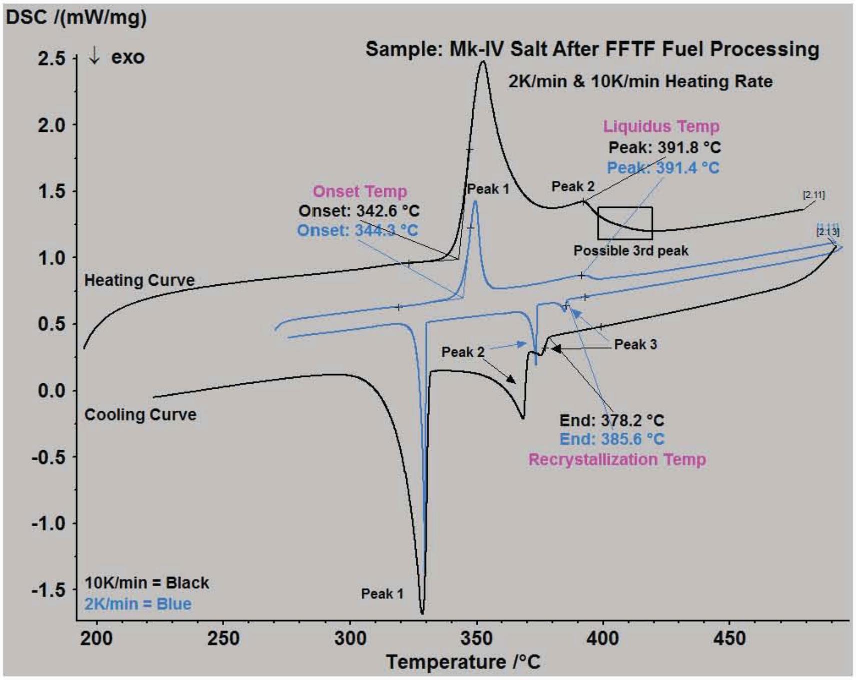

Figure 6.3: Effect of heating rates (10 K min^{-1} and 2 K min^{-1}) on Mk-IV salt After FFTF fuel processing

Peak 3 was small because of the temperature and mass of sample that was involved in the transition and was not visible on the heating curves. Onset and liquidus temperatures and estimated enthalpy of fusion values have been tabulated in Table 6.2 as well.

Table 6.2: Onset and liquidus temperature, and enthalpy of fusion Before and After FFTF fuel processing

		Before FFTF	**After FFTF**	**|Δ|**
Heating Curve	Onset Temp, °C	342.9	342.7	0.2
	Liquidus, °C	378.9	391.8	12.9
	Enthalpy of Fusion (J/g)	204.6	184.6	20.0
Cooling Curve	Peak 1, °C	325.2	328.4	3.2
	Peak 2, °C	349.0	368.3	19.3
	Peak 3, °C	352.1	375.0	22.9
	Enthalpy of Fusion (J/g)	-198.2	-184.5	13.7

Due to a higher impurity concentration (in the form of chlorides of Pu, Na, and FPs) in the After FFTF fuel sample, it was expected to have a higher liquidus temperature which was confirmed from the DSC pattern (Figure 6.1). The curve for after FFTF fuel indicates a liquidus temperature of 392°C while the DSC curve for the salt Before FFTF fuel processing showed a liquidus temperature of 379°C. Processing of more than 312 kg of heavy metal FFTF fuel, in the Mk-IV ER, would cause the liquidus temperature to increase by about 13°C.

6.1.2 INTEC Fuel

Seven simulated salt sample were made that represented the compositions of the Mk-IV ER salt at various points during INTEC fuel processing. The composition of each simulated salt sample is shown in Table 6.3. The samples are labeled in reference to the batch of INTEC fuel processed. For instance, INTEC B25 represented the composition of the Mk-IV ER salt after the 25th batch of INTEC fuel has been processed.

Table 6.3: Simulated salt for INTEC fuel samples

Sample	**LiCl-KCl, wt%**	**Actinide Chlorides, wt%**	**FP Chlorides, wt%**	**NaCl, wt%**
INTEC B25	66.2	12.5	10.1	11.2
INTEC B50	59.4	13.6	12.7	14.4
INTEC B75	54.8	12.3	15.3	17.6
INTEC B100	53.7	12.2	15.8	18.3
INTEC B125	48.3	13.3	17.8	20.7
INTEC B150	44.5	12.1	20.0	23.4
INTEC B165	44.9	13.1	19.4	22.6

It is hypothesized that the melting temperature of the molten salt with the impurity concentration built up would increase, Figure 6.4 proved this hypothesis to be true. Upon comparing of the DSC curves (of all INTEC simulates salt samples), it was clear that the liquidus temperature increased with an increase in impurity build-up. The impurities in this study are in the form of chloride of actinides, FP, and sodium. The DSC signal for each salt decreased in magnitude with increasing impurity concentration. This is shown by comparing Figures 6.4 (heating) and 6.5 (cooling). The scanning rate for all samples is 10 K min^{-1} with each curve shown on the same scale. The compositions of each salt, as well as sample size, shown in Figures 6.4 and 6.5, are listed in Table 6.4. The liquidus temperature represents the final peak temperature for each salt sample. Typically, the end of the final peak was taken as the onset temperature. This is because the crucibles used in the present study have a thermal lag atypical of alumina which is typically used as a crucible material for DSC measurements. After studying the LiCl-KCl system it was realized that the end peak temperatures represented the more accurate liquidus temperature.

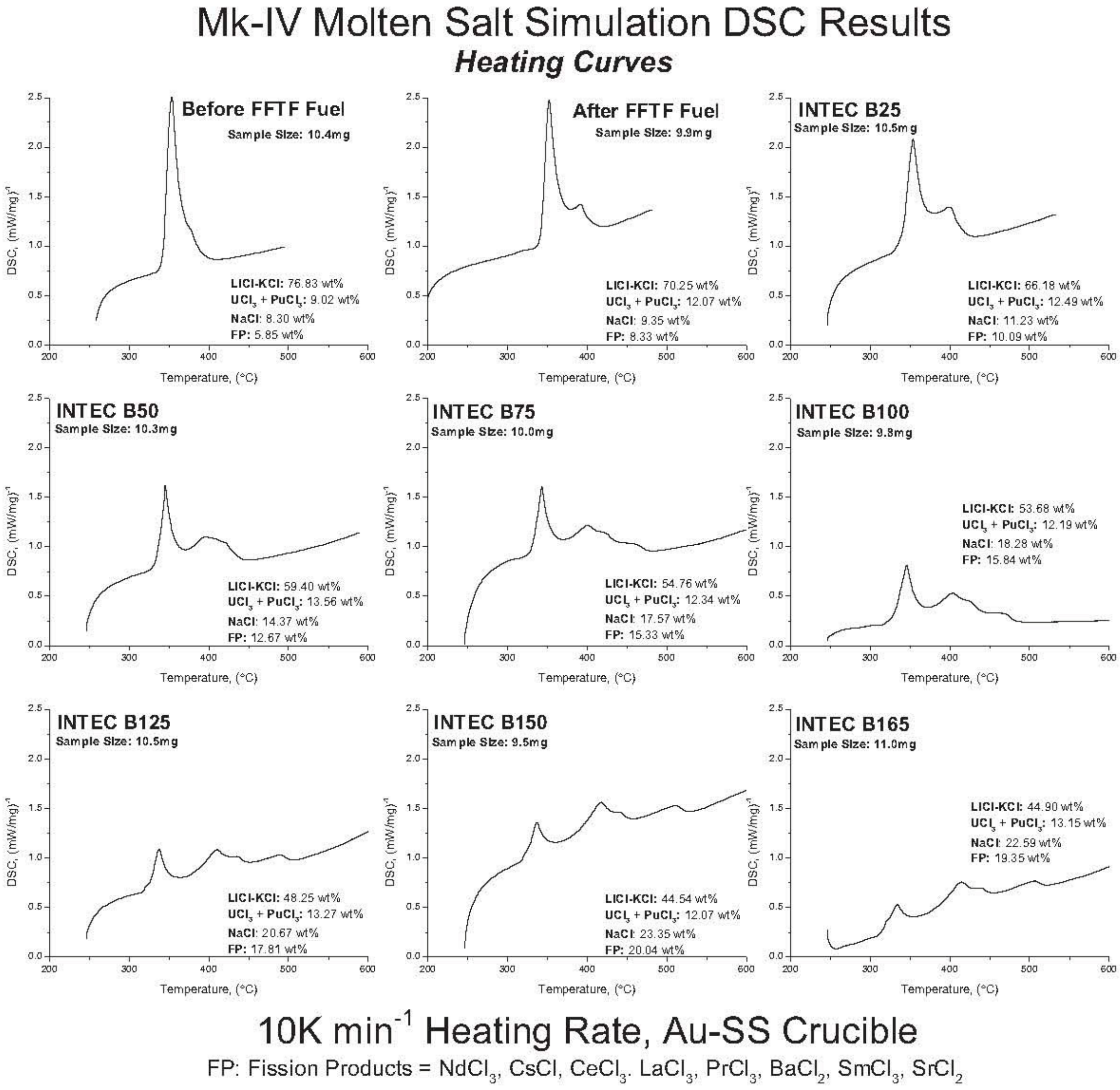

Figure 6.4: DSC thermograms of the simulated salt samples (used for processing of INTEC fuels), heating rate: 10 K min^{-1}. Each curve is shown on the same scale (for the sake of comparison)

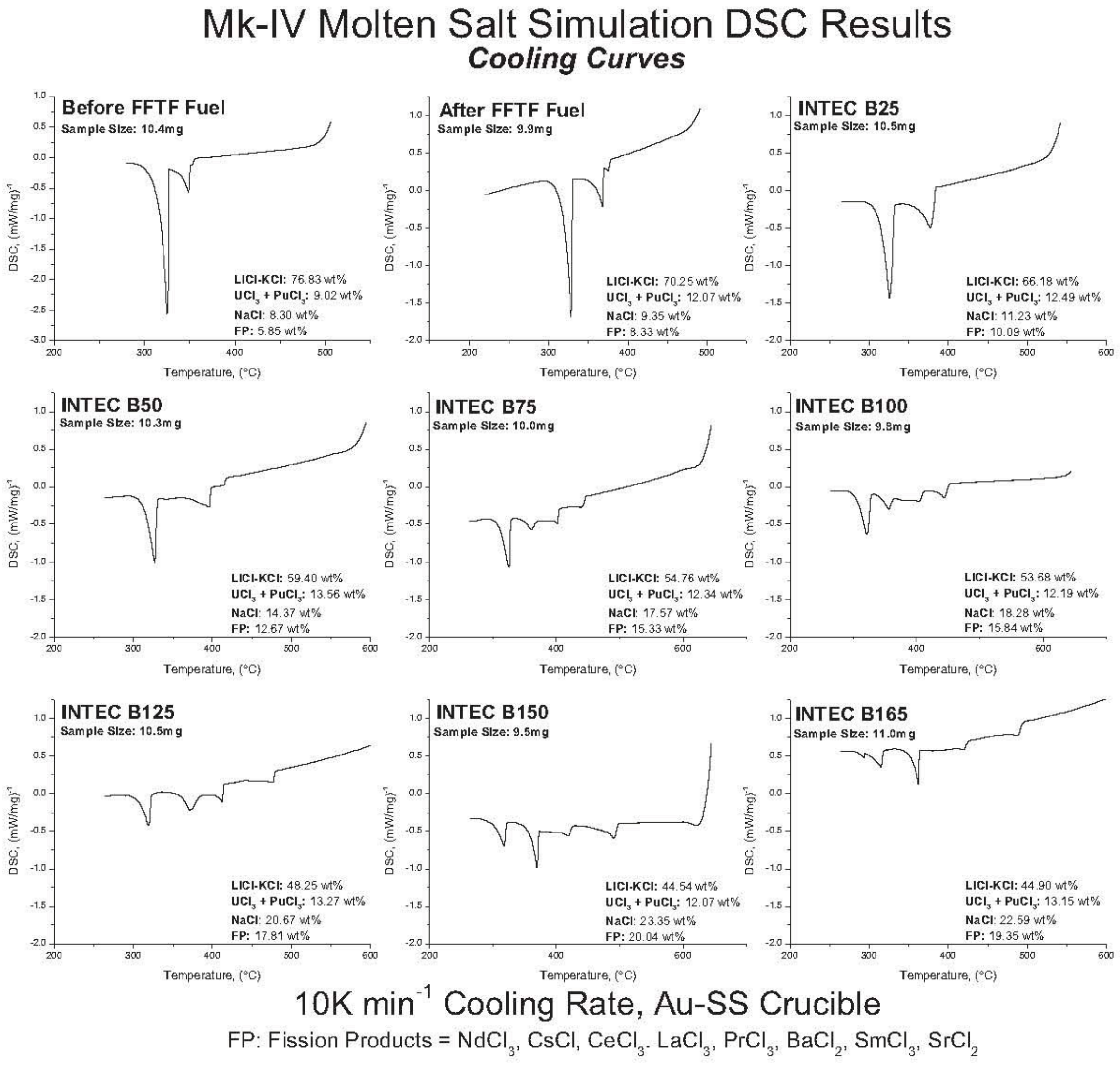

Figure 6.5: DSC results for INTEC fuel processing with a 10 K min^{-1} cooling rate

The onset and liquidus temperatures were observed to vary slightly with different heating rates. Table 6.4 has listed the onset and liquids temperatures, enthalpies of fusion and recrystallization for each simulated salt sample during INTEC fuel processing. The actual DSC curves from which the DSC data were tabulated (Table 6.4) have been presented in Appendix E. The thermograms in Appendix E have each of the three heating and cooling cycles labeled with the temperature and enthalpy values pertinent to each curve.

Table 6.4: Values taken from DSC curves for INTEC fuel processing

Sample	**Cycle**	**Onset (°C)**	**Liquidus (°C)**	**Enthalpy of Fusion (J/g)**	**Enthalpy of Crystallization (J/g)**
INTEC B25	1	340.2	399.2	203.4	-202.4
	2	340.6	399.5	200.6	-203.6
	3	340.3	399.8	201.9	-203.7
	Average	340.4	399.5	202.0	-203.2
INTEC B50	1	332	419.8	173.6	-168.4
	2	332.4	420.7	170.0	-166.6
	3	332.6	420.5	164.0	-165.5
	Average	332.3	420.3	169.2	-166.8
INTEC B75	1	330.7	477.5	168.9	-175.9
	2	328.6	461.7	176.3	-177.3
	3	330.7	461.6	175.2	-174.4
	Average	330.0	466.9	173.5	-175.9
INTEC B100	1	318.2	469.5	193.3	-182.7
	2	316.6	469.9	188.9	-179.8
	3	316.5	470.4	186.5	-177.6
	Average	317.1	469.9	189.6	-180.0
INTEC B125	1	317.6	491.4	134.2	-170.6
	2	317.5	490.2	137.3	-175.9
	3	317.3	490.1	142.0	-172.3
	Average	317.5	490.6	137.8	-172.9
INTEC B150	1	318.2	511.6	198.3	-199.6
	2	317.7	511.1	192.9	-177
	3	317.4	510.6	190.8	-185.6
	Average	317.8	511.1	194.0	-187.4
INTEC B165	1	313.0	507.6	152.8	-213.2
	2	313.0	506.8	152.5	-210.2
	3	316.5	506.5	155.8	-209.4
	Average	314.2	507.0	153.7	-210.9

The onset temperature of eutectic LiCl-KCl salt is ~352°C. The addition of over 23 wt% impurities decreased the onset temperature to 340±2°C. The onset temperature remained constant at ~340°C until after INTEC B25 was processed or the impurity concentration became greater than 33wt%. INTEC B50 and INTEC B75 had similar onset temperatures (near 330°C) because they had total impurity concentration of 43±3 wt%. Impurity concentrations between 46 and 55 wt% (INTEC B100, INTEC B125, INTEC B150, and INTEC B165) had an onset temperature near 317°C. The reason for the reduced onset temperature, after processing batch 100 of INTEC fuel, was caused by a small peak (transition) occurring before the bulk of the material went through a series of transitions. This small peak was embedded in the larger peak and could be faintly seen in samples INTEC B100 through

INTEC B165. To determine the nature of the transition(s) associated with each peak, other complimentary characterization techniques (such as X-Ray diffraction) are necessary.

The number of transition peaks present in the salt also changes with increasing impurity concentration. It can be seen that at a heating rate of 10 K min^{-1} for, INTEC B25 and INTEC B165 shows two and five peaks, respectively. Unlike the case of pure binary or ternary salts (eutectic LiCl-KCl and KCl-LiCl-NaCl, respectively) higher impurity concentrations in these salts can give rise to the presence of multiple peaks. These peaks signify simple crystallographic phase changes and/or formation of either congruent or incongruent melting phases.

6.1.3 Discussion

At the beginning of FFTF fuel processing, the Mk-IV ER salt had a melting temperature of 378°C with an impurity concentration of 23wt%. Upon the completion of 192 batches of spent metallic fuel (both FFTF and INTEC) the melting temperature of the electrolyte had risen to 512°C with an impurity concentration near 60 wt%. The Mk-IV operates at 500°C for current electrorefining operations. To maintain a homogenous melt, the Mk-IV ER should operate with a superheat of 100°C. Superheat being defined as the operating temperature minus the melting temperature of salt. The superheat line is shown as a red line (occurring at 400°C) in Figure 6.6. To ensure safe operating conditions in the Mk-IV ER, it is recommended that once the salt has less than 100°C superheat ideas need to be considered to lowering the melting temperature of the salt. Figure 6.6 suggests that any spent fuel processed after INTEC B25 would result in less than 100°C superheat. At this point the salt impurity concentration is nearly 35 wt%. Some salt may need to be removed from the Mk-IV ER and eutectic LiCl-KCl salt must be added to decrease the melting temperature and maintain ~500 kg of electrolyte in the ER vessel. The melting temperature can also be reduced by "cleaning" the salt

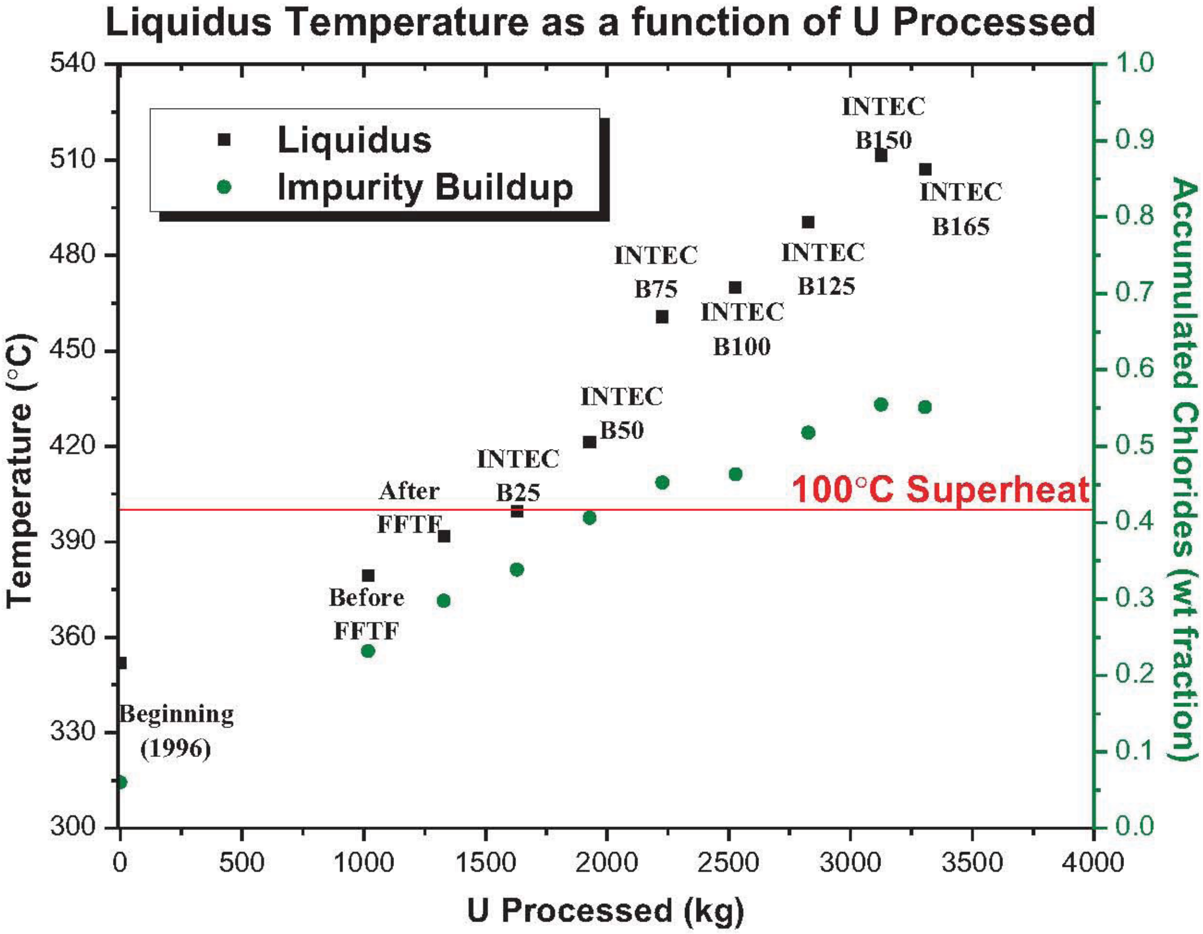

Figure 6.6: Liquidus and onset temperature as a function of impurity concentration in simulated salt sample

It is possible to get an estimate of the melting temperature of the Mk-IV ER, electrolyte within a range of ±35°C, simply by taking into consideration the NaCl concentration and ignoring the presence of the rest of the elements ($SrCl_2$, CsCl, $BaCl_2$, $LaCl_3$, $CeCl_3$, $PrCl_3$, $NdCl_3$, $SmCl_3$, and $GdCl_3$) that make up each salt sample. A comparison of the liquidus temperatures of modeled and experimentally obtained values is shown in Figure 6.7. The modeled values were obtained from the liquidus projection of KCl-LiCl-NaCl (Figure 3.14) by Sangster and Pelton (1991). The approximate liquidus temperature modeled by Sangster and Pelton (1991) is represented in Figure 6.7 by black squares (■). This data was extracted from a ternary liquidus projection for KCl-LiCl-NaCl.

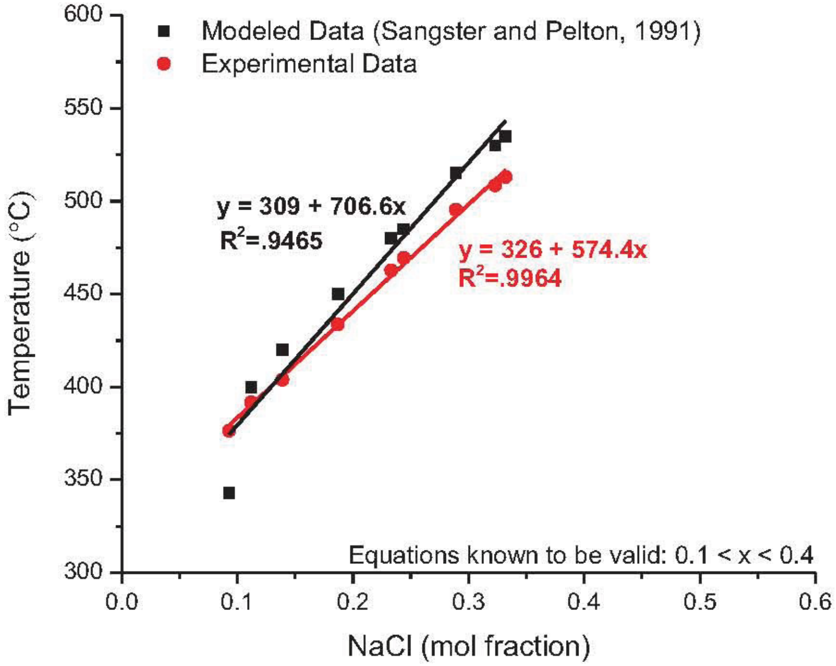

Figure 6.7: Modeled (Sangster and Pelton, 1991) vs. experimentally determined liquidus temperature

The ratio of KCl to LiCl remains constant for all data points representing the eutectic composition of 0.592 mol LiCl and 0.407 mol KCl. If the data were plotted on a ternary phase diagram (Figure 3.14) it would depict the mol fraction of NaCl linearly increasing along the eutectic LiCl-KCl composition line. The red dots (●) in Figure 6.7 represent the melting temperature of the surrogate salts, used to represent the Mk-IV electrolyte. There is a range of validity for the equations shown in Figure 6.7. The equations hold in the good composition range of 0.1 to 0.4 mol fraction. Below 0.1 mol fraction NaCl, the eutectic temperature for the modeled data changes the slope of the line. A linear function does not provide the best fit prior to 0.1 mol fraction NaCl and can be seen by the R^2 value of 0.9465. The experimental data can be represented very adequately with the linear fit function, resulting in a R^2 value of 0.9964. Once the NaCl composition in the salt is greater than 0.1 mol fraction NaCl the data can be fit linearly. Table 6.5 shows the recalculated salt composition, that considers only the three compounds listed above. Table 6.5 also compares the melting temperature of the simulated salt samples with the corresponding estimated values for the melting temperature of KCl-LiCl-NaCl based on the liquidus projection, developed by Sangster and Pelton (1991).

Table 6.5: Comparison of experimental and modeled liquidus temperatures, (modeled liquidus temperature were obtained from the KCl-LiCl-NaCl phase diagram, Sangster and Pelton (1991))

Sample	**KCl (mol fraction)**	**LiCl (mol fraction)**	**NaCl (mol fraction)**	**Experimental Melting Temperature (°C)**	**Liquidus Projection Melting Temperature (°C)**	**Projected - Experimental (°C)**
Before FFTF	0.369	0.538	0.093	376.4	343	-33.4
After FFTF	0.361	0.527	0.112	391.7	405	13.3
INTEC B25	0.351	0.510	0.139	403.9	420	16.1
INTEC B50	0.331	0.482	0.187	433.7	450	16.3
INTEC B75	0.312	0.454	0.233	462.7	480	17.3
INTEC B100	0.308	0.448	0.244	469.4	485	15.6
INTEC B125	0.290	0.421	0.289	495.3	515	19.7
INTEC B150	0.272	0.395	0.332	513.0	535	22.0
INTEC B165	0.276	0.401	0.323	508.5	530	21.5

Several reasons can be cited for the difference between the experimental obtained and estimated melting temperatures. The ternary has not taking into account the effects of other sample constituents ($SrCl_2$, CsCl, $BaCl_2$, $LaCl_3$, $CeCl_3$, $PrCl_3$, $NdCl_3$, $SmCl_3$, and $GdCl_3$). The effects of these elements and their concentrations have not been represented. The complex formation is more common with bivalent and trivalent species such as alkaline and rare earth chlorides. It is well known that the multivalent complexes that formed with these elements would alter the modeled (KCl-LiCl-NaCl) melting temperature to a significant extent. Deviations from modeled behavior due to the complex formations are the basis of the Temkin model. In order to use the Temkin model, all complexes must be known so that the activity of the complexes can be estimated for arriving at the solution in the composition range where the complexes exists. The Temkin model is not used for ternary species and as a result very little insight to the system of current of interest. Nonetheless, it can predict the melting temperature of the binary systems (axis of ternary phase diagram) when the concentration of each species is less than approximately 0.30 mol fraction. The usefulness of the Temkin model is shown in Figure 6.8. Here, the Temkin model calculates the KCl (red line) and NaCl (blue line) liquidus temperature using the ideal activity of KCl and NaCl, respectively. For concentrations of KCl and NaCl <~0.30 mol fraction, the Temkin model provides a very good approximation of the melting temperatures. A modified Temkin model can predict the melting temperature of the ionic binary solution at all concentrations.

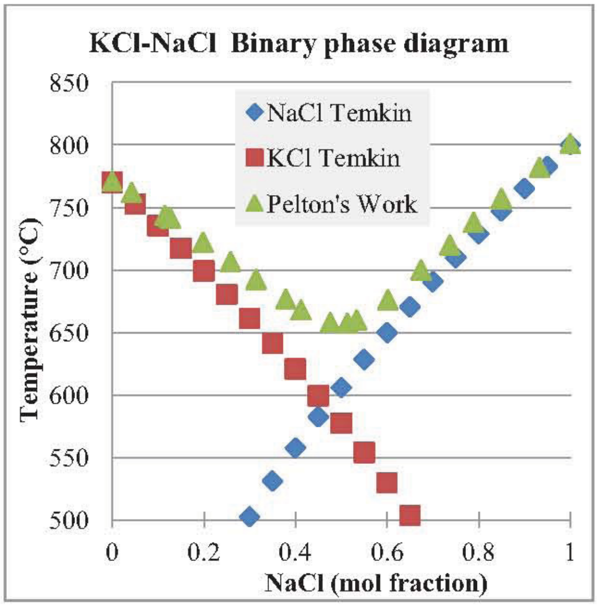

Figure 6.8: KCl-NaCl liquidus projection on the basis of the Temkin model

According to Sangster and Pelton (1991) another reason for the observed deviations of the melting temperature from the experimental and the modeled liquidus temperature is the effect of the ionic radii of the rare earth chlorides. They modeled the monovalent alkali chloride ternary metal systems using the conformal ionic solution theory. The theory concludes that the excess free energy of mixing of an ionic mixture can be represented by a simple polynomial that only takes into account nearest neighbor interactions (Blander, 2000). Typically, a one or two term polynomial will yield a close approximation (Sangster and Pelton, 1987) and the closer the ionic radii are in size the more accurate the approximations can be. For K, Li and Na, the atomic radii are between 0.073 and 0.151 nm, with Li and K having the smallest and largest ionic radii, respectively. The rare earth elements, used in this study, were having the ionic radii in the range of 0.117nm (La^{3+}) – 0.107nm (Gd^{+3}). The difference between the ionic radii of the alkali metals and the rare earth will have an effect on the interaction energy between the nearest neighbor atoms. This, in turn, will affect the Gibb's free energy of mixing, as well as enthalpy and entropy of the mixing, leading to a liquidus temperature that can have both positive and/or negative deviation from the ideal model (in this case KCl-LiCl-NaCl).

The experimental data, modeled in (Figure 6.7), assumed the presence of only three chloride species in the solution (KCl, LiCl, and NaCl) and the rest of the elements, mainly rare earth chlorides were not considered.

Another way to compare the modeled data with the experimental date is to assume the NaCl concentration, used in the experimental samples to represent other metal chlorides except LiCl and KCl. This means that NaCl represents $SrCl_2$, CsCl, $BaCl_2$, $LaCl_3$, $CeCl_3$, $PrCl_3$, $NdCl_3$, $SmCl_3$, $GdCl_3$, and of course NaCl. This assumption can be made because the ionic radii of Na, Sr, Cs, Ba, La, Ce, Pr, Nd, Sm, and Gd is approximately 0.110 ± 0.007 nm. As per the model, developed by Sangster and Pelton (1987, 1991). The nearest neighbor interactions are assumed to be approximately the same distance apart. NaCl was used to represent the mixture of complexes in the experimental samples because the ionic radii of the sodium and other elements are similar. Modeled (approximate liquidus temperature) data were extracted from the ternary liquidus projection, modeled by Sangster and Pelton (1991). The approximate liquidus temperature (NaCl concentration is equal to the sum of all species in solution except LiCl and KCl), experimental liquidus temperature, representative NaCl concentration, concentrations of LiCl, KCl, and other metal chlorides for each of the simulated salt sample are listed in Table 6.6.

Table 6.6: Composition and liquidus temperature of modeled and simulated salt samples

Sample	**KCl (mol fraction)**	**LiCl (mol fraction)**	**Representative NaCl (mol fraction)**	**Other Metal Chlorides (mol fraction)**	**Modeled Liquidus Temperature (°C)**	**Experimental Liquidus Temperature (°C)**
Before FFTF	0.3550	0.5173	0.1278	0.038	400	376.4
After FFTF	0.3406	0.4982	0.1612	0.055	425	391.7
INTEC B25	0.3298	0.4784	0.1938	0.067	450	403.9
INTEC B50	0.3066	0.4459	0.2502	0.077	495	433.7
INTEC B75	0.2871	0.4174	0.2989	0.084	520	462.7
INTEC B100	0.2825	0.4106	0.3104	0.086	525	469.4
INTEC B125	0.2623	0.3811	0.3607	0.099	555	495.3
INTEC B150	0.2450	0.3559	0.4038	0.105	575	513.0
INTEC B165	0.2480	0.3601	0.3965	0.106	575	508.5

The data in Table 6.6 was used to generate the curves, seen in Figure 6.9, which essentially is a plot of the liquidus temperature vs. the NaCl concentration. The modeled liquidus temperature data are being represented by black squares (■) where the liquidus temperature is based on the representative composition of NaCl present in the KCl-LiCl-NaCl system. Representative composition of NaCl is equal to the concentration of all constituents in the salt sample except LiCl and KCl. The KCl-LiCl concentration remained at the eutectic ratio for all data points. The experimental liquidus temperature data points were taken from DSC curves presented in Appendices D and E. The data used in Table 6.6 were taken from the DSC curves generated with a scanning rate of 2 K min^{-1}. Figure 6.9 shows that the modeled and experimental liquidus temperatures are quite different. At higher concentrations of NaCl, the liquidus temperature varies by more than 60°C. By introducing a correction factor to the modeled data, it may be possible to account for the interactions from salt constituents other than KCl, LiCl, and NaCl. A linear fit was applied to the modeled data and the experimental data that yielded the following two equations:

$$Modeled\ Data: \qquad y = 325 + 636x \qquad eq\ 6.1$$

$$Experimental\ Data: \qquad y = 308 + 506.6x \qquad eq\ 6.2$$

where x is the representative mol fraction of NaCl in the samples, it's value is given in Table 6.6 for all samples. A correction factor, (β) that needs to be applied to the modeled data will account for the actual NaCl concentration in the salt, can be expressed as:

$$\beta = (Modeled\ Liquidus\ Temperature) * (Other\ Metal\ Chlorides\ mol\ fraction) \qquad eq\ 6.3$$

The modeled data is based on the simple ternary system KCl-LiCl-NaCl that has been studied by many authors. The experimental data is based on a complex system, composed of KCl, LiCl, NaCl, $SrCl_2$, CsCl, $BaCl_2$, $LaCl_3$, $CeCl_3$, $PrCl_3$, $NdCl_3$, $SmCl_3$, and $GdCl_3$. The introduction of β to the modeled data is expected to take care of the effect of the change in liquidus temperature due to more complex species, arising out of a combination of $SrCl_2$, CsCl, $BaCl_2$, $LaCl_3$, $CeCl_3$, $PrCl_3$, $NdCl_3$, $SmCl_3$, and $GdCl_3$ for which no modeling information exists in open literature. The correction factor allowed a known simple monvalent ternary system to represent an unknown system that contains multiple species, not studied yet. The corrected data are represented by half filled black circles in Figure 6.9. The corrected model yields the following linear equation

$$Corrected\ Model: \qquad y = 325 + 636x - \beta \qquad eq\ 6.4$$

A simple check for the equation of this line shows that the assumptions made for corrected model are reasonable. When x = 0 in equation 6.4 the liquidus temperature is equal to 328°C. This would be the eutectic composition for KCl-LiCl, which has a melting point of 352°C. The corrected model is off by 25°C. When x = 1 in equation 6.4, the liquidus temperature is equal to 803.3°C. This would be the composition of pure NaCl which has a melting temperature of 801°C. The corrected model is off by less than 3°C.

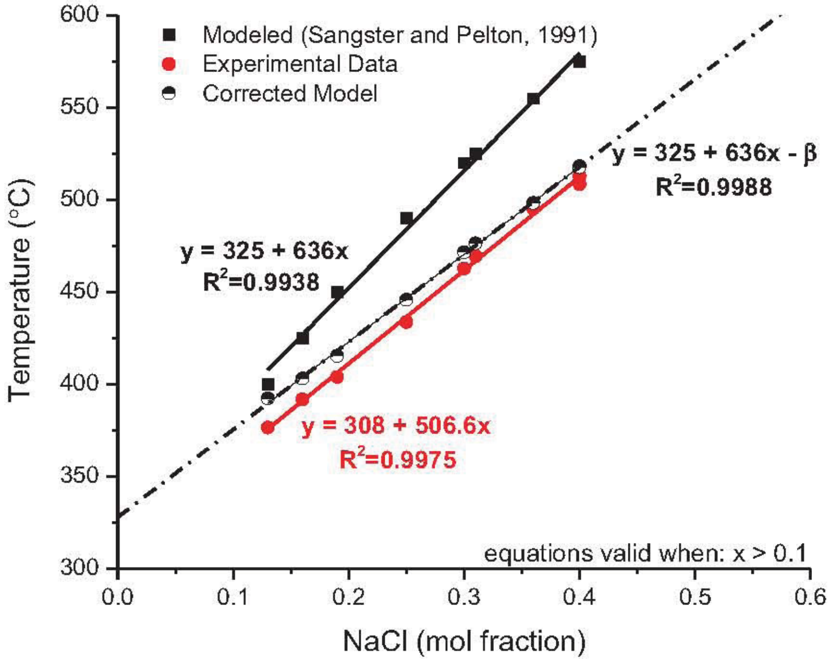

Figure 6.9: Plot of composition vs. liquidus temperature for modeled, experimental, and corrected model systems

As the concentration of NaCl increased the corrected model becomes more accurate. Table 6.7 shows the corrected model liquidus temperature, experimental liquidus temperature, and the difference between them. The model is off by at most 15.6°C and as little as 3.7°C for compositions of representative NaCl in the simulated salt samples between 0.1 and 0.4 mol fraction. The modeled, experimental and corrected model data can be fit using linear functions all giving R^2 values greater than 0.993.

Table 6.7: Comparison between corrected model data and experimental data

Sample	**β (°C)**	**Corrected Model Liquidus Temperature (°C)**	**Experimental Liquidus Temperature (°C)**	**Difference (°C)**
Before FFTF	15.2	392	376	15.6
After FFTF	23.4	403	392	11.3
INTEC B25	30.2	416	404	12.1
INTEC B50	37.7	446	434	12.3
INTEC B75	43.7	472	463	9.30
INTEC B100	45.2	477	470	7.60
INTEC B125	54.9	499	495	3.70
INTEC B150	60.4	519	513	6.00
INTEC B165	61.0	518	509	9.50

7. CONCLUSION AND FUTURE WORK

As the wt% of impurities (actinide, fission product, and bond sodium) increase, the liquidus temperature of the Mk-IV ER electrolyte increases. Although this general trend was expected, the exact nature of the trend, as a function of type and mass of spent fuel processed in the Mk-IV ER, was previously unknown. Therefore this study is the first of its kind which investigates the effects of electrorefining operations on the thermal characteristics of the electrolyte. From this study it can be concluded that in order to maintain a 100°C of superheat (defined as the difference between operating temperature and liquidus temperature), the impurity chloride concentration should not be greater than 35 wt%. The concentration of the salt is predicted to reach 35 wt% impurities after Batch 25 of INTEC fuel is processed. At that time the impurity concentration in the salt nears ~35 wt% and as a result it may be necessary to remove and/or replace some of the electrolyte in order to reduce the impurity concentration.

The experiments, carried out in the present study, have helped develop information that perhaps will prove to be very beneficial to the electrorefiner operators. If there is a question about the melting temperature of the salt in the ER, the operators can refer to this study to make a quick determination as to the condition (homogeneity) of the salt. This study provides an estimate of the melting temperature of the salt based on two different assumptions. (1) Considering the salt sample to be composed of just three metal chlorides (KCl, LiCl, and NaCl) and (2) the sodium chloride concentration is equal to the composition of all other salt constituents except those of KCl and LiCl. Both assumptions yielded results with relatively good accuracy. Assumption one yielded results within ±35°C and assumption two yielded results within ±12°C, with better accuracy upon gradual increase in the NaCl concentrations.

Using the information, obtained in the, present studies this research allows the INL to predict when salt removal from the ER will become necessary to support electrorefining operations. This work also shows that the liquidus temperature of the electrolyte in the Mk-IV ER is a function of NaCl concentration. Therefore to prolong the life of the salt, it may be beneficial to remove NaCl from the spent fuel before electrorefining takes place. The salt removed from the Mk-IV ER can be incorporated into a ceramic waste form, suitable for disposition into a geologic repository.

The present study has provided a strong platform for similar research and is a good foundation for experiments to aid in predicting the thermal behavior of a system using radiological components. A logical extension of this study will therefore be to repeat the same set of experiments using UCl_3 and $PuCl_3$. Working with radioactive material is more involved than working with non-radioactive samples. For future work either at the Idaho National Laboratory or in a university there just needs to be a DSC capable of handling radioactive samples. Once such a DSC is obtained it could also be used to generate thermodynamic data on systems of interest to pyroprocessing. Research systems may include: LiCl-KCl-UCl_3, LiCl-KCl-$PuCl_3$, LiCl-KCl-$NpCl_3$, etc. Although few studies on the LiCl-KCl-UCl_3 system have been reported no studies on the ternary chloride system with transuranic elements exists in open literature. These are fundamental studies that need to be investigated. This work is a good introduction to DSC concepts and capabilities with respect to developing phase diagrams for radiological and non-radiological systems.

8. REFERENCES

Ackerman, J. P. (1991). Chemical Basis for Pyrochemical Reprocessing of Nuclear Fuel. *Industrial & Engineering Chemistry Research, 31,* p141.

ASTM. (2007). Standard Terminology Relating to Thermophysical Properties, *Standard U.S.C. E 1142-07.*

ASTM. (2010). Standard Terminology Relating to Thermal Analysis and Rheology, *Standard U.S.C. E473-10.*

Basin, A.S., Kaplun, A.B., Meshalkin, A.B. and Uvarov, N.F. (2008). The LiCl-KCl Binary System. *Russian Journal of Inorganinc Chemistry*. 53(9) p1509

Blander, M. (2000). Fundamental Theories and Concepts for Predicting Thermodynamic Properties of High Temperature Ionic and Metallic Liquid Solutions and Vapor Molecules. *Metallurgical and Materials Transactions, 31B*, p579.

Burkes, D. E., Fielding, R. S., Porter, D. L., Crawford, D. C., and Meyer, M. K. (2009). A US Perspective on Fast Reactor Fuel Fabrication Technology and Experience Part I: Metal fuels and assembly design. *Journal of Nuclear Materials*, 389(3), p458.

Chang, Y.I. (1989). The Integral Fast Reactor. *Nuclear Technology*, 88, p129.

Cochran, R. G. and Tsoulfanidis, N. (1999). The Nuclear Fuel Cycle: Analysis and Management (2nd ed.) American Nuclear Society. *La Grange Park, Il.*

Flood, H. and Urnes, S. (1955). Die Berechnung Der Aktivitaten in Magnesium Chlorid-Alkalichlorid Schmelzen Aus Strukturmodellen. *Zeitschrift Fur Elektrochemie*. 59 (9), p834.

Franzosini, P. and Sanesi, M. (1983). Thermal Methods. In D. G. Lovering, and R. J. Gale. Molten Salt Techniques (Ed. 1) Vol 1, p177. *New York, NY: Plenum Press.*

Fredrickson, G.L., Yoo, T. and Vaden, D.E. (2010). Treating FFTF "U-Zr" and EBR-II "U-Fs" Fuels in the Mk-IV and Mk-V Electrorefiners. Department of Energy, Idaho National Laboratory. *Technical Evaluation Study (TEV-976)*. Unpublished Work. U.S. Government.

Garn, P. D. (1961). Thermal Analysis. A Critique. *Analytical Chemistry, 33*(9), p124.

Goff, K. M. and Simpson, M. F. (2009). Dry Processing of Used Nuclear Fuel. *Proceedings of Global*, Paris, France. , 9516.

Grimshaw, R.W., Heaton, E. and Roberts, A.L. (1945). The constitution of refractory clays. *Transactions of the British Ceramic Society*. 44, p69

Hersh, L.S. and Kleppa, O.J. (1965). Enthalpies of Mixing in Some Binary Liquid Halide Mixtures. *Journal of Chemical Physics*. 42, p1309.

Hohne, G. W., Hemminger, W., and Flammersheim, H. J. (2003). Differential Scanning Calorimetry (2nd ed.). *New York: Springer-Verlag Berlin Heidelberg.*

Hore-Lacy, I. (2003). Nuclear engineering in the 21st century (7th ed.). *Massachusetts: World Nuclear University Press.*

Johnson, I. (1988). The Thermodynamics of Pyrochemical Processes for Liquid Metal Reactor Fuel Cycles. *Journal of Nuclear Materials,* 154, p169.

Korin, E. and Soifer, L. (1997). Thermal Analysis of the System LiCl-KCl by Differential Scanning Calorimetry. *Journal of Thermal Analysis. 50*(3), p347.

Lahm, C. E., Koenig, J. F., Pahl, R. G., Porter, D. L., and Crawford, D. C. (1993). Experience with Advanced Driver Fuels in EBR-II. *Journal of Nuclear Materials, 204*, p119.

Laidler, J. J. (1993). Pyrochemical Recovery of Actinides. *Proceedings of the American Power Conference,* Chicago, Illinois. , *5,* p1074.

Lewis, E. E. (1978). Nuclear Power Reactor Safety. *New York, NY: Wiley Publishing.*

Li, S. X., Johnson, T. A., Westphal, B. R., Goff, K. M., and Benedict, R. W. (2005). Electrorefining Experience for Pyrochemical Processing of Spent EBR-II Driver Fuel. *Global,* Tsukuba, Japan.

Madson, A. A., and Laug, M. T. (1972). Xenon-Tagging of EBR-II Driver Fuel. EBR-II project. (*Technical Report No. ANL/EBR--57*). Argonne National Lab., Ill. Argonne National Lab., Idaho Falls, Id: Department of Energy.

Melling R., Wilburn, F. W., and McIntosh, R. M. (1969). Study of Thermal Effects Observed by Differential Thermal Analysis. Theory and its application to influence of sample parameters on a typical DTA curve. *Analytical Chemistry, 41*(10), 1275.

Moore, J. J. (1990). Slag chemistry. In Chemical Metallurgy (2nd ed., p152) *London; Boston; Butterworths.*

Nesshoefer, C. A., (2000). *EBR*-II Pre-Demolition Source Term. Radcon Technical Basis (TBL-194), 441.A16. Rev. 0, p4, *http://ar.inel.gov/images/pdf/200911/2009111100608TUA.pdf*

Netzsch. (2009). The best thermal analysis methods for your application. *Personal communications.*

Netzsch. (2010). Calibrations (Sensitivity and Temperature). Proetus ® Software for thermal analysis. V5.2.1/29.11.2011. *Help Menu: Netzsch.*

Øye, H. A. (2000). The Power of Thermodynamic Modeling; Examples from Molten Halide Mixtures. *Metallurgical and Materials Transactions B, 31*(4), p641.

Pella, E. and Nebuloni, M. (1971). Temperature Measurements with a Differential Calorimeter. *Journal of Themal Analysis and Calorimetry.* 3, p229.

Phongikaroon, S. (2011). Molten salt technology (NE504). Lecture 3 - Thermal Methods and Phase Diagrams of Molten Salts. *University of Idaho: Idaho Falls, ID*

Pitner, A. L. and Baker, R. B. (1993). Metal Fuel Test Program in the FFTF. *Journal of Nuclear Materials, 204*(0), p124.

Reiss, H., Katz, J., Kleppa, J. (1962). Theories of the Heats of Mixing of Certain Fused Salts. *Journal of Chemical Physics.* 36(1), p144.

Richards, T.W. and Meldrum, R.W. (1917). The Melting Point of the Lithium, Rubidium, and Caesium, and the Freezing Points of Binary and Ternary Mixtures of These Salts, Including also Potassium and Sodium Chloride. *Journal of the American Chemical Society*, 39 (9), p1816

Sangster J. and Pelton, D. (1987). Phase Diagrams and Thermodynamic Properties of the 70 Binary Alkali Halide Systems Having Common Ions. *Journal of Physical and Chemical Reference Data. 16*, p509.

Sangster J. and Pelton, D. (1991) Thermodynamic Calculation of Phase Diagrams of the 60 Common-Ion Ternary Systems Containing Cations Li, Na, K, Rb, Cs and Anions F, Cl, Br, I. *Journal of Phase Equilibria,* 12(15), p511.

Schindler, A. (2010). STA - Techniques, Instruments, and Instrumentation. *Netzsch. Personal communications.*

Simpson, M. F. and Law, J. D. (2010). Nuclear Fuel Rreprocessing. *url: http://www.inl.gov/technicalpublications/Documents/4460757.pdf.*

Smith , J.M., Van Ness, H.C. and Abbott, M.M. (2005). Introduction to Chemical Engineering Thermodynamics. (7th ed.) *New York, NY. McGraw-Hill.*

Speil, S., Berkelhamer, I.H., Pask, J.A. and Davies, B. (1945) Differential Thermal Analysis. Its Application to Clays and Other Aluminous Minerals: *U.S. Bureau Of Mines*, Tech. Paper 664.

Temkin, M. (1945). Mixtures of Fused Salts as Ionic Solutions. *Acta Physicochim*, URSS, vol 20, p411.

Vaden, D. (2005). Fuel Conditioning Facility Electrorefiner Process Model. *Separation Science and Technology, 41*(10), p2003.

Wendlandt, W. W. (1974). Thermal Methods of Analysis. (2nd ed.). *New York: Wiley-Interscience. New York.*

West, D.R.F and Saunders, N. (2002). Ternary Phase Diagrams in Materials Science. (3rd ed.) *Carlton House Terrace, London. Maney Publishing.*

Westphal, B. R., Mariani, R. D., Vaden, D. E., Sherman, S. R., Li, S. X., and Keiser, D. D., Jr. (2000). Recent Advances during the Treatment of Spent EBR-II Fuel. *ANS 4th Topical Meeting - DOE Spent Nuclear Fuel and Fissile Material Management,* San Diego, CA.

Westphal, B. R., Vaden, D., Li, S. X., Fredrickson, G. L., and Mariani, R. D. (2009). Fate of Noble Metal Fission Products during Electrorefining. *Proceedings of Global,* Paris, France. (9309)

WNA. World Nuclear Association. (07/11/2011). Processing of Used Nuclear Fuels. Retrieved 10/01/2011, from *http://world-nuclear.org/info/inf69.html.*

Yoo, T. (2011a). Updated Modeling and Simulation of FFTF Treatment Strategies. *Unpublished manuscript.*

Yoo, T. (2011b). Updated Modeling and Simulation of Fissium Treatment Strategies. *Unpublished manuscript.*

9. APPENDIX

Appendix A: Surrogate Mk-IV Salt Composition

Table A-1: Composition of Mk-IV salt and 15 g surrogate sample Before FFTF fuel processing

Before FFTF	Element	wt of Me in Mk-IV salt	% Me in Mk-IV salt	Calculated weight of MeCl_x for 15 g Surrogate Sample	Actual wt of MeCl_x in 15 g Sample	Actual wt of Me in 15 g Sample	wt% Me in 15 g sample
1	Chlorine	268417.70					
2	Potassium	96705.37	55.09%	6.3030	6.3030	3.3055	55.10%
3	Lithium	25011.34	14.25%	5.2218	5.2231	0.8551	14.25%
4	Uranium (Gd)	19897.29	11.34%	1.1402	1.1402	0.6801	11.34%
5	Sodium	14330.03	8.16%	1.2453	1.2455	0.4899	8.17%
6	Neodymium	4622.14	2.63%	0.2742	0.2732	0.1574	2.62%
7	Cesium	4283.10	2.44%	0.1850	0.1862	0.1474	2.46%
8	Plutonium (Gd)	3705.82	2.11%	0.2124	0.2123	0.1266	2.11%
9	Cerium	2431.27	1.39%	0.1459	0.1476	0.0841	1.40%
10	Lanthanum	1397.65	0.80%	0.0844	0.0844	0.0478	0.80%
11	Praseodymium	1245.51	0.71%	0.0747	0.0748	0.0426	0.71%
12	Samarium	1149.16	0.65%	0.0674	0.0585	0.0341	0.57%
13	Strontium	746.74	0.43%	0.0459	0.0514	0.0286	0.48%
Total		**443943.12**	**100.00%**	**15.0000**	**15.0002**	**5.9994**	**100.00%**

Table A-2. Composition of Mk-IV salt and 15 g surrogate sample After FFTF fuel processing

After FFTF	Element	wt of Me in Mk-IV salt	% Me in Mk-IV salt	Calculated weight of MeCl_x for 15 g Surrogate Sample	Actual wt of MeCl_x in 15 g Sample	Actual wt of Me in 15 g Sample	wt% Me in 15 g sample
1	Chlorine	258704.69			NA		
2	Potassium	87870.12	48.78%	5.7638	5.7638	3.0239	48.70%
3	Lithium	22724.54	12.61%	4.7733	4.7943	0.7855	12.65%
4	Uranium (Gd)	21827.91	12.12%	1.2589	1.2614	0.7527	12.12%
5	Sodium	16044.06	8.91%	1.4030	1.4059	0.5533	8.91%
6	Plutonium (Gd)	9555.20	5.30%	0.5511	0.5521	0.3294	5.31%
7	Neodymium	6940.88	3.85%	0.4143	0.2977	0.1716	2.76%
8	Cesium	4814.50	2.67%	0.2093	0.2971	0.2352	3.79%
9	Cerium	3765.47	2.09%	0.2274	0.2279	0.1299	2.09%
10	Lanthanum	2101.88	1.17%	0.1277	0.1279	0.0725	1.17%
11	Praseodymium	1917.06	1.06%	0.1157	0.1161	0.0662	1.07%
12	Samarium	1671.39	0.93%	0.0987	0.0987	0.0575	0.93%
13	Strontium	919.13	0.51%	0.0568	0.0572	0.0318	0.51%
Total		**438856.83**	**100.00%**	**15.0000**	**15.0001**	**6.2094**	**100.00%**

Table A-3. Composition of Mk-IV salt and 15 g surrogate sample after INTEC B25

INTEC B25	**Element**	**wt of Me in Mk-IV salt**	**% Me in Mk-IV salt**	**Calculated weight of $MeCl_x$ for 15 g Surrogate Sample**	**Actual wt of $MeCl_x$ in 15 g Sample**	**Actual wt of Me in 15 g Sample**	**wt% Me in 15 g sample**
1	Chlorine	258091.64					
2	Potassium	84430.762	45.35%	5.4400	5.4400	2.8617	45.36%
3	Uranium (Gd)	24290.255	13.05%	1.3760	1.3760	0.8233	13.05%
4	Lithium	21869.152	11.75%	4.4871	4.4869	0.7412	11.75%
5	Sodium	19641.454	10.55%	1.6848	1.6851	0.6658	10.55%
6	Plutonium (Gd)	8790.6774	4.72%	0.4980	0.4975	0.2977	4.72%
7	Neodymium	7895.5492	4.24%	0.4629	0.4629	0.2676	4.24%
8	Cesium	5623.9491	3.02%	0.2405	0.2404	0.1905	3.02%
9	Cerium	4373.5367	2.35%	0.2593	0.2592	0.1482	2.35%
10	Lanthanum	2396.3796	1.29%	0.1430	0.1434	0.0815	1.29%
11	Praseodymium	2210.1174	1.19%	0.1310	0.1312	0.0750	1.19%
12	Samarium	1807.3677	0.97%	0.1048	0.1044	0.0610	0.97%
13	Barium (Sr)	1667.7765	0.90%	0.1019	0.1019	0.0565	0.90%
14	Strontium	1161.393	0.62%	0.0706	0.0708	0.0395	0.63%
Total		**444250.01**	**100.00%**	**15.0000**	**14.9997**	**6.3094**	**100.00%**

Table A-4: Composition of Mk-IV salt and 15 g surrogate sample after INTEC B50

INTEC B50	**Element**	**wt of Me in Mk-IV salt**	**% Me in Mk-IV salt**	**Calculated weight of $MeCl_x$ for 15 g Surrogate Sample**	**Actual wt of $MeCl_x$ in 15 g Sample**	**Actual wt of Me in 15 g Sample**	**wt% Me in 15 g sample**
1	Chlorine	257233.89					
2	Potassium	77241.503	39.77%	4.8766	4.8766	2.5617	39.77%
3	Uranium (Gd)	27436.795	14.13%	1.5230	1.5228	0.9098	14.12%
4	Sodium	25622.72	13.19%	2.1551	2.1547	0.8496	13.19%
5	Lithium	20006.999	10.30%	4.0336	4.0336	0.6635	10.30%
6	Neodymium	9833.3565	5.06%	0.5649	0.5649	0.3261	5.06%
7	Plutonium (Gd)	9213.2646	4.74%	0.5114	0.5114	0.3055	4.74%
8	Cesium	7116.5501	3.66%	0.2980	0.2982	0.2362	3.67%
9	Cerium	5522.1838	2.84%	0.3209	0.3214	0.1834	2.85%
10	Lanthanum	2989.0321	1.54%	0.1747	0.1749	0.0992	1.54%
11	Praseodymium	2777.0663	1.43%	0.1613	0.1611	0.0920	1.43%
12	Barium (Sr)	2765.1073	1.42%	0.1656	0.1656	0.0917	1.42%
13	Samarium	2171.9301	1.12%	0.1234	0.1237	0.0722	1.12%
14	Strontium	1535.999	0.79%	0.0914	0.0914	0.0509	0.79%
Total		**451466.40**	**100.00%**	**15.0000**	**15.0003**	**6.4420**	**100.00%**

Table A-5. Composition of Mk-IV salt and 15 g surrogate sample after INTEC B75

INTEC B75	**Element**	**wt of Me in Mk-IV salt**	**% Me in Mk-IV salt**	**Calculated weight of $MeCl_x$ for 15 g Surrogate Sample**	**Actual wt of $MeCl_x$ in 15 g Sample**	**Actual wt of Me in 15 g Sample**	**wt% Me in 15 g sample**
1	Chlorine	253591.18					
2	Potassium	70717.12	36.28%	4.4964	4.4964	2.3628	36.28%
3	Sodium	31115.06	15.96%	2.6355	2.6351	1.0395	15.96%
4	Uranium (Gd)	23493.69	12.05%	1.3135	1.3135	0.7850	12.05%
5	Lithium	18317.06	9.40%	3.7182	3.7179	0.6120	9.40%
6	Neodymium	11613.86	5.96%	0.6720	0.6718	0.3879	5.96%
7	Plutonium (Gd)	9606.56	4.93%	0.5371	0.5365	0.3206	4.92%
8	Cesium	8472.98	4.35%	0.3574	0.3578	0.2834	4.35%
9	Cerium	6577.37	3.37%	0.3849	0.3850	0.2198	3.38%
10	Barium (Sr)	3786.03	1.94%	0.2284	0.2284	0.1265	1.94%
11	Lanthanum	3533.56	1.81%	0.2080	0.2080	0.1180	1.81%
12	Praseodymium	3297.92	1.69%	0.1930	0.1933	0.1104	1.69%
13	Samarium	2506.47	1.29%	0.1435	0.1434	0.0837	1.29%
14	Strontium	1871.12	0.96%	0.1122	0.1123	0.0626	0.96%
Total		**448500.00**	**100.00%**	**15.0000**	**14.9994**	**6.5122**	**100.00%**

Table A-6. Composition of Mk-IV salt and 15 g surrogate sample after INTEC B100

INTEC B100	**Element**	**wt of Me in Mk-IV salt**	**% Me in Mk-IV salt**	**Calculated weight of $MeCl_x$ for 15 g Surrogate Sample**	**Actual wt of $MeCl_x$ in 15 g Sample**	**Actual wt of Me in 15 g Sample**	**wt% Me in 15 g sample**
1	Chlorine	252243.85					
2	Potassium	69470.65	35.48%	4.4089	4.4089	2.3181	35.47%
3	Sodium	32453.71	16.57%	2.7425	2.7432	1.0832	16.58%
4	Uranium (Gd)	23860.55	12.18%	1.3313	1.3313	0.7962	12.18%
5	Lithium	18020.70	9.20%	3.6435	3.6436	0.6013	9.20%
6	Neodymium	11885.85	6.07%	0.6863	0.6865	0.3967	6.07%
7	Plutonium (Gd)	8919.75	4.55%	0.4977	0.4975	0.2975	4.55%
8	Cesium	8708.50	4.45%	0.3667	0.3664	0.2903	4.44%
9	Cerium	6770.95	3.46%	0.3955	0.3956	0.2260	3.46%
10	Barium (Sr)	4258.20	2.17%	0.2564	0.2563	0.1421	2.17%
11	Lanthanum	3618.68	1.85%	0.2126	0.2126	0.1207	1.85%
12	Praseodymium	3388.04	1.73%	0.1979	0.1982	0.1133	1.73%
13	Samarium	2522.66	1.29%	0.1441	0.1446	0.0845	1.29%
14	Strontium	1948.74	1.00%	0.1166	0.1167	0.0651	1.00%
Total		**448070.84**	**100.00%**	**15.0000**	**15.0014**	**6.5349**	**100.00%**

Table A-7. Composition of Mk-IV salt and 15 g surrogate sample after INTEC B125

INTEC B125	Element	wt of Me in Mk-IV salt	% Me in Mk-IV salt	Calculated weight of $MeCl_x$ for 15 g Surrogate Sample	Actual wt of $MeCl_x$ in 15 g Sample	Actual wt of Me in 15 g Sample	wt% Me in 15 g sample
1	Chlorine	252152.88					
2	Potassium	63634.61	31.31%	3.9633	3.9633	2.0844	31.31%
3	Sodium	37386.00	18.40%	3.1001	3.1002	1.2246	18.40%
4	Uranium (Gd)	27011.76	13.29%	1.4791	1.4791	0.8848	13.29%
5	Lithium	16506.83	8.12%	3.2745	3.2748	0.5407	8.12%
6	Neodymium	13499.14	6.64%	0.7650	0.7653	0.4423	6.64%
7	Cesium	9912.80	4.88%	0.4097	0.4095	0.3245	4.87%
8	Plutonium (Gd)	9342.22	4.60%	0.5116	0.5119	0.3062	4.60%
9	Cerium	7724.17	3.80%	0.4427	0.4429	0.2531	3.80%
10	Barium (Sr)	5177.48	2.55%	0.3059	0.3056	0.1694	2.55%
11	Lanthanum	4111.90	2.02%	0.2371	0.2371	0.1347	2.02%
12	Praseodymium	3859.05	1.90%	0.2212	0.2210	0.1263	1.90%
13	Samarium	2827.87	1.39%	0.1586	0.1589	0.0928	1.39%
14	Strontium	2236.40	1.10%	0.1313	0.1315	0.0733	1.10%
Total		**455383.10**	**100.00%**	**15.0000**	**15.0011**	**6.6573**	**100.00%**

Table A-8: Composition of Mk-IV salt and 15 g surrogate sample after INTEC B150

INTEC B150	Element	wt of Me in Mk-IV salt	% Me in Mk-IV salt	Calculated weight of $MeCl_x$ for 15 g Surrogate Sample	Actual wt of $MeCl_x$ in 15 g Sample	Actual wt of Me in 15 g Sample	wt% Me in 15 g sample
1	Chlorine	249193.83					
2	Potassium	58326.54	28.69%	3.6590	3.6590	1.9248	28.69%
3	Sodium	41928.58	20.62%	3.5018	3.5015	1.3836	20.62%
4	Uranium (Gd)	23094.75	11.36%	1.2738	1.2738	0.7621	11.36%
5	Lithium	15129.91	7.44%	3.0225	3.0224	0.4993	7.44%
6	Neodymium	14985.74	7.37%	0.8554	0.8555	0.4946	7.37%
7	Cesium	11009.95	5.42%	0.4584	0.4580	0.3630	5.41%
8	Plutonium (Gd)	9735.06	4.79%	0.5370	0.5372	0.3214	4.79%
9	Cerium	8602.38	4.23%	0.4967	0.4966	0.2838	4.23%
10	Barium (Sr)	6035.50	2.97%	0.3592	0.3590	0.1991	2.97%
11	Lanthanum	4566.38	2.25%	0.2652	0.2649	0.1505	2.24%
12	Praseodymium	4293.01	2.11%	0.2478	0.2480	0.1418	2.11%
13	Samarium	3108.74	1.53%	0.1756	0.1758	0.1027	1.53%
14	Strontium	2493.98	1.23%	0.1476	0.1478	0.0824	1.23%
Total		**452504.36**	**100.00%**	**15.0000**	**14.9995**	**6.7091**	**100.00%**

Table A-9: Composition of Mk-IV salt and 15 g surrogate sample after INTEC B165

INTEC B165	**Element**	**wt of Me in Mk-IV salt**	**% Me in Mk-IV salt**	**Calculated weight of $MeCl_x$ for 15 g Surrogate Sample**	**Actual wt of $MeCl_x$ in 15 g Sample**	**Actual wt of Me in 15 g Sample**	**wt% Me in 15 g sample**
1	Chlorine	243951.92					
2	Potassium	57972.19	28.87%	3.6888	3.6888	1.9410	28.87%
3	Sodium	40014.96	19.93%	3.3887	3.3891	1.3399	19.93%
4	Uranium (Gd)	26356.44	13.13%	1.4744	1.4743	0.8824	13.13%
5	Lithium	15054.57	7.50%	3.0460	3.0460	0.5040	7.50%
6	Neodymium	14224.63	7.09%	0.8235	0.8238	0.4764	7.09%
7	Cesium	10451.15	5.21%	0.4414	0.4416	0.3501	5.21%
8	Plutonium (Gd)	8917.88	4.44%	0.4989	0.4989	0.2986	4.44%
9	Cerium	8179.47	4.07%	0.4789	0.4786	0.2737	4.07%
10	Barium (Sr)	5877.44	2.93%	0.3547	0.3548	0.1968	2.93%
11	Lanthanum	4335.30	2.16%	0.2554	0.2556	0.1453	2.16%
12	Praseodymium	4079.54	2.03%	0.2388	0.2391	0.1367	2.03%
13	Samarium	2935.22	1.46%	0.1681	0.1679	0.0981	1.46%
14	Strontium	2371.44	1.18%	0.1423	0.1423	0.0794	1.18%
Total		**452504.36**	**100.00%**	**15.0000**	**15.0008**	**6.7224**	**100.00**

Appendix B: DSC Calibration Curves

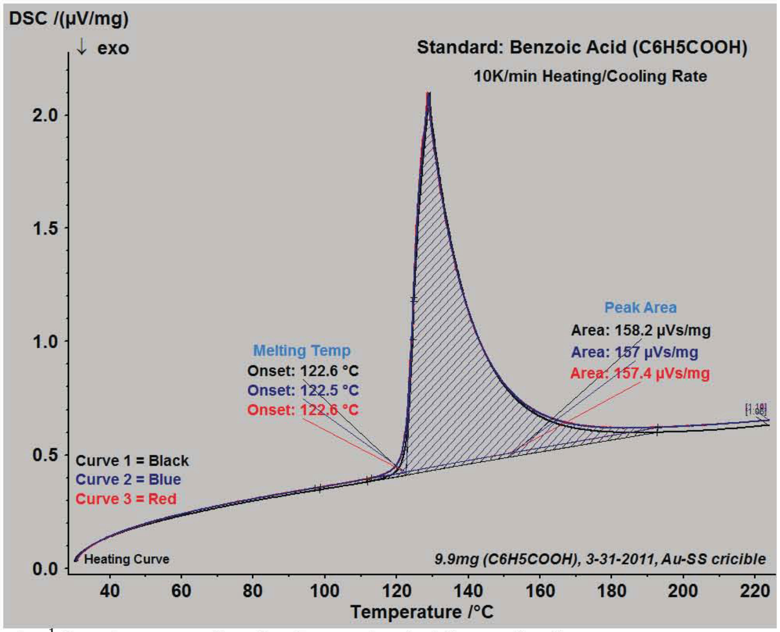

Figure B-1. 10 K min^{-1} heating rate for the Benzoic Acid standard

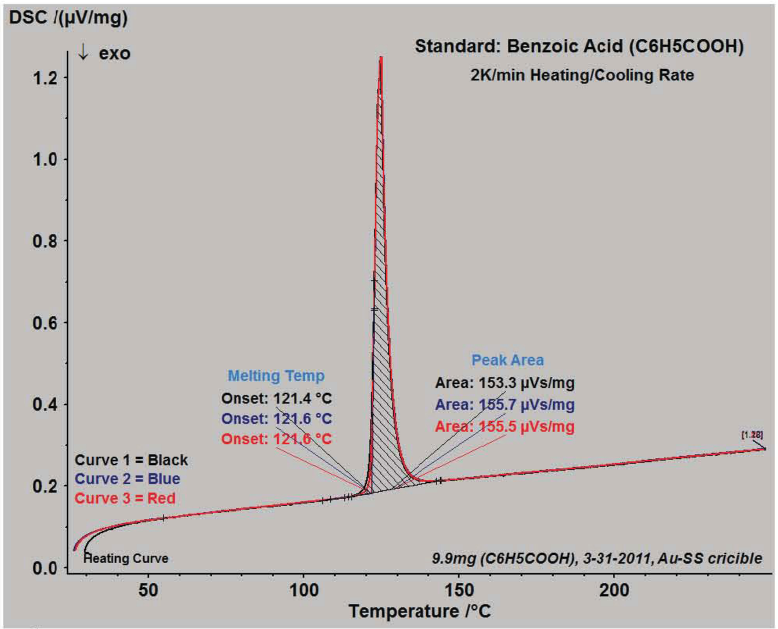

Figure B-2. 2 K min^{-1} heating rate for the Benzoic Acid standard

Table B-1. Onset and Peak values obtained from thermograms in Figure B-1 and B-2

Benzoic Acid Standard (C_6H_5COOH)					
10 K min^{-1}			2 K min^{-1}		
Cycle	Onset Temp, (°C)	Peak Area, (μVs/mg)	Cycle	Onset Temp, (°C)	Peak Area, (μVs/mg)
1	122.6	158.2	1	121.4	153.3
2	122.5	157.0	2	121.6	155.7
3	122.6	157.4	3	121.6	155.5
Avg	122.6	157.5	Avg	121.5	154.8

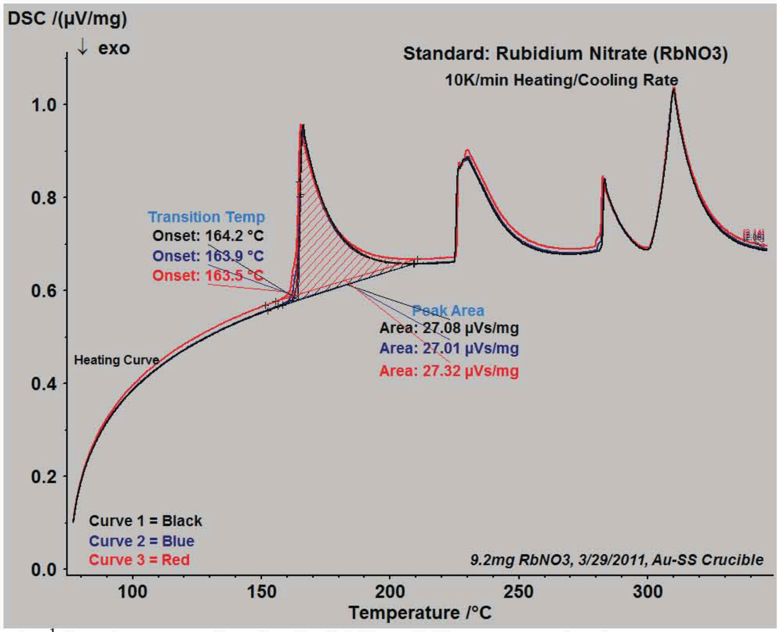

Figure B-3. 10 K min^{-1} heating rate for the Rubidium Nitrate standard

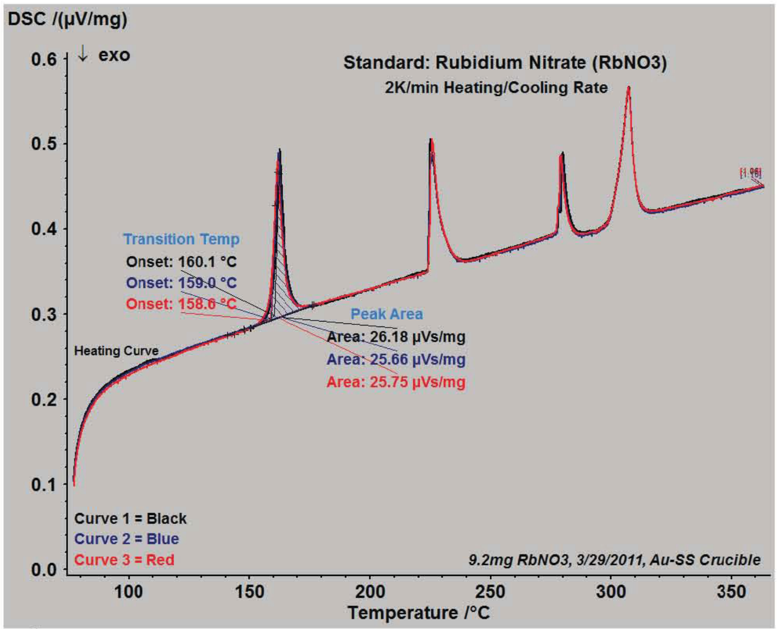

Figure B-4. 2 K min^{-1} heating rate for the Rubidium Nitrate standard

Table B-2. Onset and Peak values obtained from thermograms in Figure B-3 and B-4

Rubidium Nitrate Standard ($RbNO_3$)					
10 K min^{-1}			2 K min^{-1}		
Cycle	Onset Temp, (°C)	Peak Area, (μVs/mg)	Cycle	Onset Temp, (°C)	Peak Area, (μVs/mg)
1	164.2	27.08	1	160.1	26.18
2	163.9	27.01	2	159.0	25.66
3	163.5	27.32	3	158.6	25.75
Avg	163.9	27.1	Avg	159.2	25.9

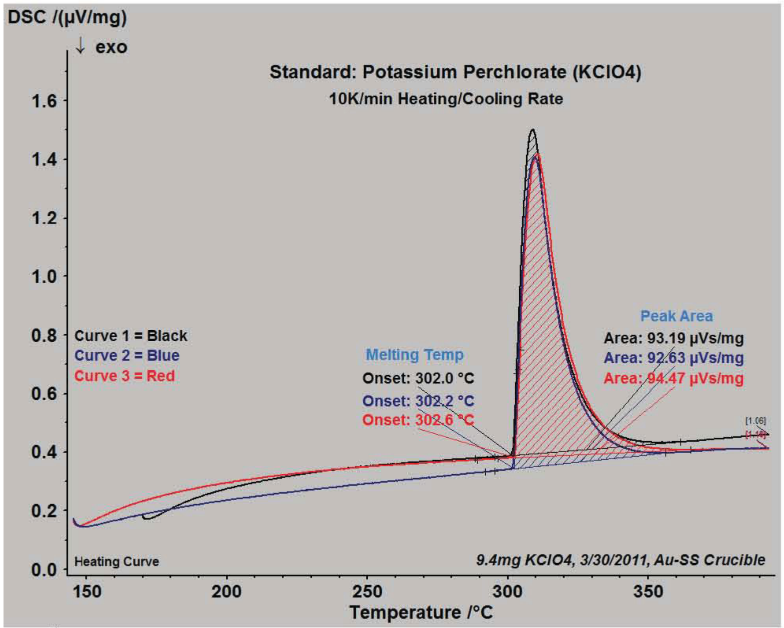

Figure B-5. 10 K min^{-1} heating rate for the Potassium Perchlorate standard

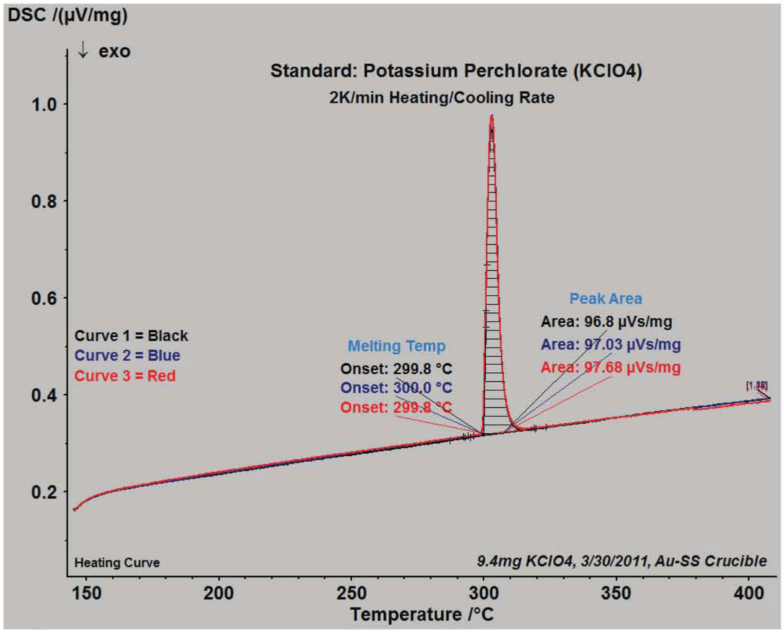

Figure B-6. 2 K min^{-1} heating rate for the Potassium Perchlorate standard

Table B-3. Onset and Peak values obtained from thermograms in Figure B-5 and B-6

Potassium Perchlorate Standard ($KClO_4$)					
10 K min^{-1}			2 K min^{-1}		
Cycle	Onset Temp, (°C)	Peak Area, (µVs/mg)	Cycle	Onset Temp, (°C)	Peak Area, (µVs/mg)
1	302.0	93.19	1	299.8	96.8
2	302.2	92.63	2	300.0	97.03
3	302.6	94.47	3	299.8	97.68
Avg	302.3	94.4	Avg	299.9	97.2

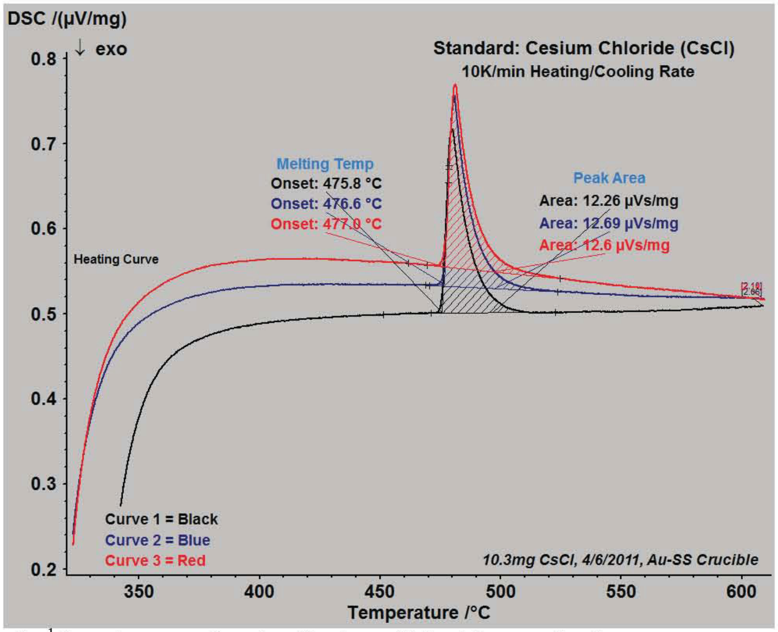

Figure B-7. 10 K min^{-1} heating rate for the Cesium Chloride standard

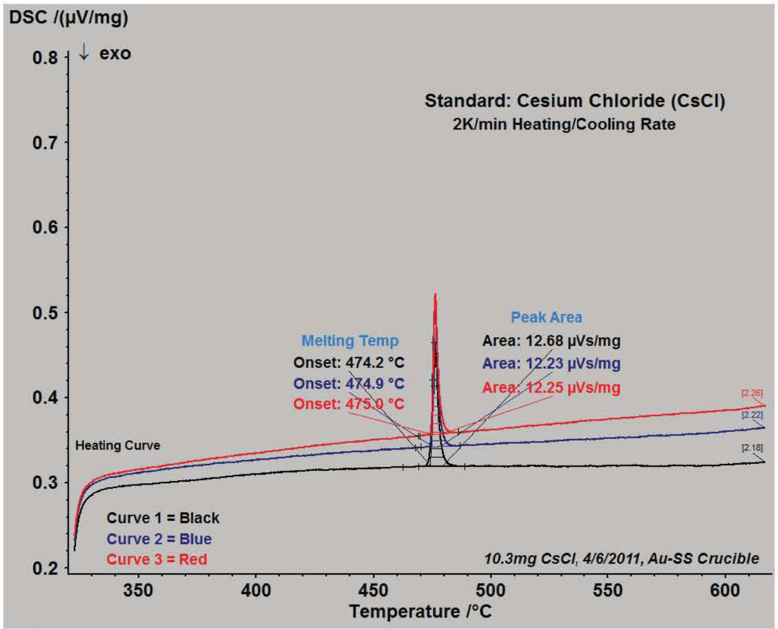

Figure B-8. 2 K min^{-1} heating rate for the Cesium Chloride standard

Table B-4. Onset and Peak values obtained from thermograms in Figure B-7 and B-8

Cesium Chloride Standard (CsCl)					
10 K min^{-1}			2 K min^{-1}		
Cycle	Onset Temp, (°C)	Peak Area, (µVs/mg)	Cycle	Onset Temp, (°C)	Peak Area, (µVs/mg)
1	475.8	12.26	1	474.2	12.68
2	476.6	12.69	2	474.9	12.23
3	477.8	12.6	3	475.0	12.25
Avg	476.5	12.5	Avg	474.7	12.4

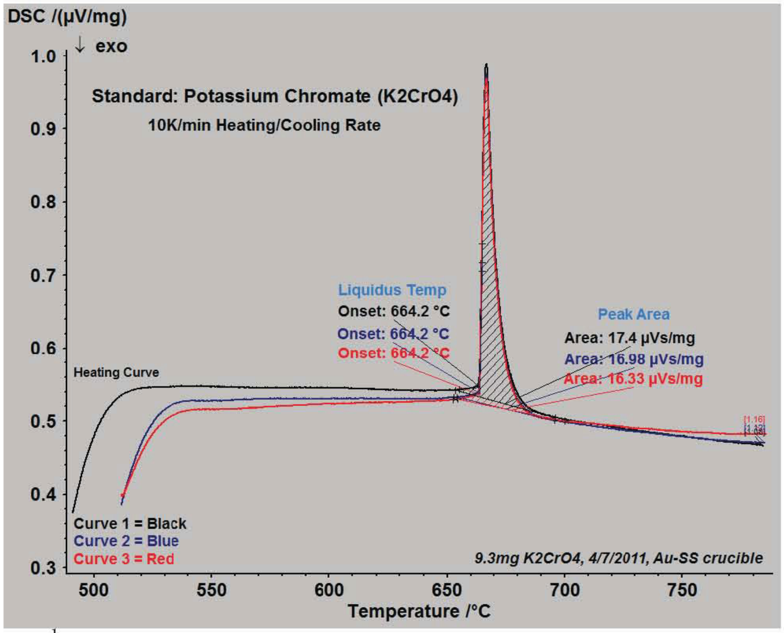

Figure B-9. 10 K min^{-1} heating rate for the Potassium Chromate standard

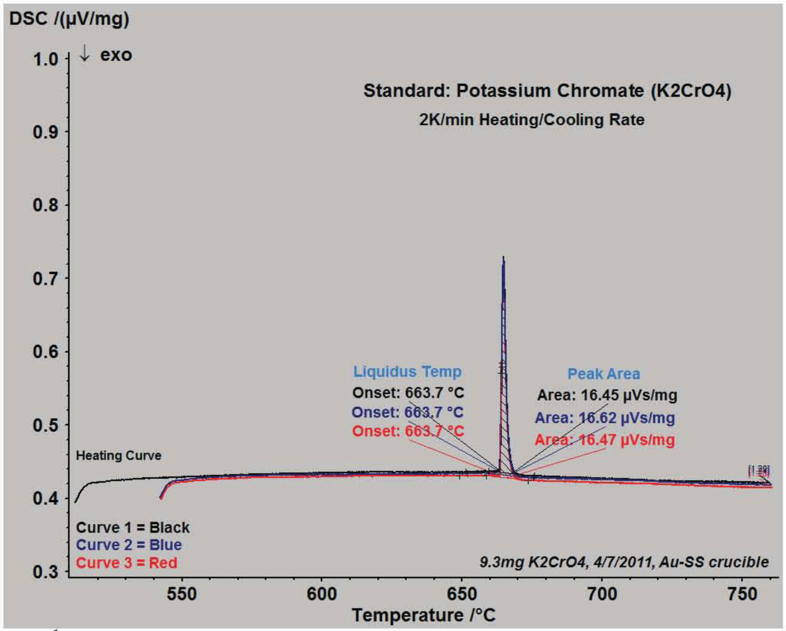

Figure B-10. 2 K min^{-1} heating rate for the Potassium Chromate standard

Table B-5. Onset and Peak values obtained from thermograms in Figure B-9 and B-10

Potassium Chromate Standard (K_2CrO_4)					
10 K min^{-1}			2 K min^{-1}		
Cycle	Onset Temp, (°C)	Peak Area, (µVs/mg)	Cycle	Onset Temp, (°C)	Peak Area, (µVs/mg)
1	664.2	17.4	1	663.7	16.45
2	664.2	16.98	2	663.7	16.62
3	664.2	16.33	3	663.7	16.47
Avg	664.2	16.9	Avg	663.7	16.5

Appendix C: LiCl-KCl Study

C.1 2 K min^{-1} Heating Rate

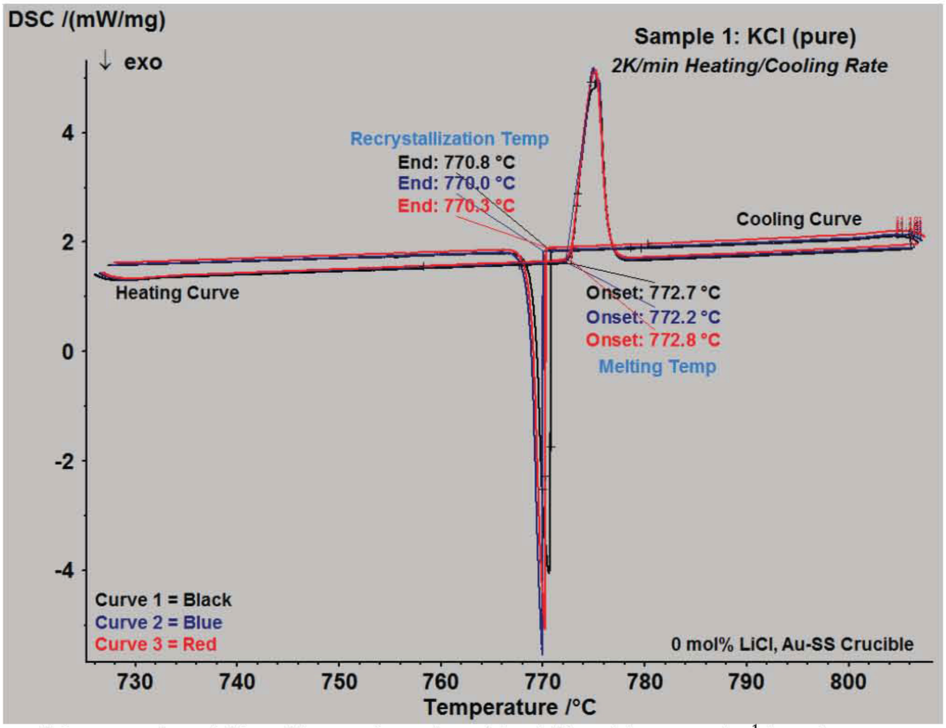

Figure C-1. DSC curve for LiCl-KCl sample 1 (0 wt% LiCl) with 2 K min^{-1} heating rate

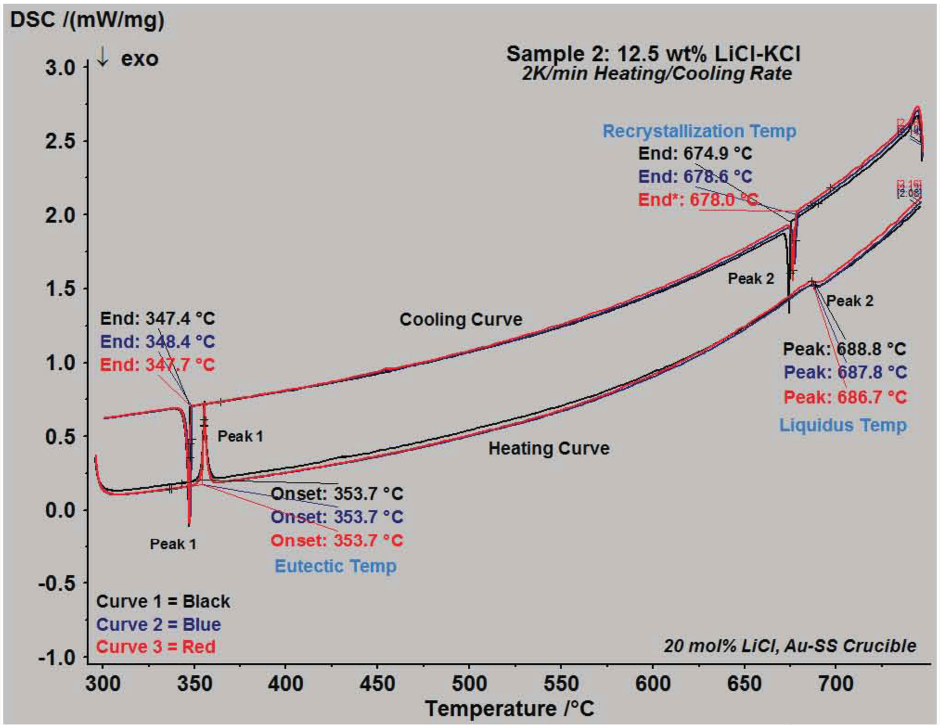

Figure C-2. DSC curve for LiCl-KCl sample 2 (12.5 wt% LiCl) with 2 K min^{-1} heating rate

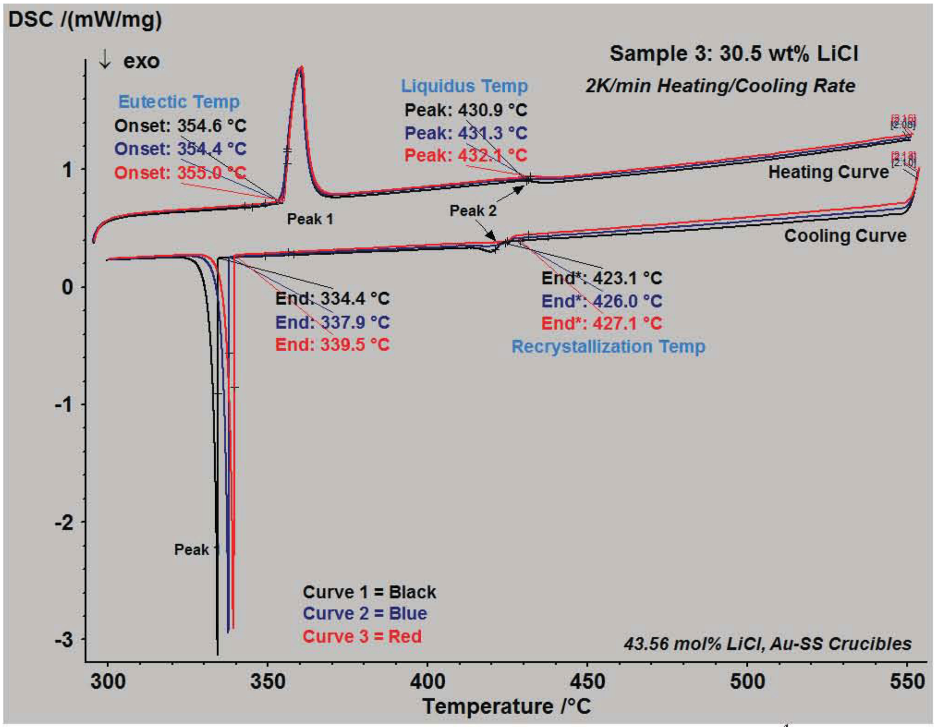

Figure C-3. DSC curve for LiCl-KCl sample 3 (30.5 wt% LiCl) with 2 K min^{-1} heating rate

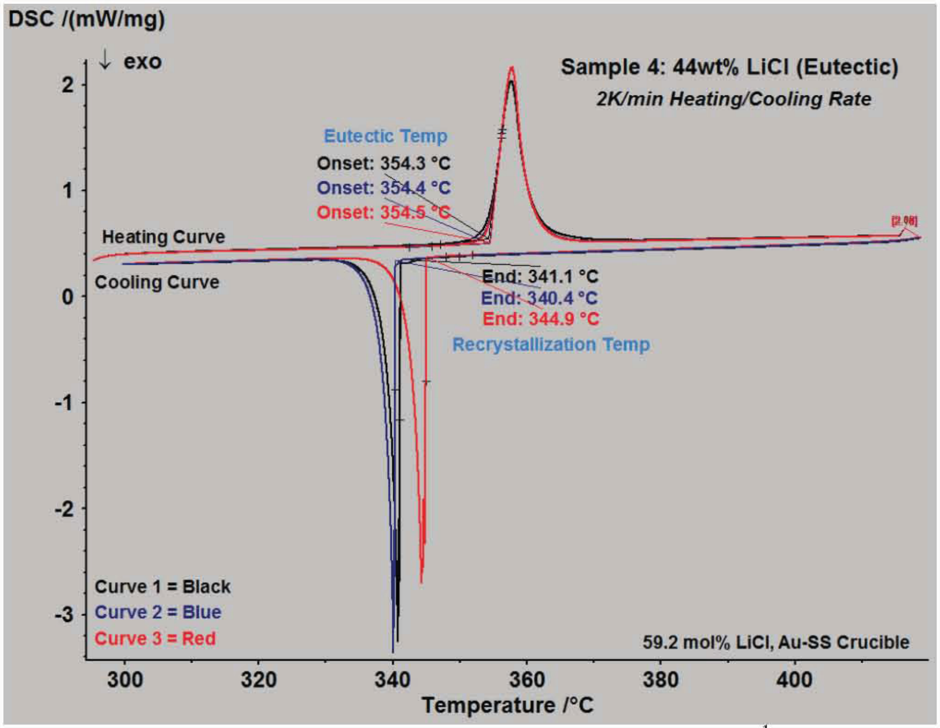

Figure C-4. DSC curve for LiCl-KCl sample 4 (44 wt% LiCl) with 2 K min^{-1} heating rate

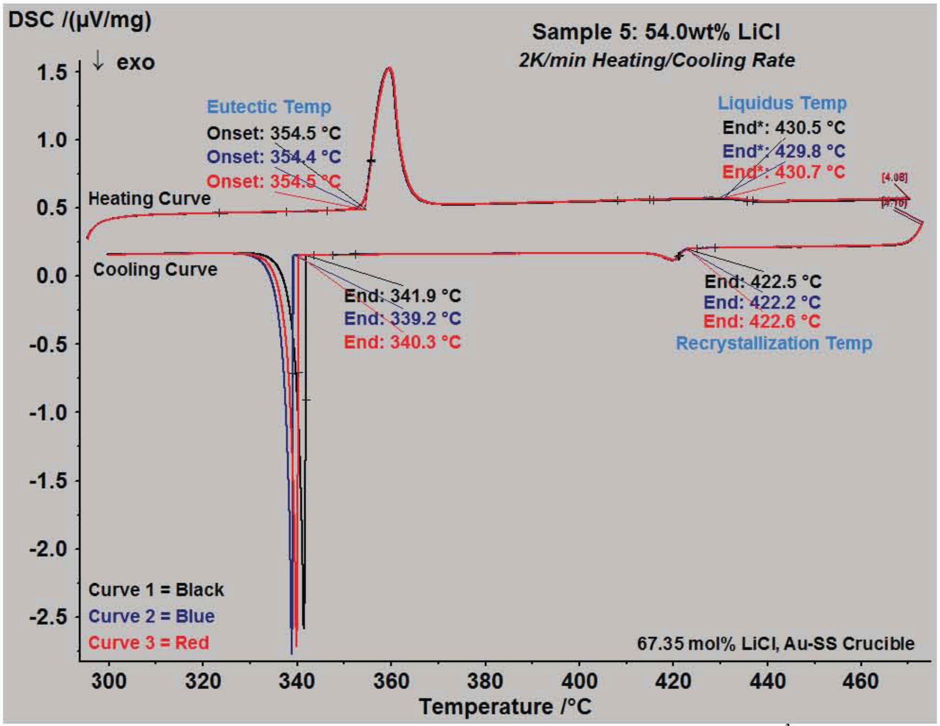

Figure C-5. DSC curve for LiCl-KCl sample 5 (54.0 wt% LiCl) with 2 K min^{-1} heating rate

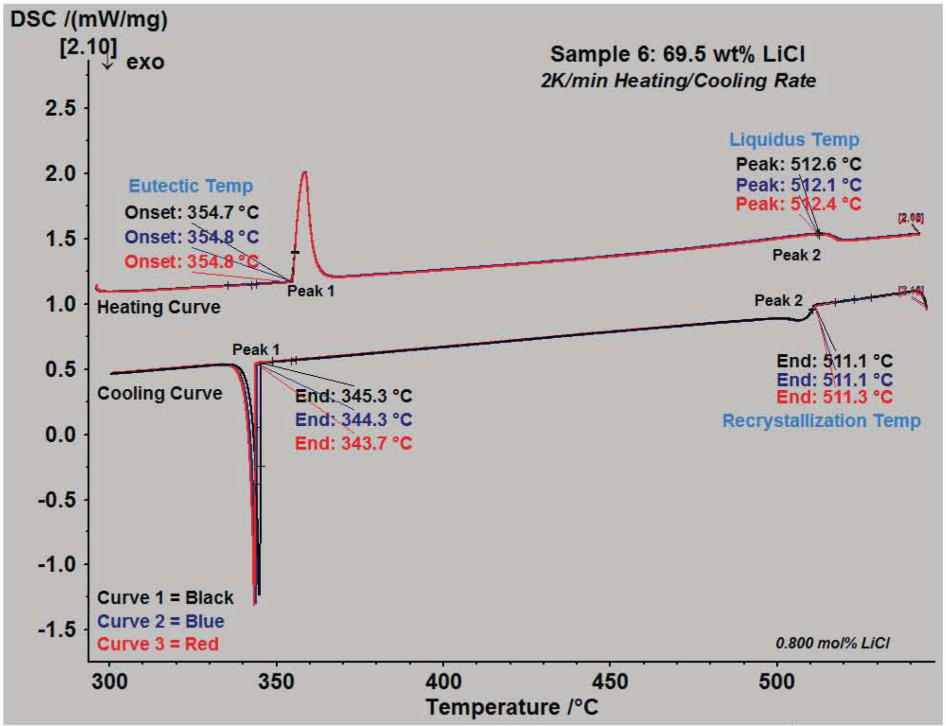

Figure C-6. DSC curve for LiCl-KCl sample 6 (69.5 wt% LiCl) with 2 K min^{-1} heating rate

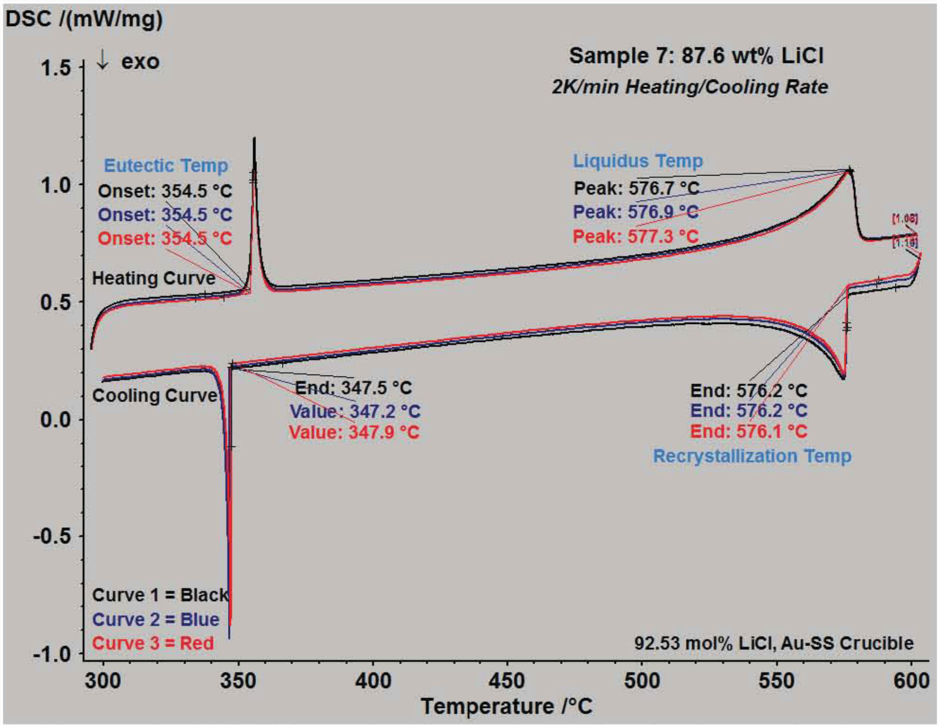

Figure C-7. DSC curve for LiCl-KCl sample 7 (87.6wt% LiCl) with 2 K min^{-1} heating rate

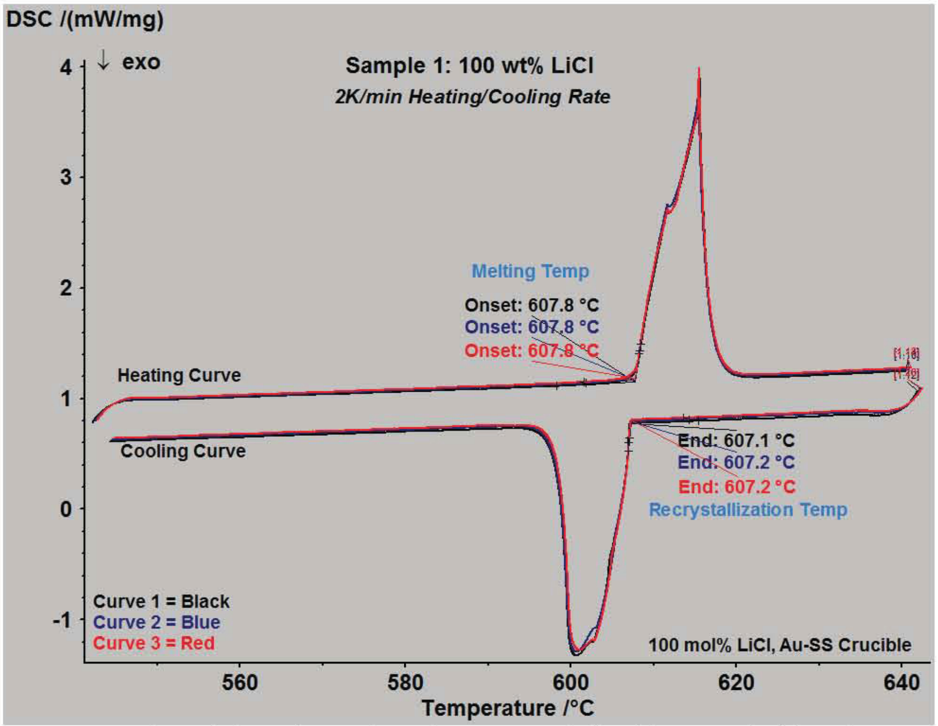

Figure C-8. DSC curve for LiCl-KCl sample 8 (100 wt% LiCl) with 2 K min^{-1} heating rate

Table C-1 provides information on the eutectic and liquidus temperatures for various compositions of LiCl-KCl with a heating/cooling rate of 2 K min^{-1}

Table C-1. Summary of results taken from Figure C-1 through Figure C-8

Summary: 2 K min^{-1} Heating Rate						
			Curve 1	Curve 2	Curve 3	Average
Sample 1	KCl (pure)	Eutectic Temp, °C	--	--	--	--
		Liquidus Temp, °C	770.8	770.0	770.3	770.4
Sample 2	12.5 wt% LiCl-KCl	Eutectic Temp, °C	353.7	353.7	353.7	353.7
		Liquidus Temp, °C	688.8	687.8	686.7	687.8
Sample 3	30.5 wt% LiCl-KCl	Eutectic Temp, °C	354.6	354.4	355.0	354.7
		Liquidus Temp, °C	--	--	--	--
Sample 4	44.0 wt% LiCl-KCl	Eutectic Temp, °C	354.3	354.4	354.5	354.4
		Liquidus Temp, °C	--	--	--	--
Sample 5	54.0 wt% LiCl-KCl	Eutectic Temp, °C	354.5	354.4	354.5	354.5
		Liquidus Temp, °C	430.5	429.8	430.7	430.3
Sample 6	69.5 wt% LiCl-KCl	Eutectic Temp, °C	354.7	354.8	354.8	354.8
		Liquidus Temp, °C	512.6	512.1	512.4	512.4
Sample 7	87.6 wt% LiCl-KCl	Eutectic Temp, °C	354.5	354.5	354.5	354.5
		Liquidus Temp, °C	576.7	576.9	577.3	577.0
Sample 8	LiCl (pure)	Eutectic Temp, °C	--	--	--	--
		Liquidus Temp, °C	607.8	607.8	607.8	607.8

C.1 10 K min^{-1} Heating Rate

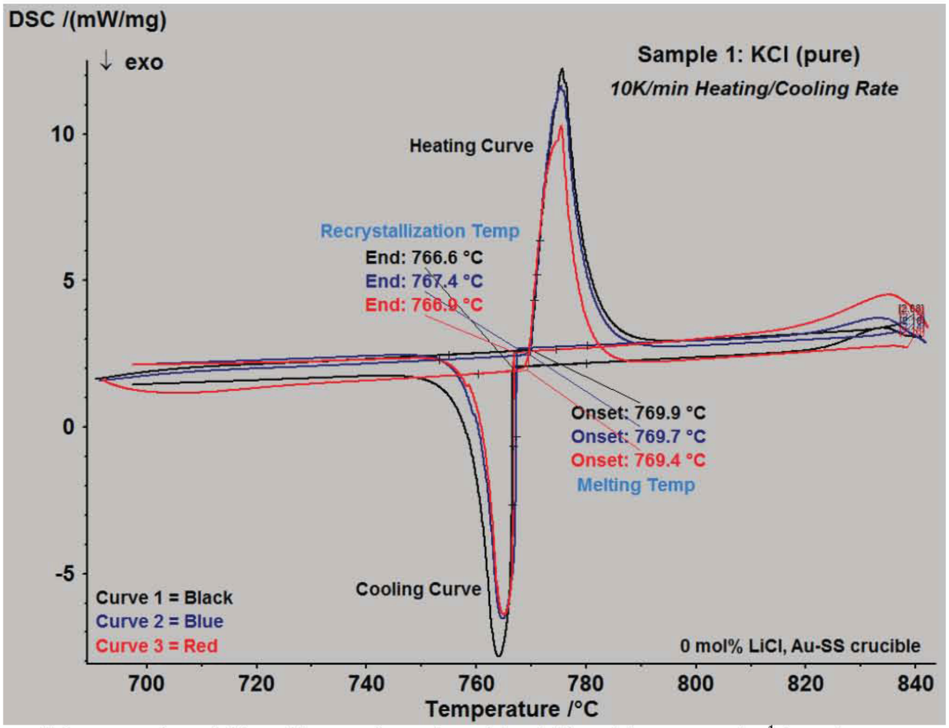

Figure C-9. DSC curve for LiCl-KCl sample 1 (0 wt% LiCl) with 10 K min^{-1} heating rate

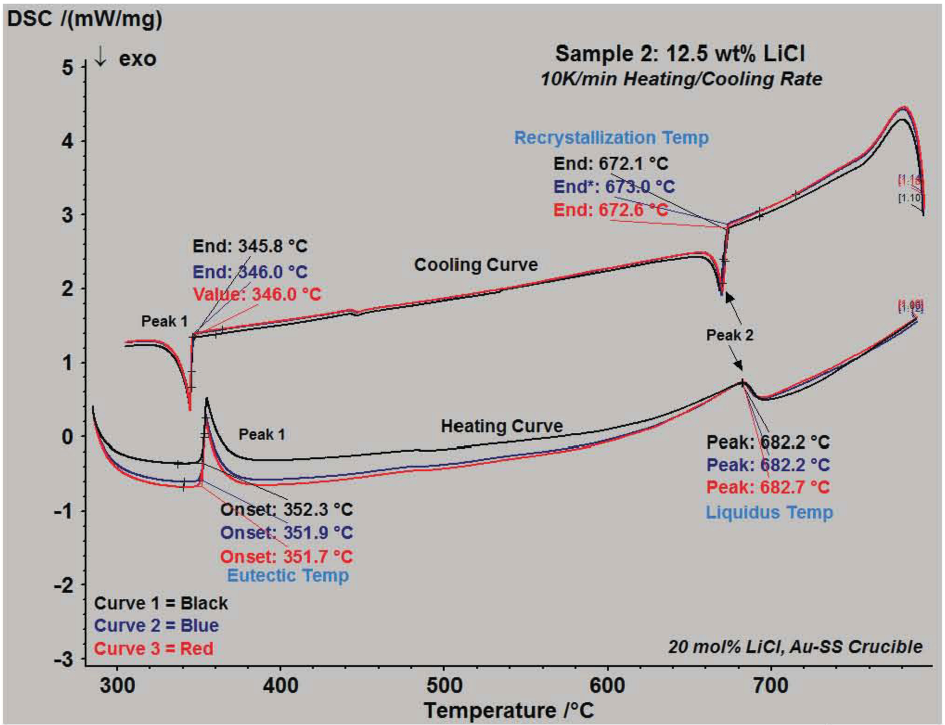

Figure C-10. DSC curve for LiCl-KCl sample 10 (12.5wt% LiCl) with 10 K min^{-1} heating rate

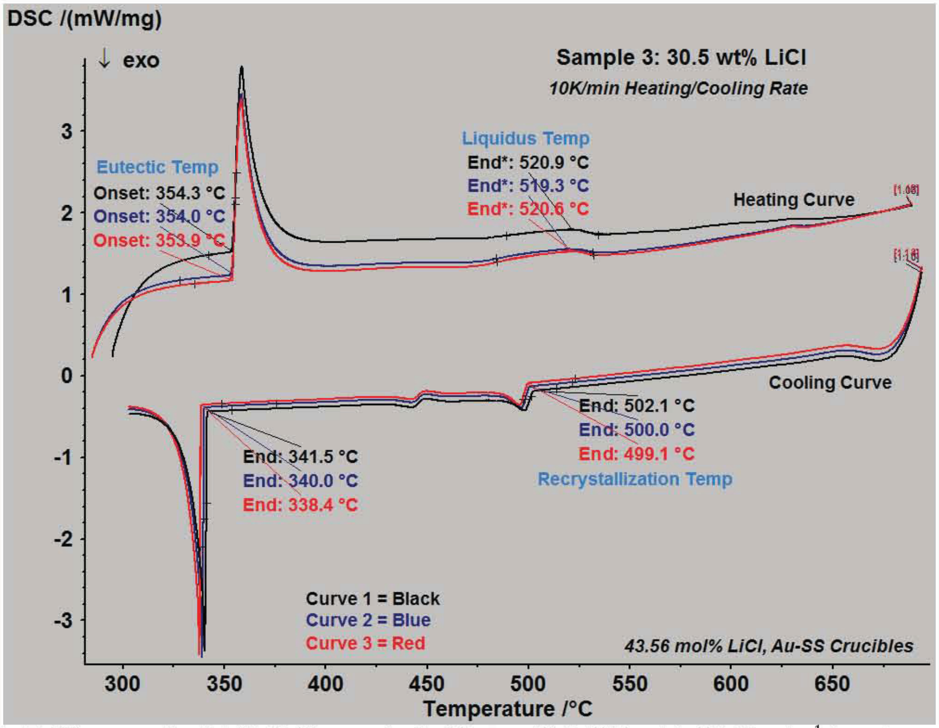

Figure C-11. DSC curve for LiCl-KCl sample 3 (30.5 wt% LiCl) with 10 K min^{-1} heating rate

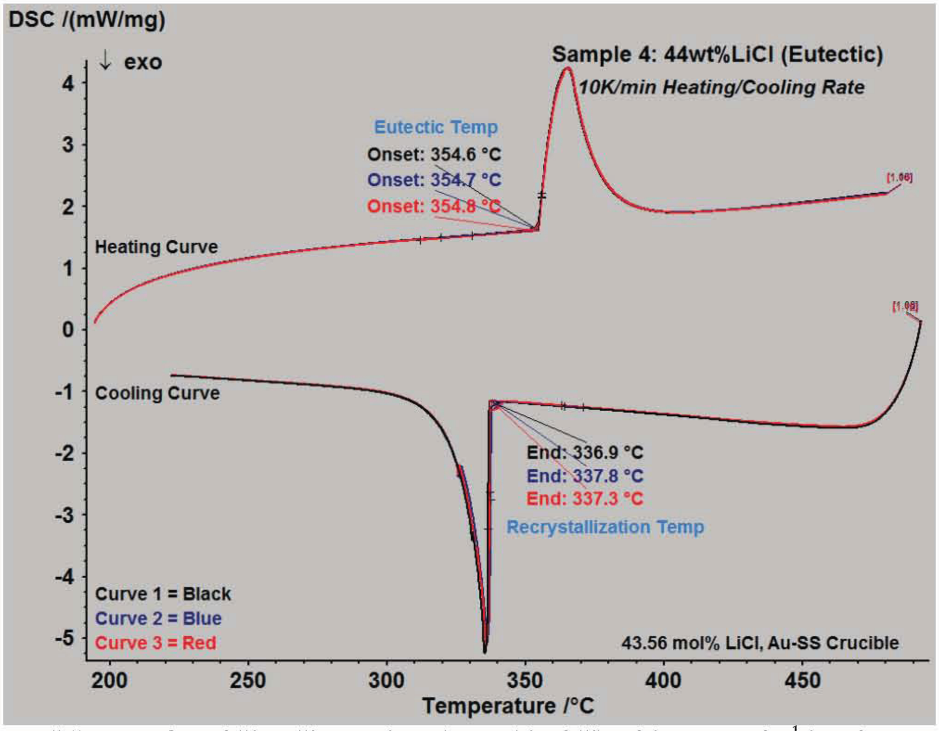

Figure C-12. DSC curve for LiCl-KCl sample 4 (44 wt% LiCl) with 10 K min^{-1} heating rate

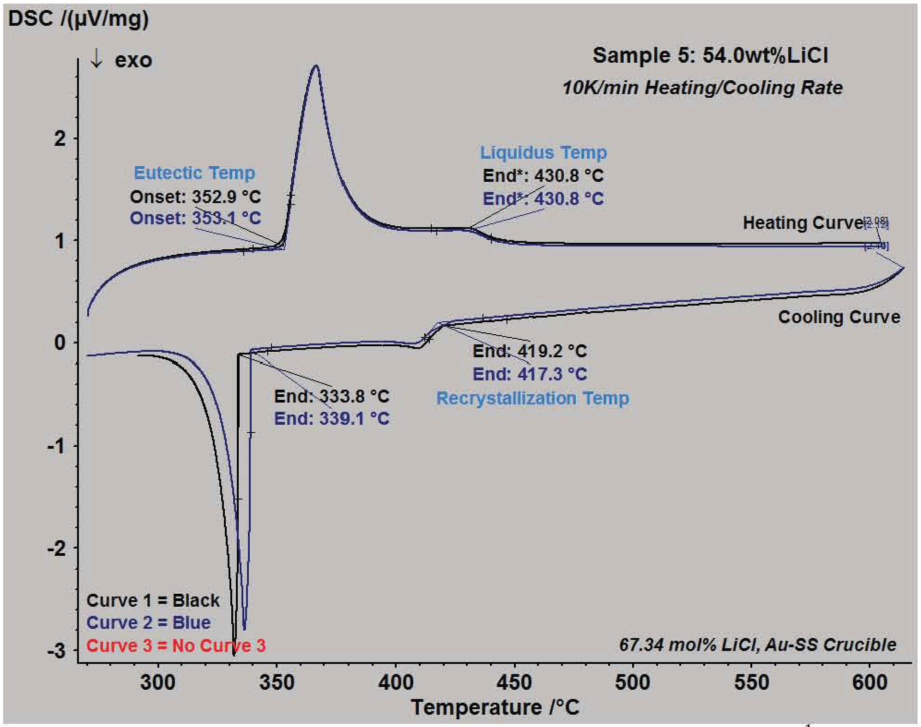

Figure C-13. DSC curve for LiCl-KCl sample 5 (54.0 wt% LiCl) with 10 K min^{-1} heating rate

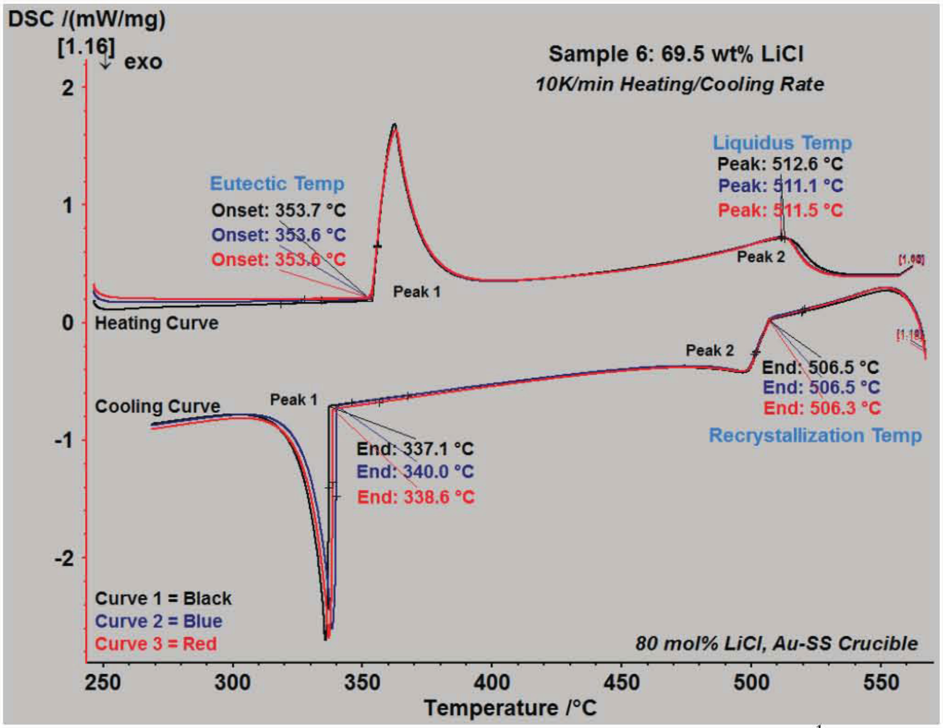

Figure C-14. DSC curve for LiCl-KCl sample 6 (69.5 wt% LiCl) with 10 K min^{-1} heating rate

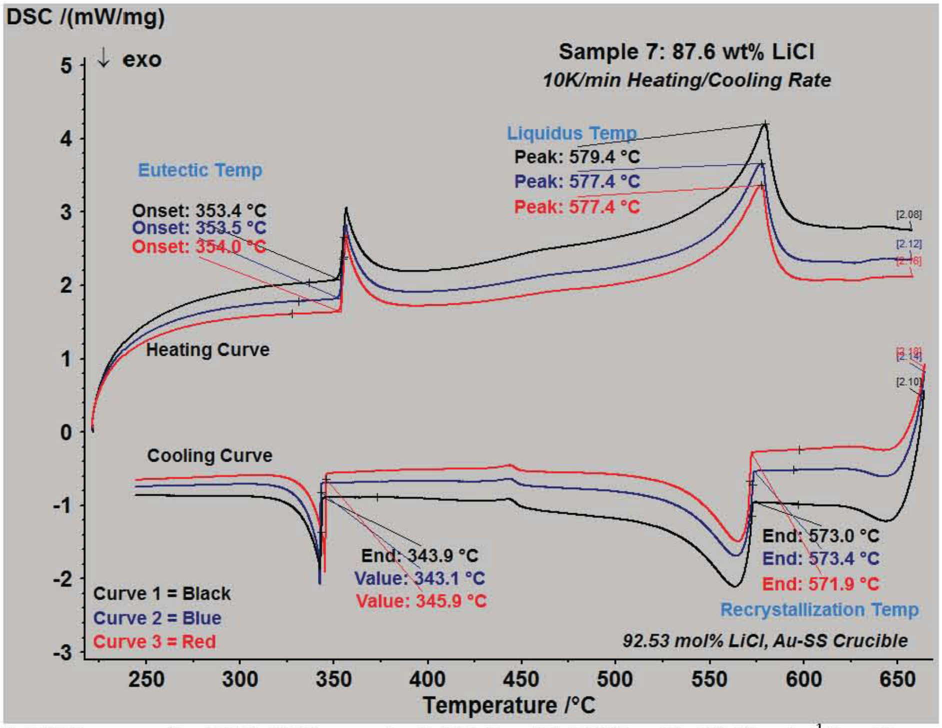

Figure C-15. DSC curve for LiCl-KCl sample 7 (87.6 wt% LiCl) with 10 K min^{-1} heating rate

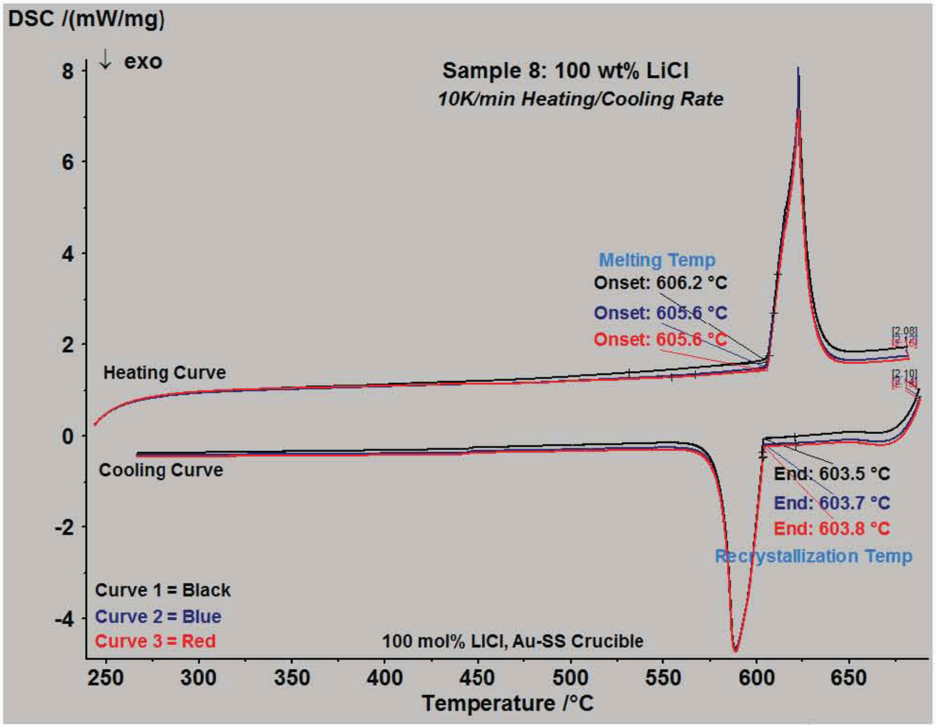

Figure C-16. DSC curve for LiCl-KCl sample 8 (100 wt% LiCl) with 10 K min^{-1} heating rate

Table C-2 provides information on the eutectic and liquidus temperatures for various compositions of LiCl-KCl with a heating/cooling rate of 10 K min^{-1}

Table C-2. Summary of results taken from Figure C-9 through Figure C-16

Summary: 10 K min^{-1} Heating Rate						
			Curve 1	Curve 2	Curve 3	Average
Sample 1	KCl (pure)	Eutectic Temp, °C	--	--	--	--
		Liquidus Temp, °C	769.9	769.7	769.4	769.7
Sample 2	12.5 wt% LiCl-KCl	Eutectic Temp, °C	352.3	351.9	351.7	352.0
		Liquidus Temp, °C	682.2	682.2	682.7	682.4
Sample 3	30.5 wt% LiCl-KCl	Eutectic Temp, °C	354.3	354.0	353.9	354.1
		Liquidus Temp, °C	520.9	519.3	520.6	520.3
Sample 4	44.0 wt% LiCl-KCl	Eutectic Temp, °C	354.6	354.7	354.8	354.7
		Liquidus Temp, °C	--	--	--	--
Sample 5	54.0 wt% LiCl-KCl	Eutectic Temp, °C	352.9	353.1	--	353.0
		Liquidus Temp, °C	430.8	430.8	--	430.8
Sample 6	69.5 wt% LiCl-KCl	Eutectic Temp, °C	353.7	353.6	353.6	353.6
		Liquidus Temp, °C	512.6	511.1	511.5	511.7
Sample 7	87.6 wt% LiCl-KCl	Eutectic Temp, °C	353.4	353.5	354.0	353.6
		Liquidus Temp, °C	579.4	577.4	577.4	578.1
Sample 8	LiCl (pure)	Eutectic Temp, °C	--	--	--	--
		Liquidus Temp, °C	606.2	605.6	605.6	605.8

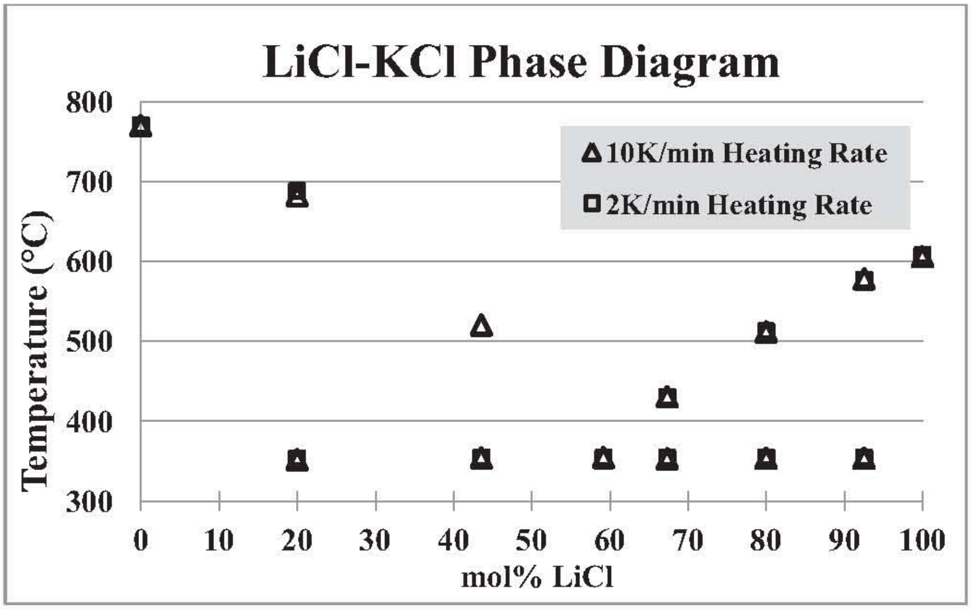

Appendix D: FFTF Fuel Processing

D.1 Before FFTF Fuel Processing

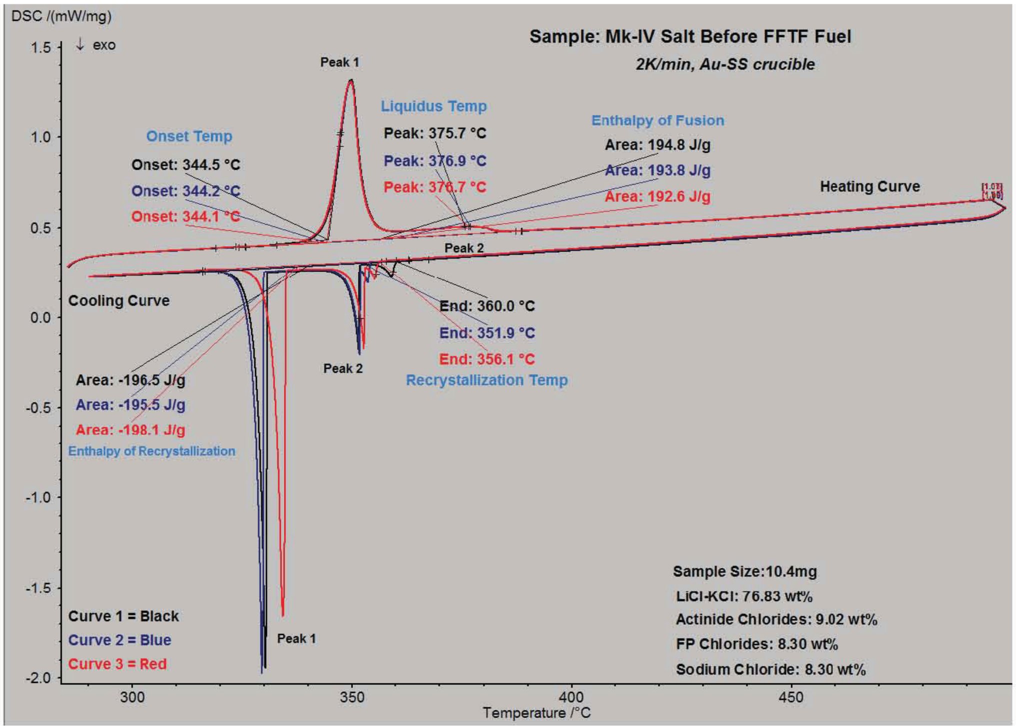

Figure D-1. DSC curve for before FFTF, 76.83 wt% LiCl-KCl with 2 K min^{-1} heating rate

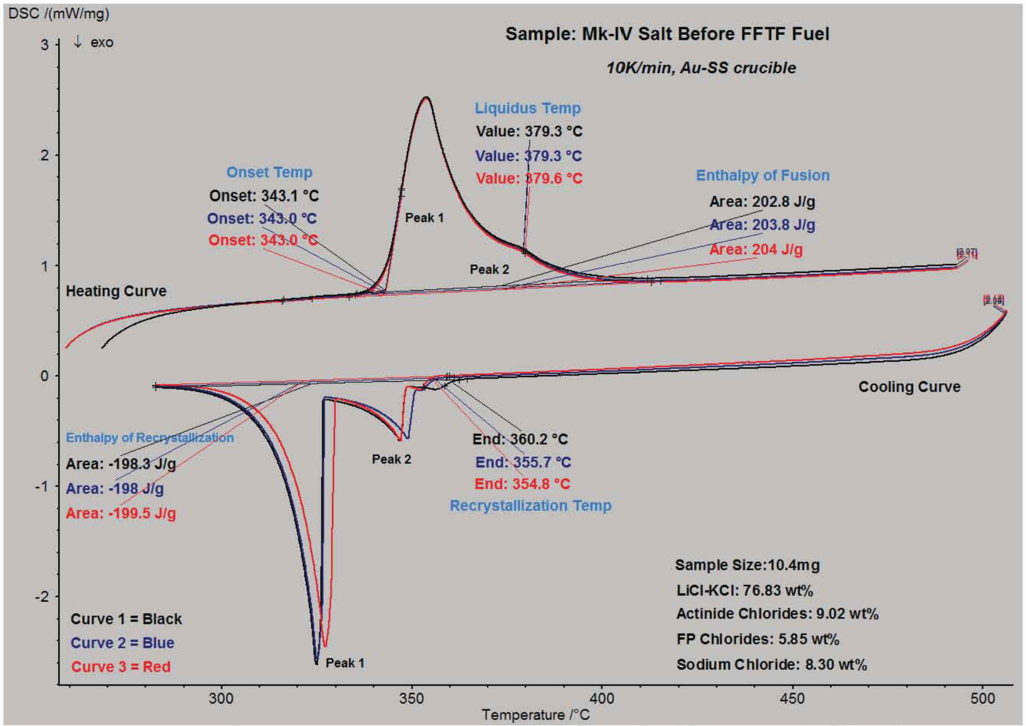

Figure D-2. DSC curve for before FFTF, 76.83 wt% LiCl-KCl with 10 K min^{-1} heating rate

D.2 After FFTF Fuel Processing

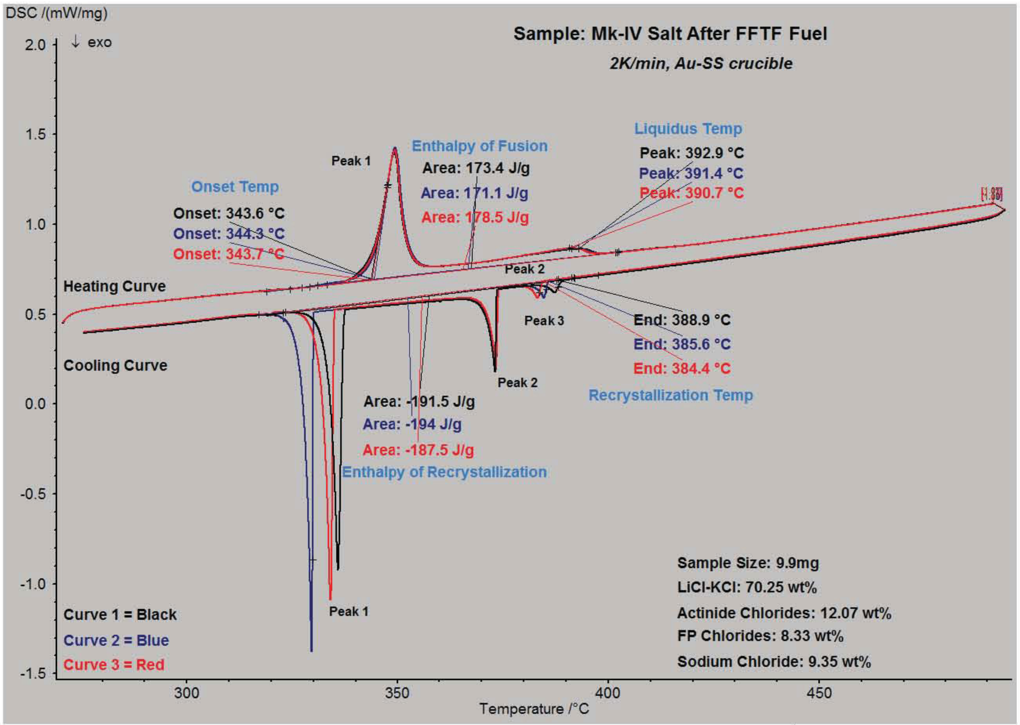

Figure D-3. DSC curve for after FFTF, 70.25 wt% LiCl-KCl with 2 K min^{-1} heating rate

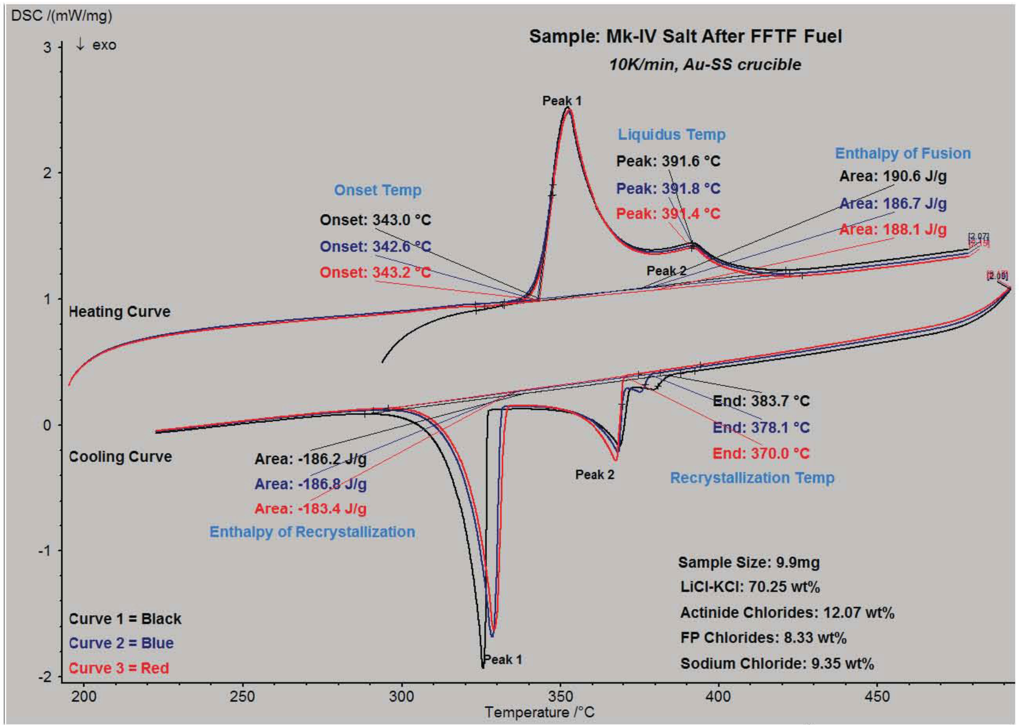

Figure D-4. DSC curve for after FFTF, 70.25 wt% LiCl-KCl with 10 K min^{-1} heating rate

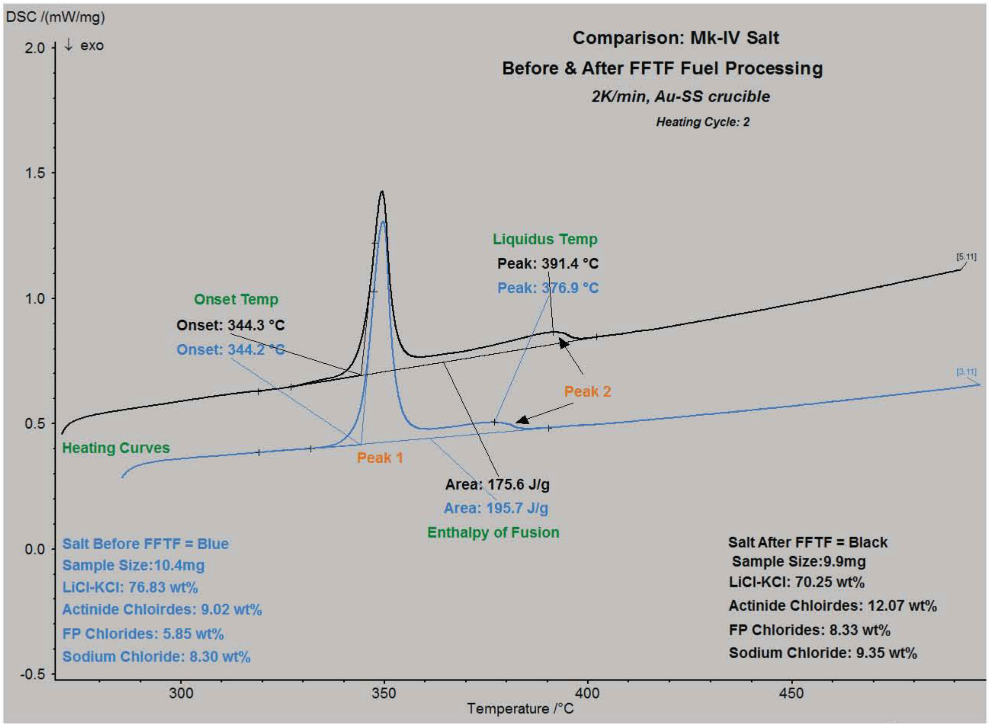

Figure D-5. DSC heating curves comparing Before FFTF with After FFTF, 2 K min^{-1} heating rate

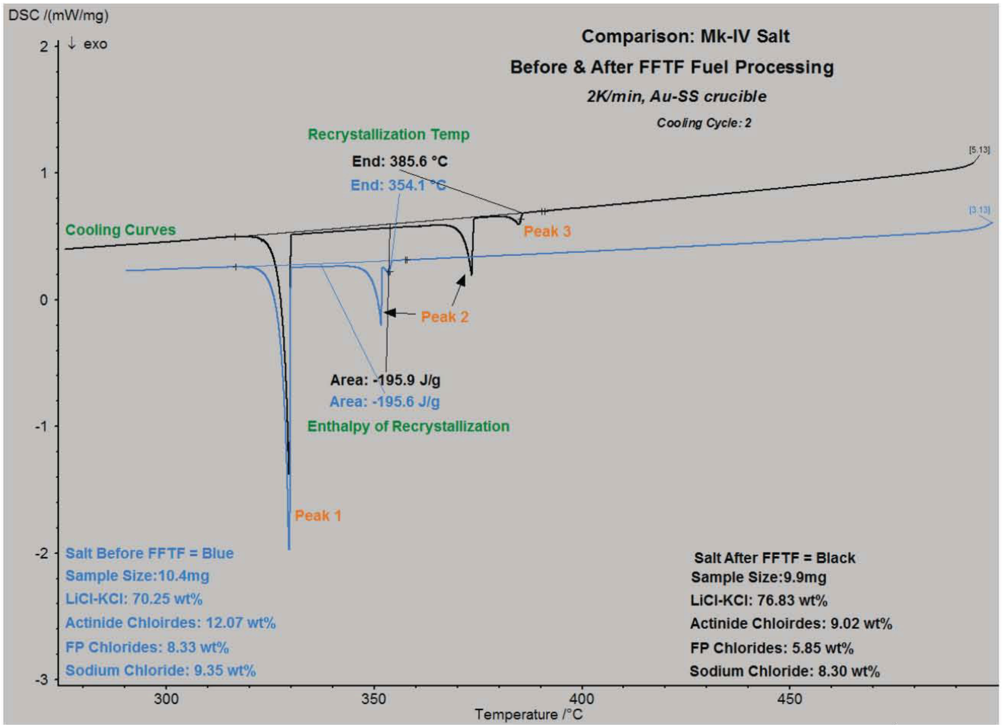

Figure D-6. DSC cooling curves comparing before FFTF with After FFTF, 2 K min^{-1} heating rate

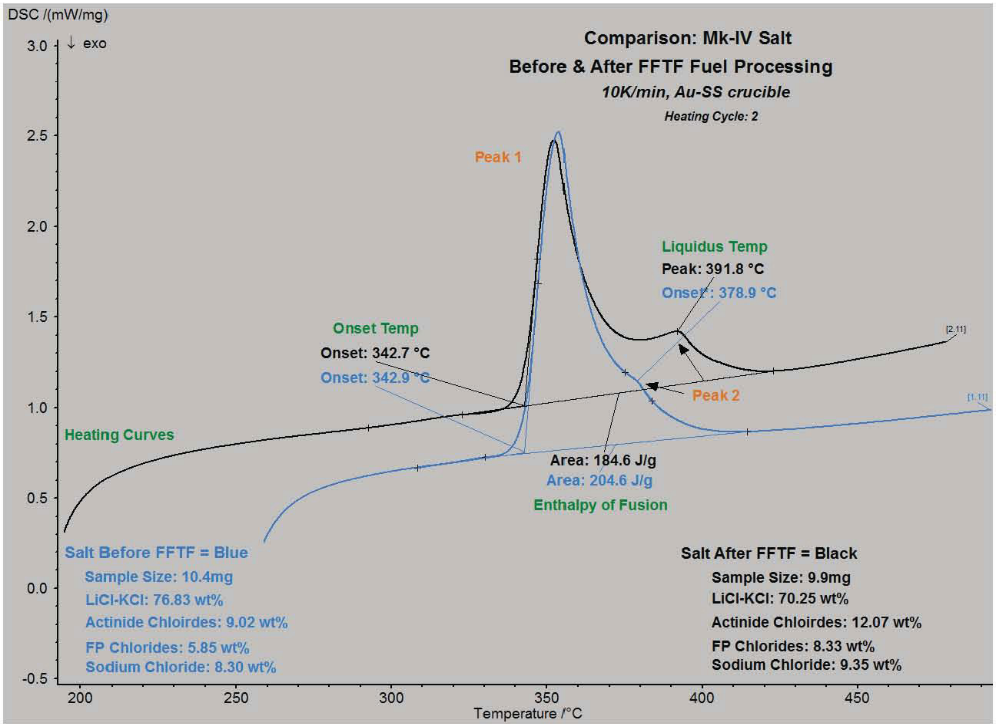

Figure D-7. DSC heating curves comparing before FFTF with After FFTF, 10 K min^{-1} heating rate

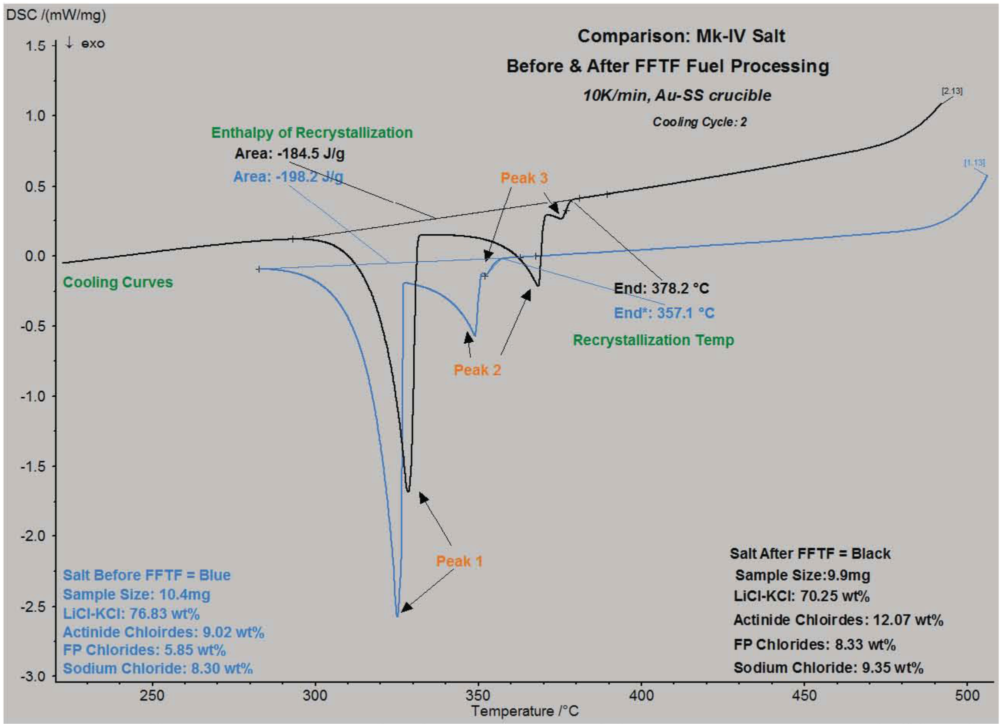

Figure D-8. DSC cooling curves comparing before FFTF with After FFTF, 10 K min^{-1} heating rate

Appendix E: INTEC Fuel Processing

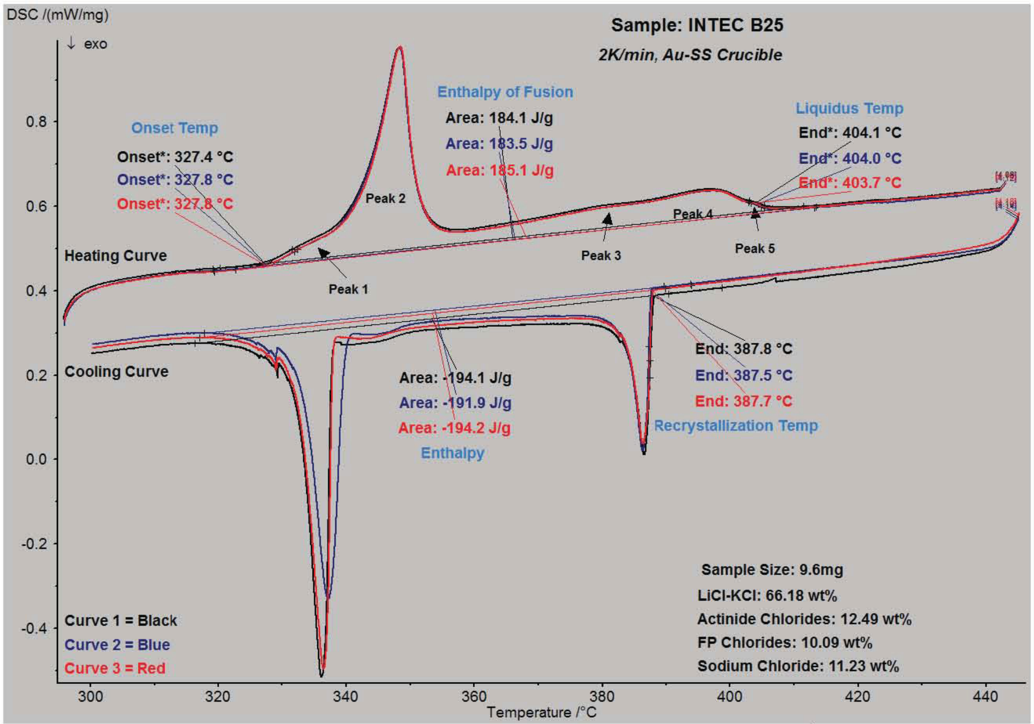

Figure E-1. DSC curve for INTEC B25, 66.18 wt% LiCl-KCl with 2 K min^{-1} heating rate

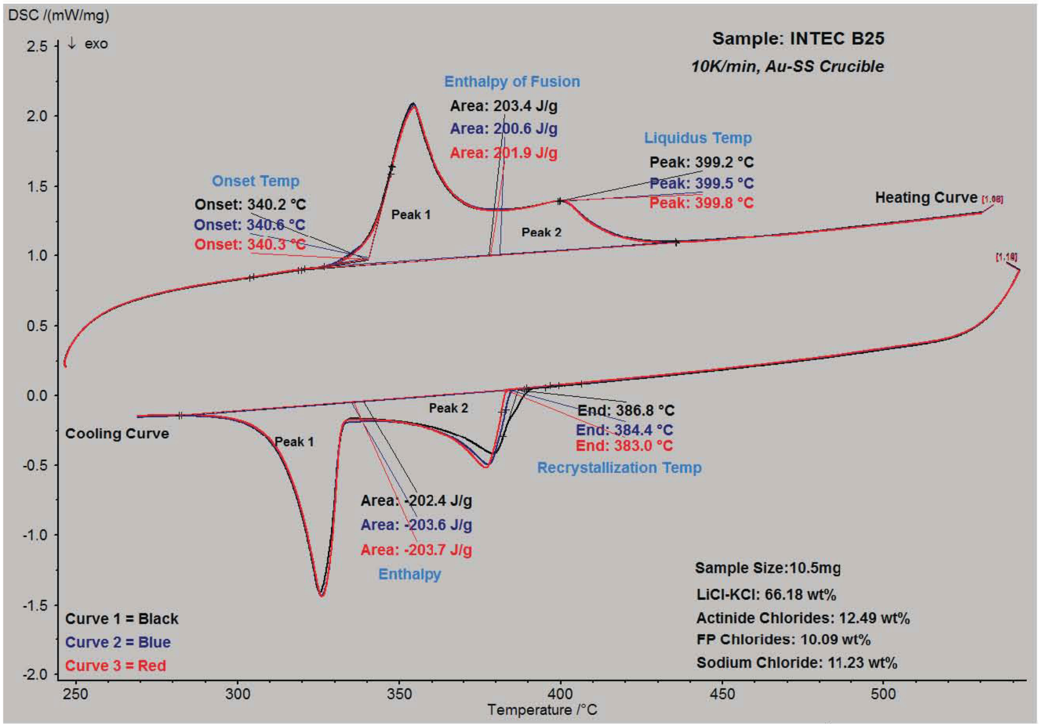

Figure E-2. DSC curve for INTEC B25, 66.18 wt% LiCl-KCl with 10 K min^{-1} heating rate

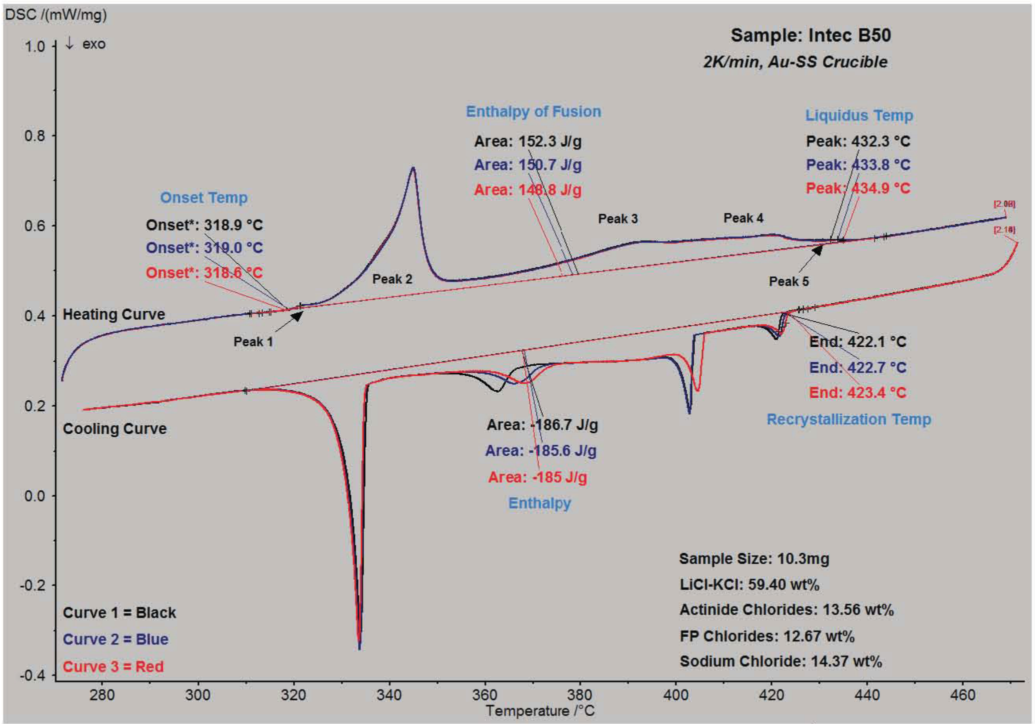

Figure E-3. DSC curve for INTEC B50, 59.40 wt% LiCl-KCl with 2 K min^{-1} heating rate

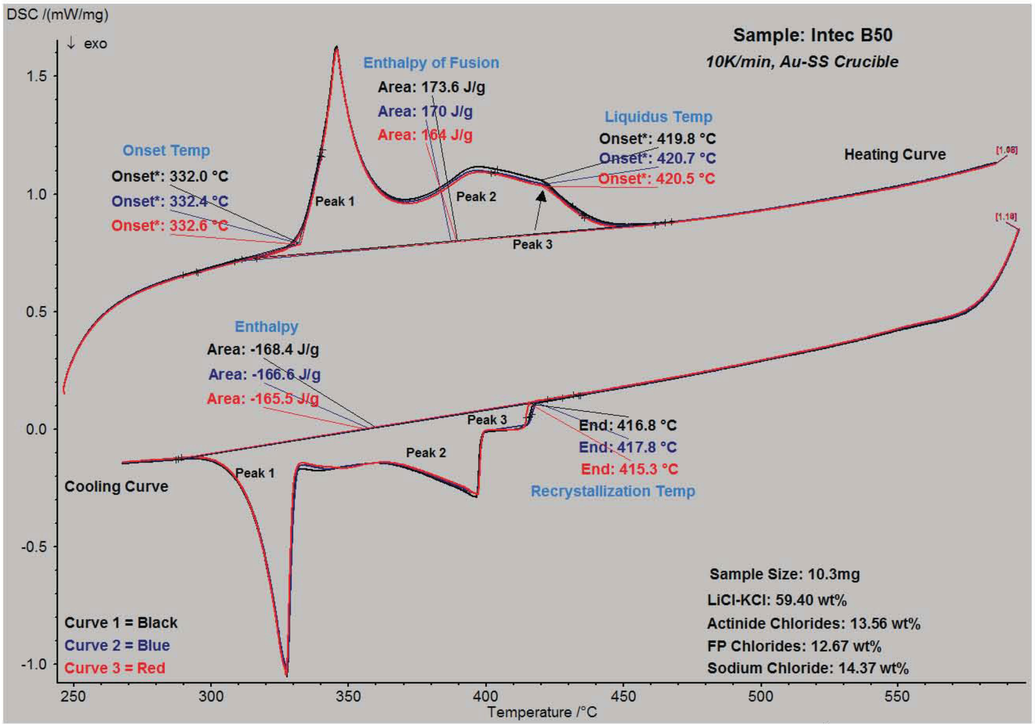

Figure E-4. DSC curve for INTEC B50, 59.40 wt% LiCl-KCl with 10 K min^{-1} heating rate

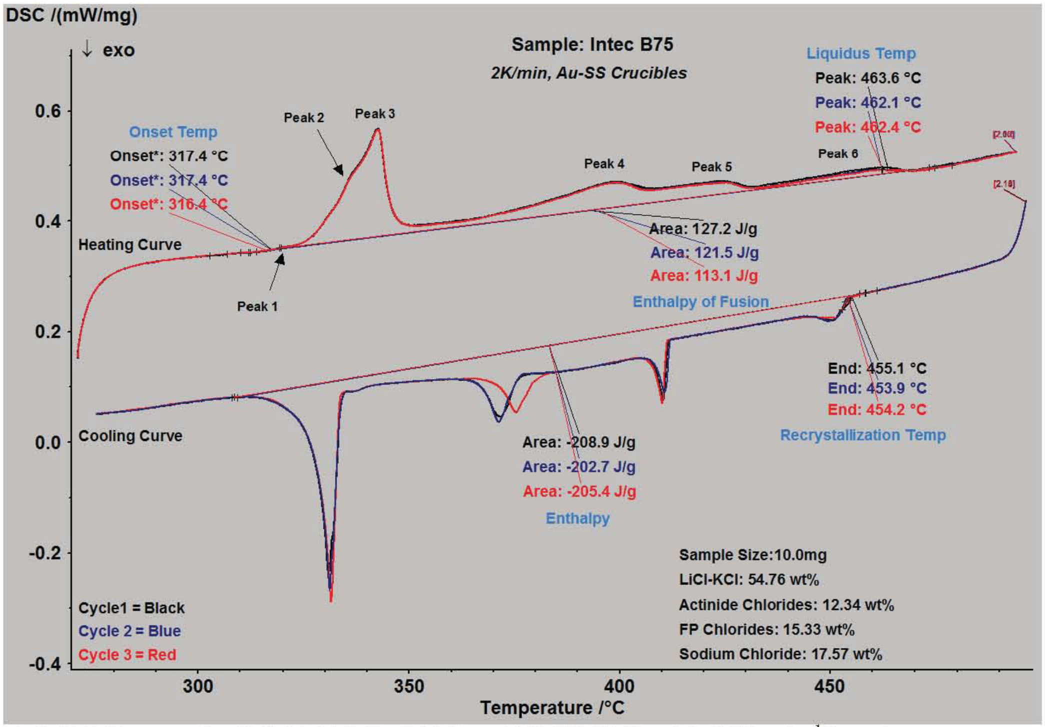

Figure E-5. DSC curve for INTEC B75, 54.76 wt% LiCl-KCl with 2 K min^{-1} heating rate

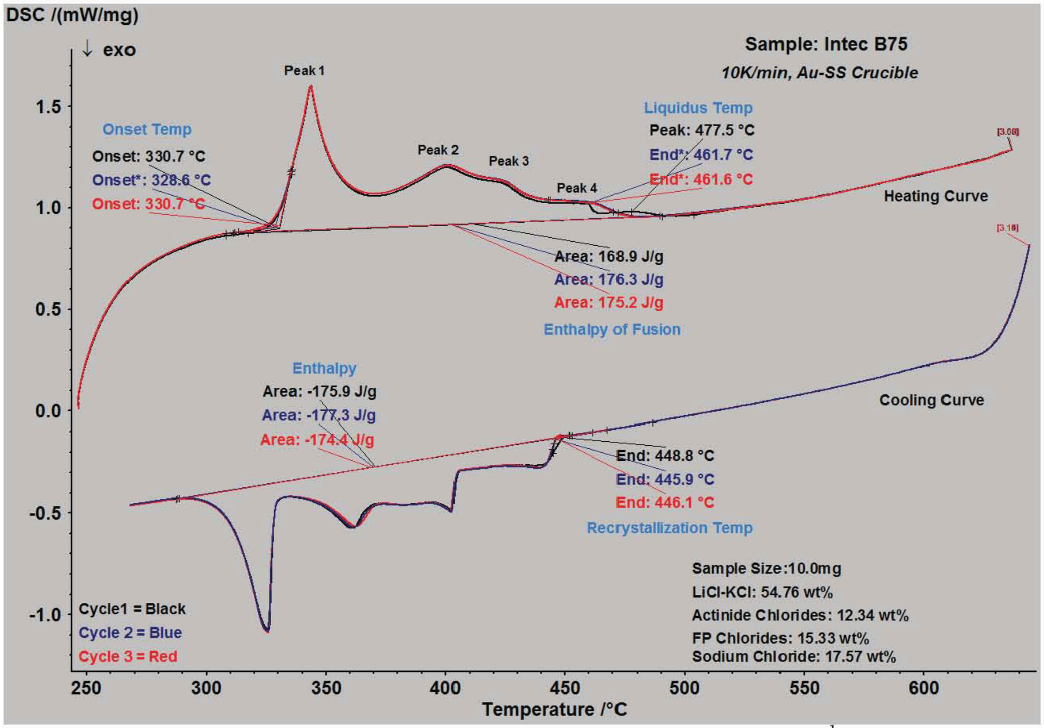

Figure E-6. DSC curve for INTEC B75, 54.76 wt% LiCl-KCl with 10 K min^{-1} heating rate

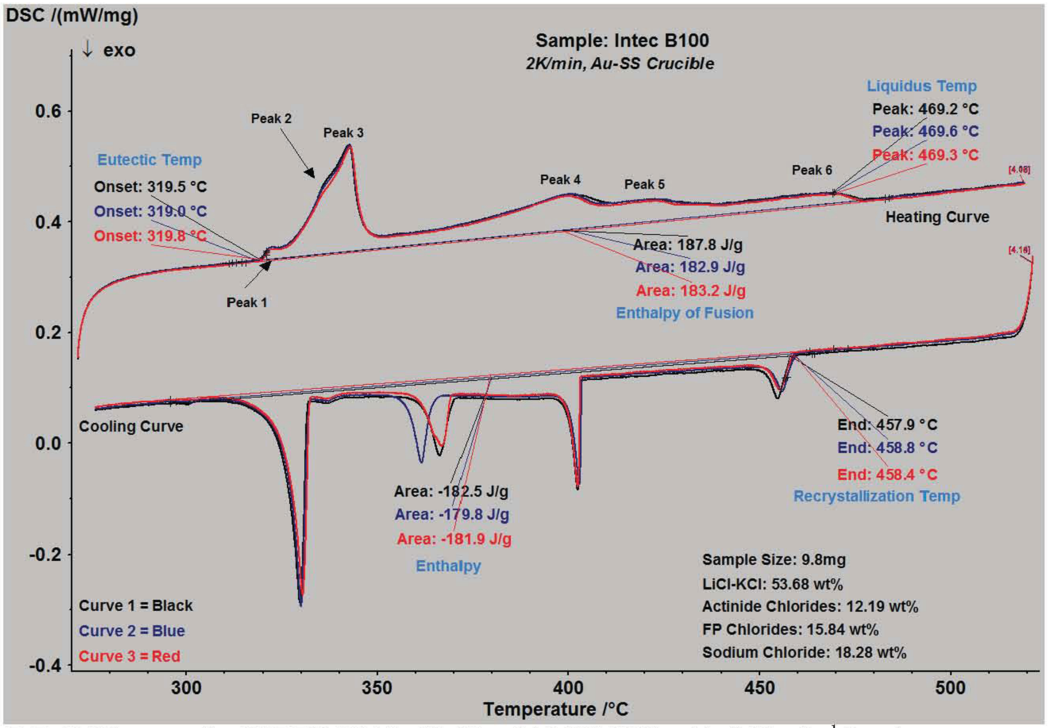

Figure E-7. DSC curve for INTEC B100, 53.68 wt% LiCl-KCl with 2 K min^{-1} heating rate

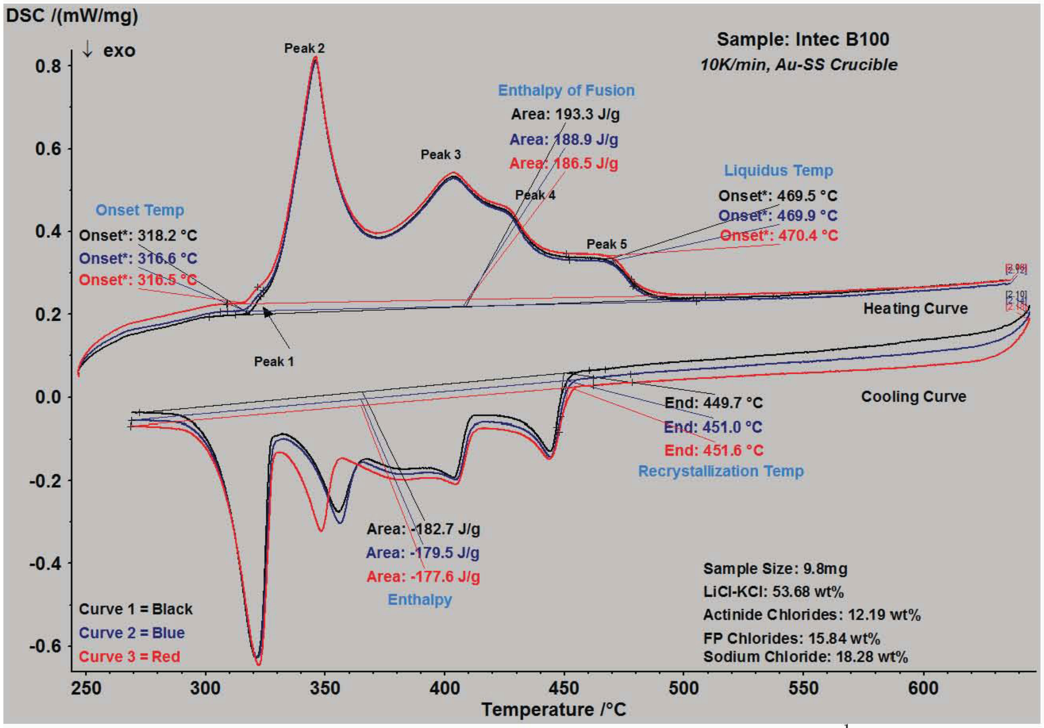

Figure E-8. DSC curve for INTEC B100, 53.68 wt% LiCl-KCl with 10 K min^{-1} heating rate

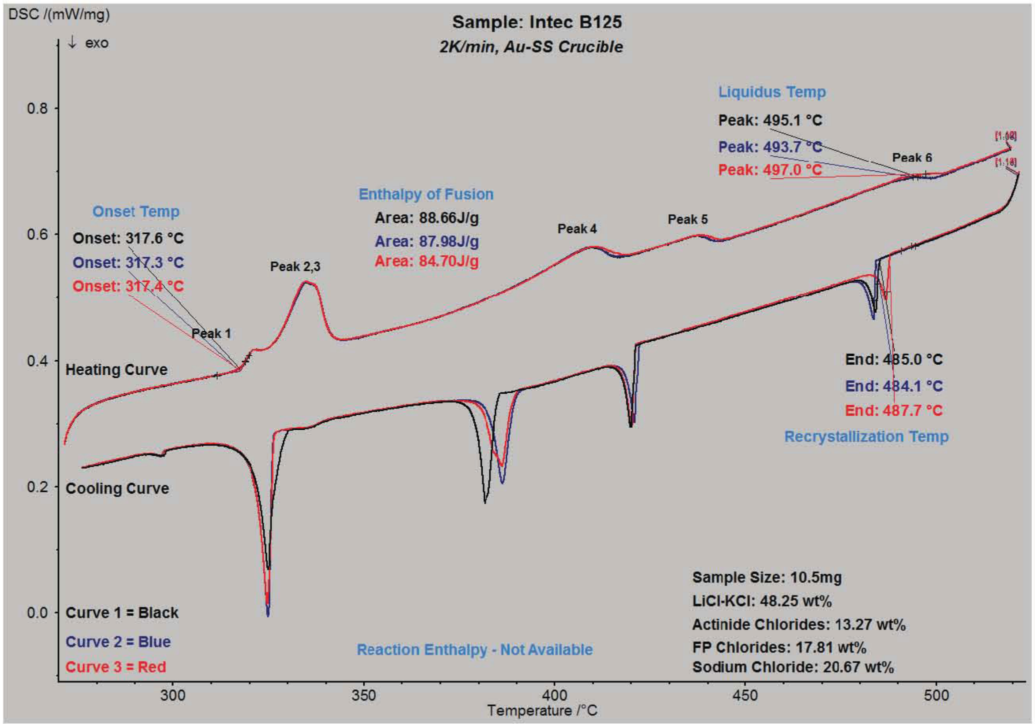

Figure E-9. DSC curve for INTEC B125, 48.25 wt% LiCl-KCl with 2 K min^{-1} heating rate

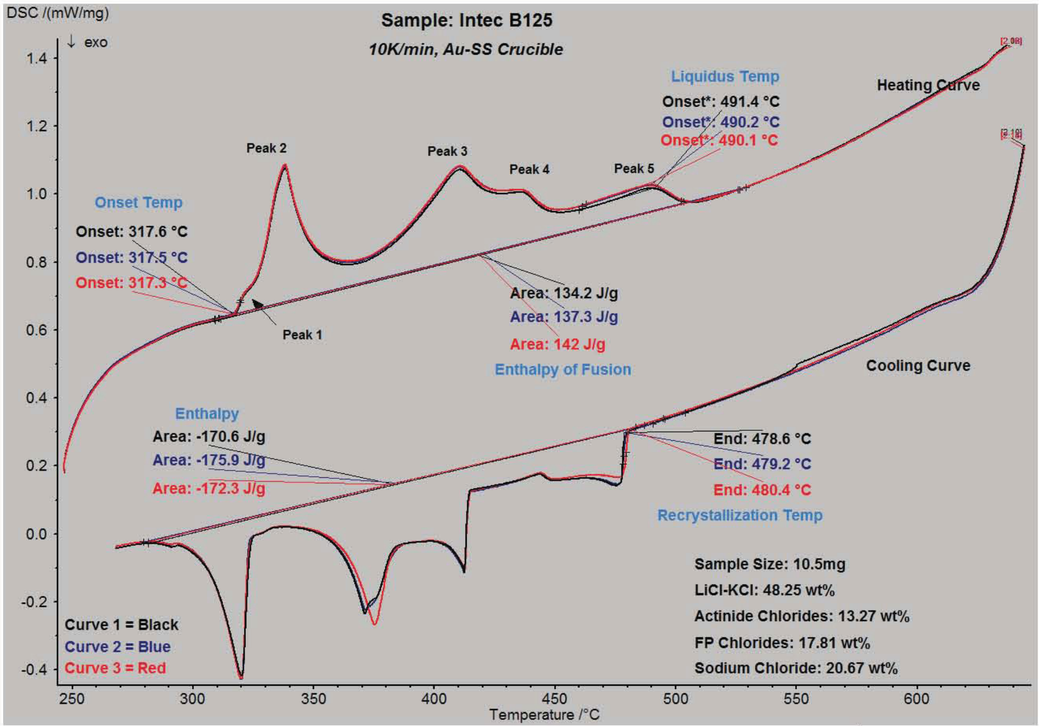

Figure E-10. DSC curve for INTEC B125, 48.25 wt% LiCl-KCl with 10 K min^{-1} heating rate

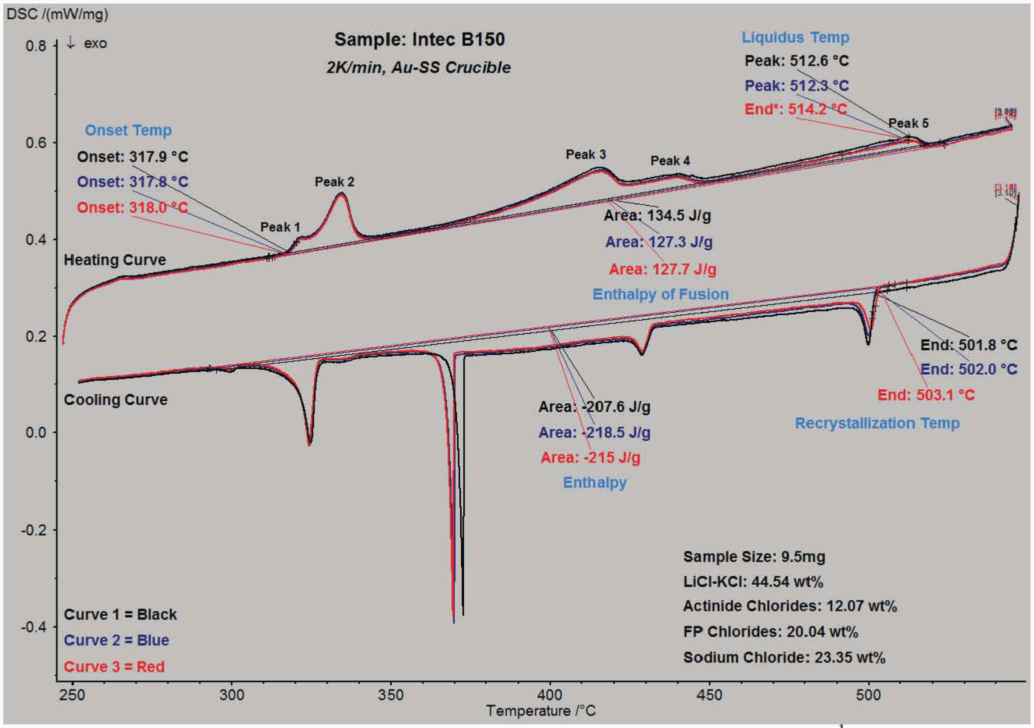

Figure E-11. DSC curve for INTEC B150, 44.54 wt% LiCl-KCl with 2 K min^{-1} heating rate

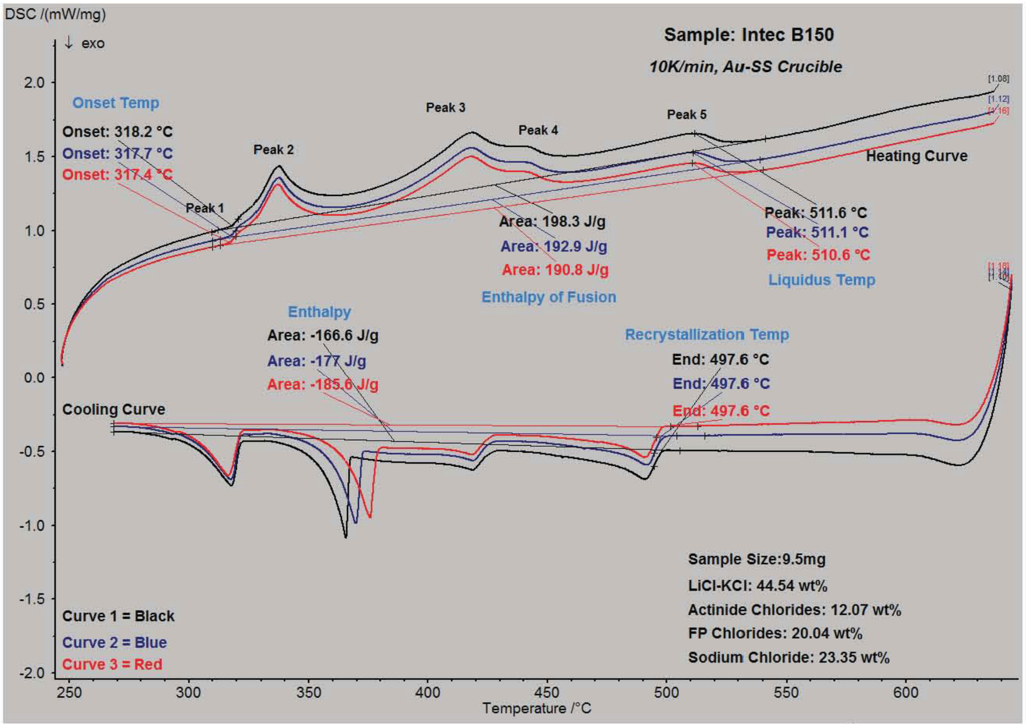

Figure E-12. DSC curve for INTEC B150, 44.54 wt% LiCl-KCl with 10 K min^{-1} heating rate

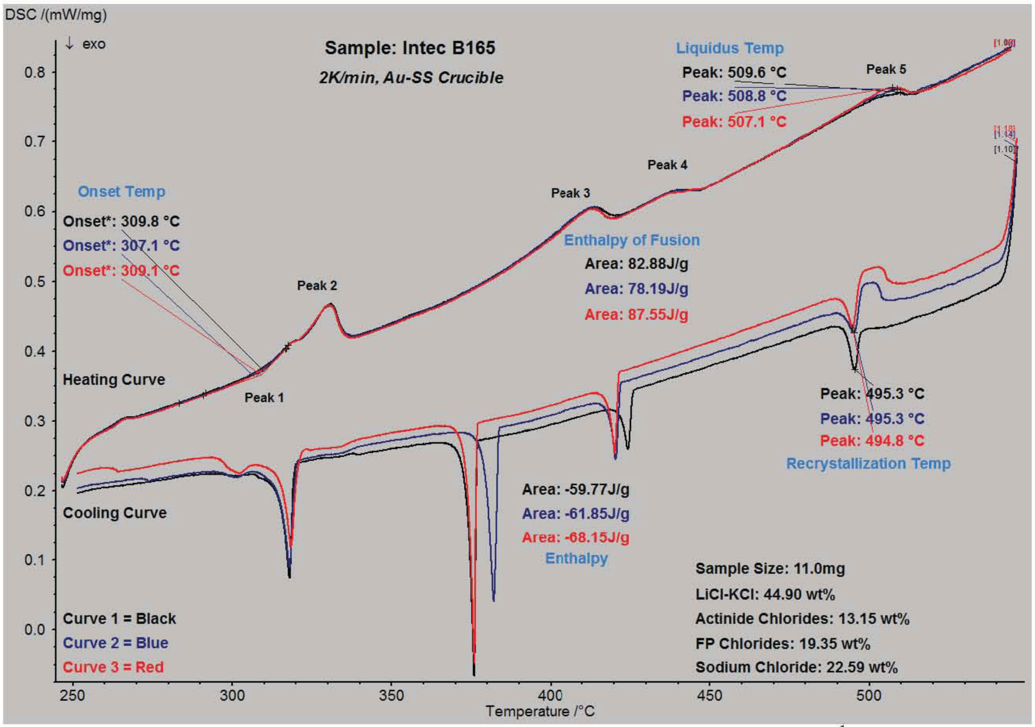

Figure E-13. DSC curve for INTEC B165, 44.90 wt% LiCl-KCl with 2 K min^{-1} heating rate

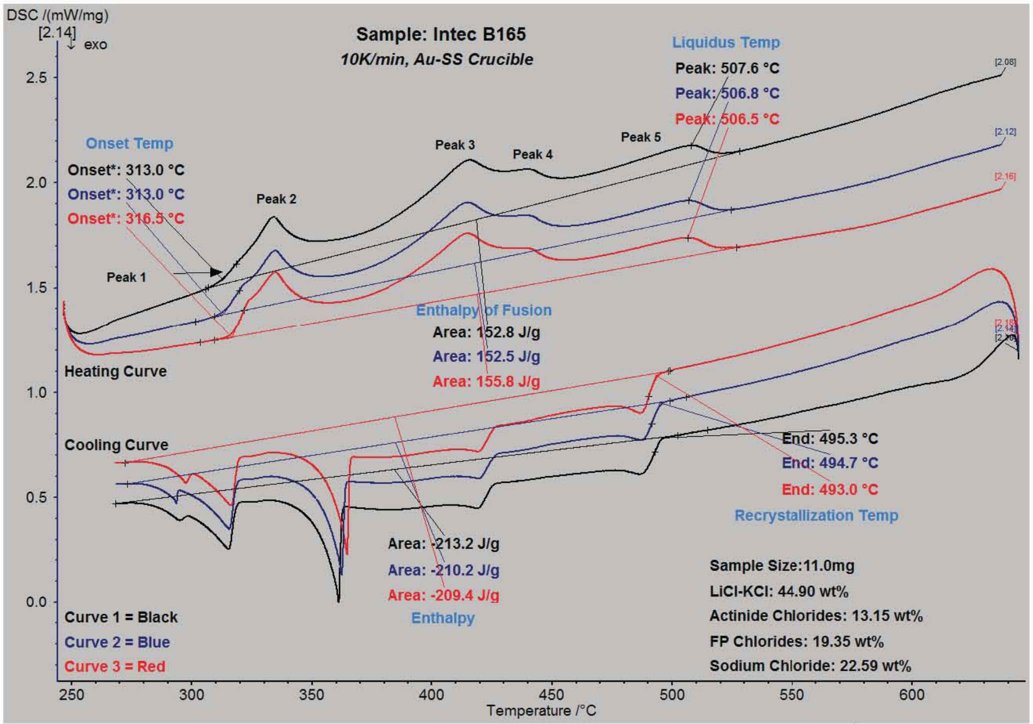

Figure E-14. DSC curve for INTEC B165, 44.90 wt% LiCl-KCl with 10 K min^{-1} heating rate

Sample	**Cycle**	**Onset (°C)**	**Liquidus (°C)**	**Enthalpy of Fusion (J/g)**	**Enthalpy (J/g)**
INTEC B25	1	327.4	404.1	184.1	-194.1
	2	327.8	404	183.5	-191.9
	3	327.8	403.7	185.1	-194.2
	Average	**327.7**	**403.9**	**184.2**	**-193.4**
INTEC B50	1	318.9	432.3	152.3	-186.7
	2	319	433.8	150.7	-185.6
	3	318.6	434.9	148.8	-185
	Average	**318.8**	**433.7**	**150.6**	**-185.8**
INTEC B75	1	317.4	463.6	127.2	-208.9
	2	317.4	462.1	121.5	-202.7
	3	316.4	462.4	113.1	-205.4
	Average	**317.1**	**462.7**	**120.6**	**-205.7**
INTEC B100	1	319.5	469.2	187.8	-182.5
	2	319	469.6	182.9	-179.8
	3	319.8	469.3	183.2	-181.9
	Average	**319.4**	**469.4**	**184.6**	**-181.4**
INTEC B125	1	317.6	495.1		
	2	317.3	493.7		
	3	317.4	497		
	Average	**317.4**	**495.3**		
INTEC B150	1	317.9	512.6	134.5	-207.6
	2	317.8	512.3	127.3	-218.5
	3	318	514.2	127.7	-215
	Average	**317.9**	**513.0**	**129.8**	**-213.7**
INTEC B165	1	309.8	509.6		
	2	307.1	508.8		
	3	309.1	507.1		
	Average	**308.7**	**508.5**		

Mk-IV Molten Salt Simulation DSC Results

Heating Curves

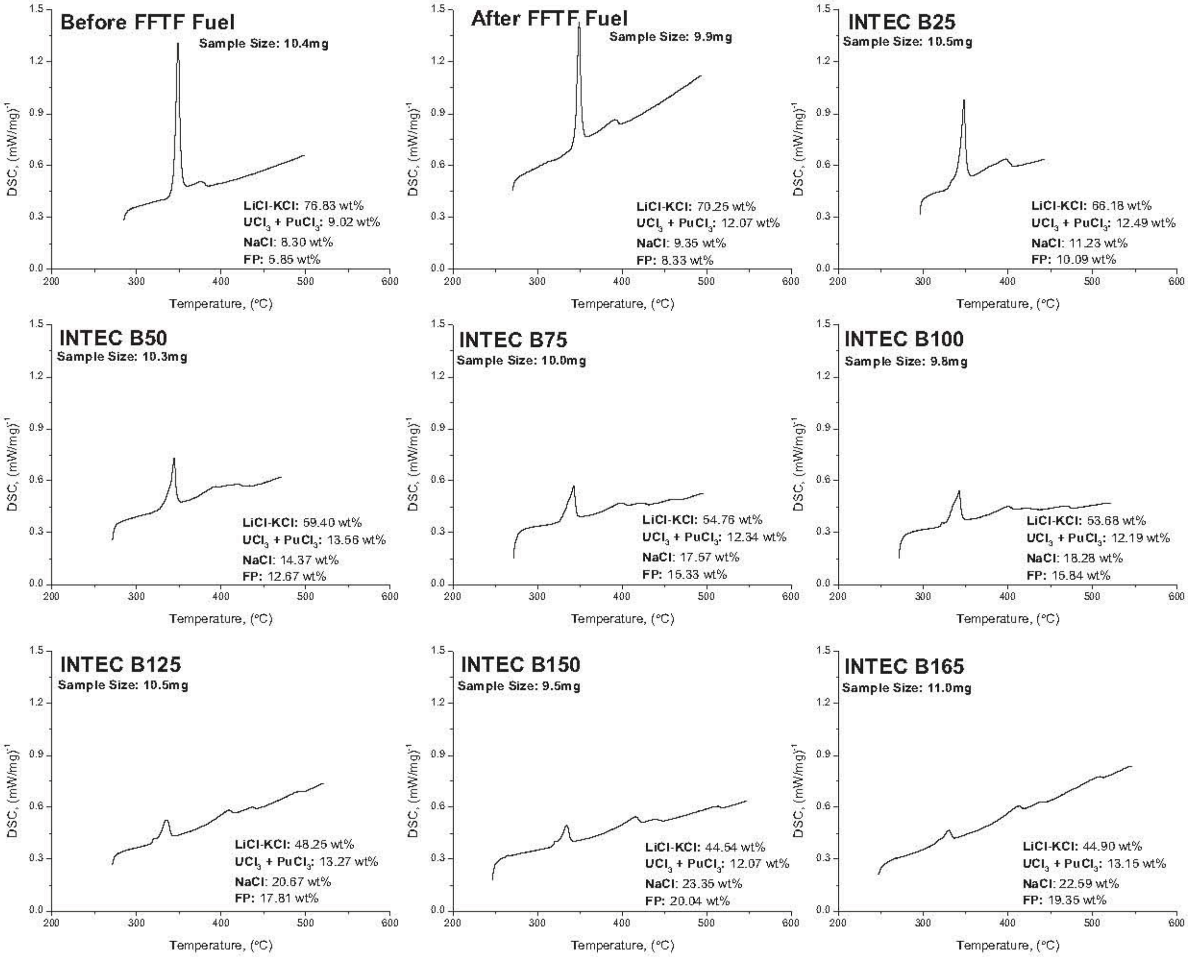

2K/min Heating Rate, Au-SS Crucible

FP: Fission Products = $NdCl_3$, CsCl, $CeCl_3$. $LaCl_3$, $PrCl_3$, $BaCl_2$, $SmCl_3$, $SrCl_2$

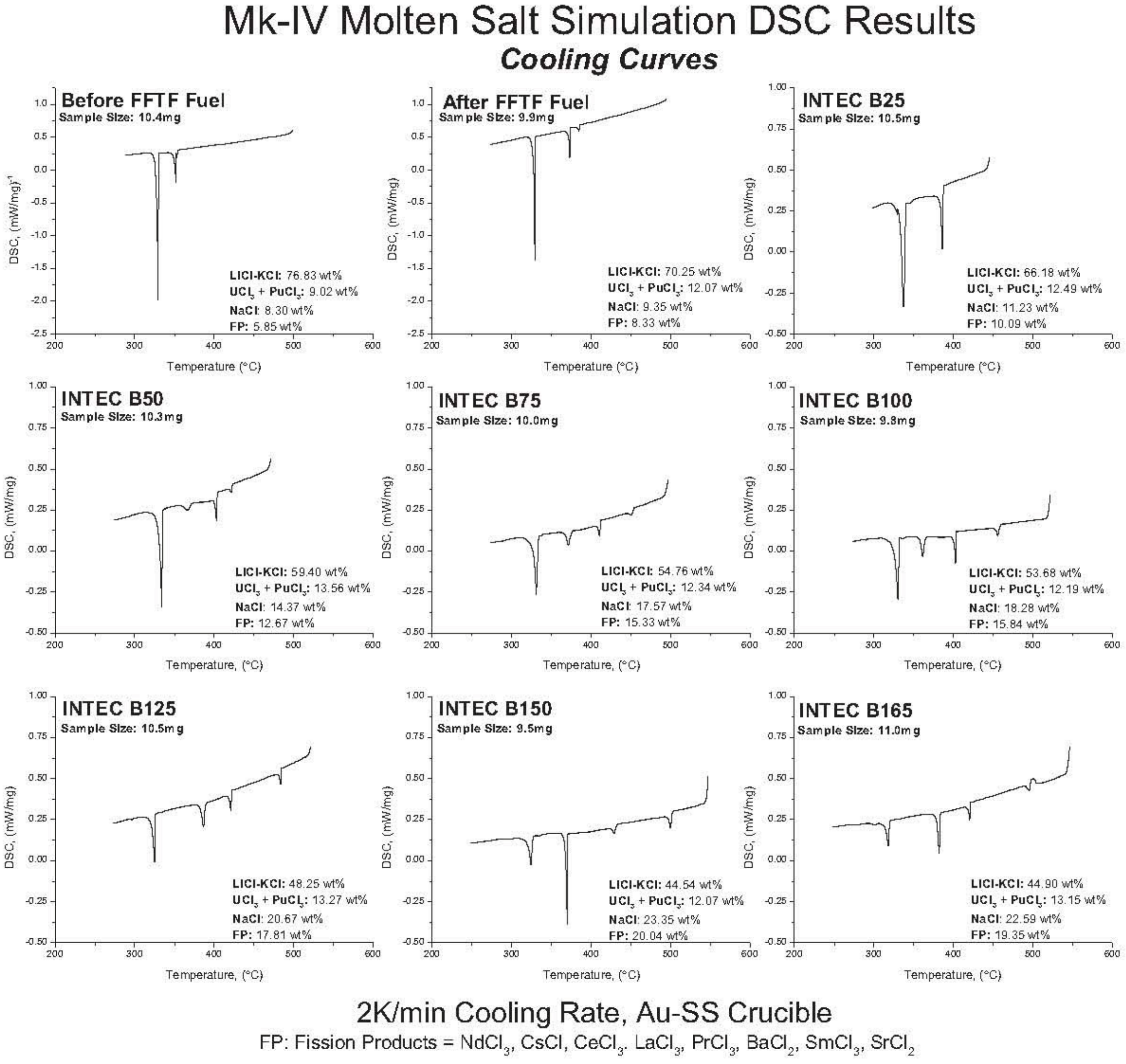

Mk-IV Molten Salt Simulation DSC Results

Cooling Curves

Before FFTF Fuel
Sample Size: 10.4mg
LiCl-KCl: 76.83 wt%
UCl$_3$ + PuCl$_3$: 9.02 wt%
NaCl: 8.30 wt%
FP: 5.85 wt%

After FFTF Fuel
Sample Size: 9.9mg
LiCl-KCl: 70.25 wt%
UCl$_3$ + PuCl$_3$: 12.07 wt%
NaCl: 9.35 wt%
FP: 8.33 wt%

INTEC B25
Sample Size: 10.5mg
LiCl-KCl: 66.18 wt%
UCl$_3$ + PuCl$_3$: 12.49 wt%
NaCl: 11.23 wt%
FP: 10.09 wt%

INTEC B50
Sample Size: 10.3mg
LiCl-KCl: 59.40 wt%
UCl$_3$ + PuCl$_3$: 13.56 wt%
NaCl: 14.37 wt%
FP: 12.67 wt%

INTEC B75
Sample Size: 10.0mg
LiCl-KCl: 54.76 wt%
UCl$_3$ + PuCl$_3$: 12.34 wt%
NaCl: 17.57 wt%
FP: 15.33 wt%

INTEC B100
Sample Size: 9.8mg
LiCl-KCl: 53.68 wt%
UCl$_3$ + PuCl$_3$: 12.19 wt%
NaCl: 18.28 wt%
FP: 15.84 wt%

INTEC B125
Sample Size: 10.5mg
LiCl-KCl: 48.25 wt%
UCl$_3$ + PuCl$_3$: 13.27 wt%
NaCl: 20.67 wt%
FP: 17.81 wt%

INTEC B150
Sample Size: 9.5mg
LiCl-KCl: 44.54 wt%
UCl$_3$ + PuCl$_3$: 12.07 wt%
NaCl: 23.35 wt%
FP: 20.04 wt%

INTEC B165
Sample Size: 11.0mg
LiCl-KCl: 44.90 wt%
UCl$_3$ + PuCl$_3$: 13.15 wt%
NaCl: 22.59 wt%
FP: 19.35 wt%

2K/min Cooling Rate, Au-SS Crucible

FP: Fission Products = $NdCl_3$, CsCl, $CeCl_3$. $LaCl_3$, $PrCl_3$, $BaCl_2$, $SmCl_3$, $SrCl_2$